CHARACTERIZING SOIL EROSION POTENTIAL USING ELECTRICAL RESISTIVITY IMAGING

by

MD ZAHIDUL KARIM

B.S., Bangladesh University of Engineering and Technology, 2013

A THESIS

submitted in partial fulfillment of the requirements for the degree

MASTER OF SCIENCE

Department of Civil Engineering
College of Engineering

KANSAS STATE UNIVERSITY
Manhattan, Kansas

2016

Approved by:

Major Professor
Dr. Stacey Tucker-Kulesza

Copyright

Abstract

The erosion rate, or erodibility, of soil depends on many soil characteristics including: plasticity, water content, grain size, percent clay, compaction, and shear strength. Many of these characteristics also influence soil in situ bulk electrical resistivity (ER) measurements. The objective of this study was to characterize soil erosion potential by correlating the in situ ER of soil with erodibility measured in the Kansas State University Erosion Function Apparatus (KSU-EFA). ER surveys were conducted at eleven bridge sites. Soil samples were also collected at each site with a drill rig from the surface to three meters using thin-walled Shelby tubes. Five samples were collected at each site, tested in the KSU-EFA, and classified according to the Unified Soil Classification System. Analysis showed that the rapid in situ data obtained from an ER survey can be used to categorize the level of erodibility. As such, ER surveys may be used to characterize the soils at future bridge sites or prioritize existing bridges for additional testing to measure the scour potential. Moreover, ER surveys may be used to determine which existing bridges should be closed or closely monitored for scour potential during a flood event. Analytical models to predict critical shear stress using ER and other soil parameters were constructed.

Table of Contents

List of Figures

List of Tables

Acknowledgements

My graduate study at K-State has been a wonderful experience for me. First, I would like to express my deep sense of appreciation and gratitude to my major professor Dr. Stacey E. Tucker-Kulesza who has given me an exciting project to work on. Surely, the knowledge I have earned from her guidance, will make me a better research professional in the future. I am also grateful to her for providing me financial support throughout the master's study.

I would also like to express my sincere gratitude to Dr. Dunja Peric and Dr. Eric Fitzsimmons for their kind support as my committee members. Again, I would not be able to finish my research without the help my wonderful groupmates, Weston Koehn, Tri Tran, Lisa Shofstall, Andrew Crowder, Michael Snapp, Abdullah-Al-Ali, Luke Augustine, and Therea Collins. I also acknowledge the kind help of Mr. Cody Delaney for helping me with all sorts of technical issues in my research.

Finally, I am grateful to Kansas Department of Transportation for funding the project and providing all sorts of direction and help in sampling.

Dedication

I would like to dedicate this thesis to my parents, Md Enayet Karim and Rawshawn Ara. Without their inspiration and continued support, I would not be able to come this far. Thank you for everything!

Chapter 1 - Introduction

The Federal Highway Administration (FHWA) defines scour as the result of erosive action of flowing water, excavating and carrying away material from the bed and banks of streams and from around the piers and abutments of bridges (Calappi et al. 2010). As of 2003, The National Bridge Inventory (NBI) contained 604,279 bridges including the federal, state, county, and city bridges of the United States (Richardson et al. 2003). Of these bridges, approximately 84% (503,000) are built over waterways, of which, over 20,000 bridges are classified as "scour critical". Therefore, at least one out of every twenty-five bridges in the United States are vulnerable to scour. According to Nassif et al. (2002), about 80% of existing bridges require some sort of scour mitigation.

From 1965 to 2005, over 1,500 bridges had collapsed in the United States, and scour was responsible for nearly 60% of these failures (Calappi et al. 2010). For example, 73 bridges collapsed during the 1985 floods in Pennsylvania, Virginia, and West Virginia (Richardson et al. 2001). Despite these collapses, it was not until 1987, when an interstate highway bridge failure over Schoharie Creek in New York killed ten people, that FHWA took action related to bridge scour monitoring. In addition to that, Hatchie River Bridge failure during the 1989 flood in Tennessee killed nine people. In fact, these two catastrophic failures are considered as the driving force that motivated extensive scour monitoring research in the United States (Lin et al. 2014).

As an immediate response to the 1987 Schoharie Creek Bridge failure, FHWA issued Technical Advisory T5140.20 titled "Scour at Bridges", accompanied by a publication titled "Interim Procedures for Evaluating Scour at Bridges" in 1988. The "Interim Procedures" divided the national scour problem at highway encroachments and crossings as 1) stream instability and channel movement, 2) long term degradation or aggradation, 3) live-bed or clear-water contraction scour, and 4) local scour at piers and abutments. It also addressed the methods for determining and preventing stream instability, channel movement, and long term elevation changes. As a part of the continued process, FHWA updated the "Interim Procedures" as Hydraulic Engineering Circular 18 (HEC-18) in 1991 (Richardson et al. 1993). HEC-18 remains the primary tool for predicting scour depth and prioritizing bridge monitoring schedules.

Since its establishment in 1991, HEC-18 has been used by bridge designers as a tool for determining scour depth and prioritizing bridge monitoring schedules (Schuring et al. 2010). However, many have observed that HEC-18 scour equations tend to over-predict scour depth for most geologic and hydraulic conditions because these empirical equations were developed from regression analysis of laboratory test results using coarse-grained soils. For example, during the early 1990s', the New Jersey Department of Transportation (NJDOT) analyzed nearly 2,400 state and county owned bridges using HEC-18 equations and identified 165 bridges as "scour critical". However, in 2006, NJDOT launched a Plan of action for the state's scour critical bridges and engaged the United States Geological Surveys (USGS) West Trenton office to conduct erosion monitoring in these bridges. USGS found that these bridges were not scour critical and were placed in the list solely based on HEC-18 analysis method (Schuring et al. 2010).

Although HEC-18 has served as a useful benchmark for scour prediction, a single manual based on granular soils is not applicable to all geologic, geotechnical, and hydraulic circumstances. Schuring et al. (2010) also indicated the necessity of proper sampling for scour prediction as median grain size and other geotechnical properties, of conventional surface grabbed samples used in HEC-18 equations may result in misleading scour depth. Therefore, it is desired to develop a viable geotechnical sampling protocol and perform site specific testing for accurately predicting erosion.

Numerous testing devices have been developed by researchers for directly measuring soil erosion in the laboratory and in the field. Some of the recent apparatuses for erosion measurements include the Sediment Erosion Rate Flume (SERF), the FLUME, the Jet Erosion Testing (JET) apparatus, the Erosion Function Apparatus (EFA), and the Ex Situ Erosion Testing Device (ESTD). For example, ESTD is the latest device utilized by FHWA in their manual to predict erosion in cohesive soils in the HEC-18 scour framework (Shan et al. 2015). Ultimately, the goal of these apparatuses is to predict the amount of scour by tracing the critical erosion (initiation of erosion). Again, the EFA, utilized in this study, is a flume style apparatus that measures the erosion of undisturbed samples collected in Shelby tubes. While soil erosion measurements are valuable using these devices, they are often time consuming. For example, a full test on a single sample takes eight hours to finish in EFA. For a vast purpose, such as statewide prioritizing of bridge

monitoring procedure, application of such time-consuming method may not be economically feasible.

The geology of Kansas is predominantly characterized by fine grained soils. Unlike coarse grained soil, where erosion is a function of median particle size only (Briaud et al. 2001), there is a complex system of factors that affects the erosion in fine grained soil. Fig. 1.1 illustrates the factors of erosion in fine grained soils. Effects of some of these factors on erosion are described in Chapter 3.

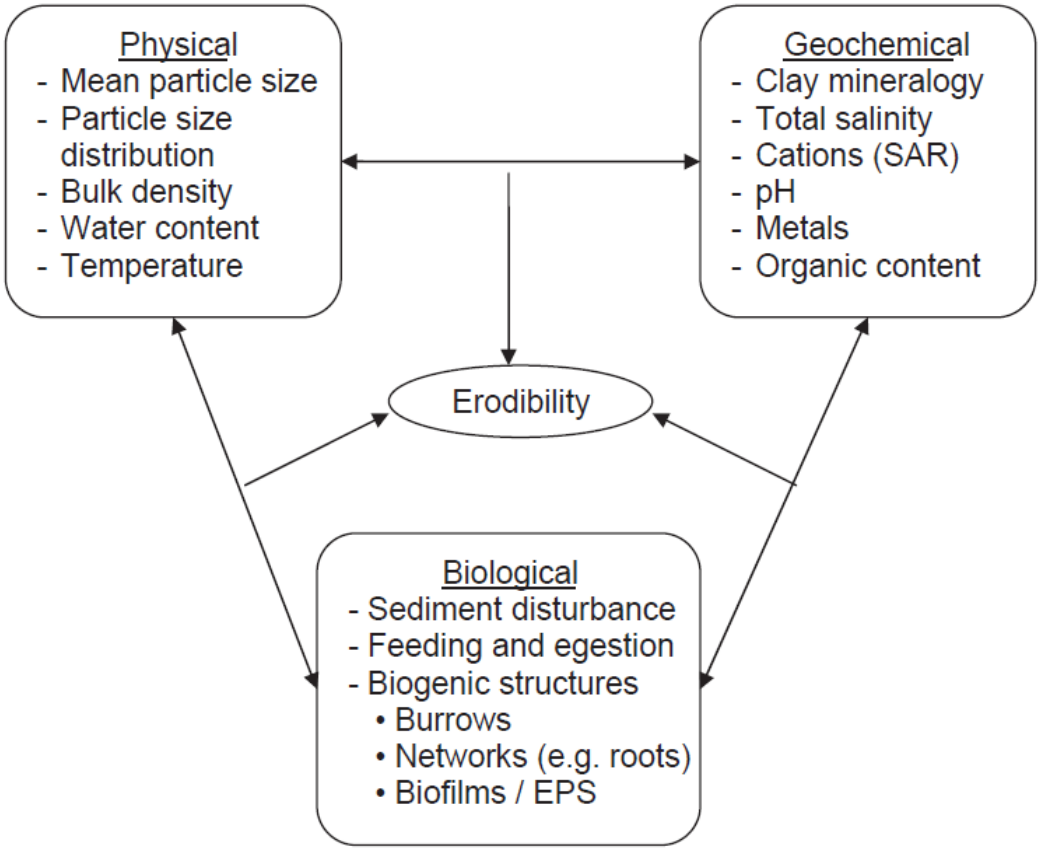

Fig. 1.1. Factors affecting erosion in fine grained soils (Grabowski 2011)

Electrical Resistivity (ER) is an intrinsic property of every material and is measured as the capability of opposing the flow of electrical current. Typical range of ER for different geo-materials are outlined in Table 1.1. ER survey has gained popularity as a geophysical testing method due to the improved data acquisition system and commonly used in fields such as geology, environmental science, archeology, and geotechnical engineering (Loke 1999; Dahlin 2001; Zonge

et al. 2005). Applications within these fields include determining depth to groundwater (Vaudelet et al. 2011), detecting varying subsurface geology (Chambers et al. 2013), and the presence of subsurface structures (Arjwech et al. 2013). The major factors that affect the ER of soils are particle sizes, water content, porosity, bulk density, mineralogy, and plasticity (Zhou et al. 2001). From Fig. 1.1, it is seen that many of this factors are exactly the same as the physical factors of erosion. Therefore, correlating erodibility and ER of soil can provide rapid in situ measurement of erodibility.

Hence, the objective of this study is to characterize the soil erosion potential, or erodibility by correlating the in situ ER of soil with the erodibility measurements from the Kansas State University Erosion Function Apparatus (KSU-EFA).

Table 1.1. Typical ER values of different geo-materials (Knight and Endres 2005; Lucius et al. 2007)

Material	Resistivity ($\Omega - m$)
Clay	5-100
Dry Sand and Gravel	>200
Saturated Sand and Gravel	<50
Sandstone	50-1,000
Shale	5-50
Conglomerates	1,000-10,000
Limestone and Dolomite	>1,000
Igneous Rocks	>1,000
Metamorphic Rocks	>1,000

Due to its geographic position in the upper Mississippi river basin, scour is a significant issue in Kansas. As mentioned earlier, erosion testing in EFA can provide essential data for predicting erodibility, but is time consuming. On the other hand, ER surveys are rapid and can collect large amount of subsurface data. Based on a correlation between ER and erodibility, ER data can be used to determine which bridge sites are vulnerable to scour and needs further testing for predicting erosion potential or, erodibility. In this way, a lot of time consuming erosion tests can be ignored

on sites that are not vulnerable to scour. ER survey can also determine which bridges should be closed or closely monitored during a flood event.

Samples were collected from 11 bridge sites throughout the eastern Kansas using Shelby tubes for erosion tests in EFA. Except one site, all other sites provided fine grained soils. ER surveys were also conducted in each bridge sites to obtain a two-dimensional distribution of subsurface ER. Data obtained in this manner was then used to correlate ER of soils with the erodibility of soils. The study results can be utilized for sorting out the vulnerable bridge sites at the primary level of scour monitoring. Additionally, the findings of this study can be used to predict critical shear stress for quantifying erosion potential in the secondary level.

There are five chapters in this thesis. The background, problem statement along with the research objective are described in Chapter 1. Chapter 2 represents a detailed literature review on different terms related to erosion, factors affecting erosion in soils as well as the history of erosion measurements. In addition, fundamentals of ER, different arrays of ER survey and data processing algorithm have been described in Chapter 2. Chapter 3 demonstrates the methodology of this research including the subsurface sampling, erosion tests as well as the field setup for ER survey. It is followed by chapter 4 where results and analysis of this research including necessary statistical analysis are provided. Finally, conclusions, findings, and recommendations for future research are provided in Chapter 5.

Chapter 2 - Literature Review

2.1 Soil Erosion

2.1.1 Erodibility and Erosion Rate

Erosion is the process of soil loss due to water flow. Erosion occurs when exerted shear forces by the flowing water overcome the resistive forces within the soil mass. The resistive forces from the soil include gravity, friction, cohesion and adhesion depending on the type of soil (Leeder 1999; Winterwerp and van Kesteren 2004). Erodibility is the measure of these resistive forces and can be seen as a threshold for erosion (Sanford 2008). This threshold for erosion can be measured in terms of critical shear stress. The process of erosion initiates once the shear stress exerted by the flowing water exceeds the critical shear stress of the soil. After this critical point, if flow continues, the amount of soil eroded per unit time is termed as the erosion rate. This simple concept concludes that, an erosion resistant soil is likely to have low erodibility, and an erosion prone soil will have a high erodibility. However, erodibility is not just a single number; it is often used to express the relationship between erosion rate, $\dot{z}$ and shear stress, τ.

2.1.2 Erosion in Various Types of Soil

While coarse grained soils erode as individual particles, fine grained soils erode as blocks. Slow motion video shows erosion as blocks in fine grained soils is associated with a combined rolling and plucking action (Briaud et al. 2001). Presence of attractive forces within the soil particles is the main reason for this type of erosion in fine grained soils. In coarse grained soils, resistance against erosion is controlled by the weight of soil. On the contrary, in fine grained soils, inter particular forces (i.e. cohesion and adhesion) provide the resistance against erosion in addition to the weight of soil (Grabowski et al. 2001). Due to this inter particular attractive forces, modeling of erodibility in fine grained soils becomes difficult which is further affected by the changes in amount and state of pore water pressure. Most common model for fine grained soil assumes that rate of erosion, $\dot{z}$ can be related to the flow variable, X in the following manner,

$$\dot{z} = kX^a \tag{2.1}$$

where, k is the soil erodibility factor (Moody et al. 2005). Rate of erosion, $\dot{z}$ is also expressed in terms of the excess shear stress such that,

$$\dot{z} = K_d(\tau - \tau_c)^b \tag{2.2}$$

where, $\dot{z}$ is the erosion rate; K_d is the coefficient of erodibility; τ and τ_c are the total shear stress and critical shear stress respectively; and exponent b is typically assumed to be equal to 1.0 in S.I. unit (Hanson et al. 1999). However, other researchers have showed that the value of b can vary from 1.0 to 6.8 (Van Klaveren and McCool 1998; Knapen et al. 2007). The rate of erosion $\dot{z}$ basically depends on the critical shear stress, τ_c which is difficult to estimate for fine grained soils.

2.1.3 Critical Shear Stress

Critical shear stress, τ_c is the shear stress exerted by flowing water on the soil surface that initiates erosion. Any shear stress having a value below τ_c, will not cause the soil to erode.

In coarse grained soils, only the weight of the soil resists the shear force. Briaud et al. (1999) found that the ratio of critical shear stress, τ_c and median grain size, d_{50} is 1.03 for coarse grained soils. Therefore, τ_c can be expressed by the following equation for coarse grained soils (Briaud et al. 1999),

$$\tau_c = d_{50} \tag{2.3}$$

where, d_{50} is the median grain size. Eq. 2.3 is also consistent with the equation derived from Shields (1936) data for critical shear stress, τ_c

$$\tau_c = 0.63\, d_{50} \tag{2.4}$$

where, d_{50} is the median grain size. However, studies have shown that these equations underestimate τ_c for fine grained soils and overestimates the amount of erosion (Hanson and Simon 2001). Many researchers have developed empirical equations of τ_c for fine grained soils based on laboratory tests. For example, Smerdon and Beasley (1961) proposed,

$$\tau_c = 0.16\,(PI)^{0.84} \tag{2.5}$$

$$\tau_c = 10.2\,(D_r)^{-0.63} \tag{2.6}$$

$$\tau_c = 3.54\ x\ 10^{-28.1 d_{50}}, \text{ and} \quad (2.7)$$

$$\tau_c = 0.493\ x\ 10^{0.0182 P_c} \quad (2.8)$$

for fine grained soils, where, PI is the plasticity index, D_r is the dispersion ratio, d_{50} is the median grain size and P_c is the percent clay by weight. Julian and Torres (2006) also developed an empirical relation for, τ_c as

$$\tau_c = 0.1 + 0.18(SC) + 0.002(SC)^2 - 2.34E + 5(SC)^3 \quad (2.9)$$

where, SC is the percent silt and clay. For fine grained soils, the value of critical shear stress is governed by the inter-particular forces and the chemistry between pore-water and flowing water; these are site-specific and very difficult to estimate (Heinzen 1976; Grissinger 1982; Knapen 2007). Again, the inter-particular forces within fine grained soil depends on different physical, chemical and biological factors. According to the study of Heinzen (1976), erodibility of fine grained soils depends mainly on the amount and type of clay; chemical composition of pore fluid; presence of organic matter; grain size distribution; stress history of the soil; soil temperature, pH, and water content of soil matrix. Review of the factors that affect erodibility of soil will be presented in the following section.

2.1.4 Factors Affecting Erodibility

Most of the factors that affect erodibility are linked to each other; changes in one factor is dependent on the interactions with other factors. These dynamically dependent factors are described below.

2.1.4.1 Soil Type (Median Particle Size, Relative Proportion of Particles)

Median grain size of soil particles is widely used as an important factor for erodibility in both coarse and fine grained soils. Hydraulic engineers worked to correlate the threshold velocity for erosion and particle size and the results are known as Hjulström Postma plots which are shown in Fig. 2.1 (Grabowski 2011). According to these plots, soil particles having either larger diameter than sand (e.g. boulders), or smaller diameter than sand (e.g. clay sized particles) will be difficult to be eroded.

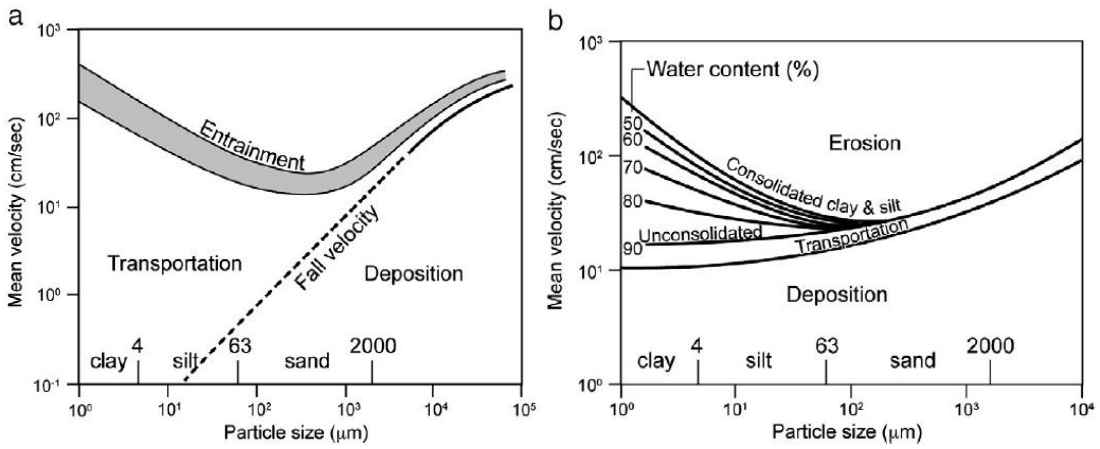

Fig. 2.1. Plots for threshold velocity against particle size: a) Hjulström; b) Postma (Grabowski 2011)

Two important restrictions should be noted while using these plots; only field observations were used for the particle diameters below 100μm and both the curves consider only the particle size neglecting other dependent variables. As mentioned earlier, laboratory tests on coarse grained soils demonstrate that increase in median grain size decreases the critical shear stress. However, for fine grained soils, the relation is generally opposite. Comprehensive laboratory studies on soil having particle size below 190 μm showed that critical shear stress decreases with increasing median grain size. The researchers concluded that silt sized particles behave as fine grained soil and the cohesion between organic materials supplies the inter-particular force (Johnson et al. 1994; Lick et al. 2004). According to a field survey on both consolidated and unconsolidated soil by Thomsen and Gust (2000) it was found that natural marine mud has an inverse correlation between critical shear stress and particle size. However, when particle size and floc density are proportional, a positive correlation between critical shear stress and particle size was observed during laboratory studies (Lau and droppo 2000; Droppo et al. 2001). Larger aggregates settle out under shear in this case and need higher critical velocity for erosion (Grabowski et al. 2011). Therefore, for fine grained soils, particle size can be either positively or negatively related to critical shear stress depending on various factors.

In addition to median particle size, erodibility is a function of particle size distribution. Several laboratory and field studies confirmed that critical shear stress increases with increasing clay contents. The increase in critical shear stress with increasing mud content (an equivalent term of clay content used in geological studies) is presented in Fig. 2.2 (Panagiotopoulos et al. 1997),

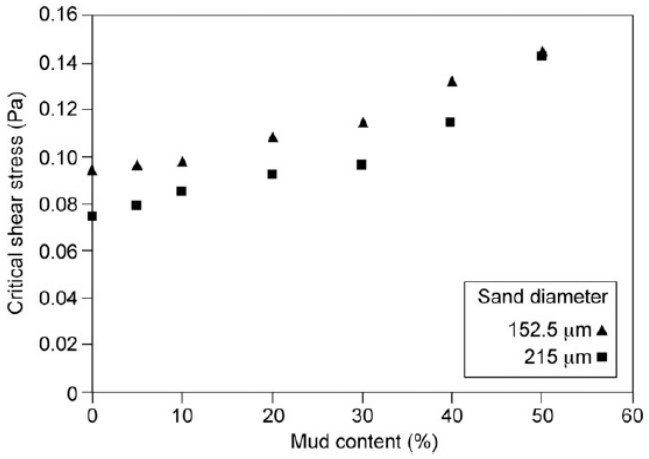

Fig. 2.2. Critical shear stress against mud content from artificial sediment mixtures (Panagiotopoulos et al. 1997)

This increase in erosion threshold can be attributed to the sand-clay adhesion or cohesion between clay particles. At low clay content (2%), clay particles adhere to sand or silt sized particles; at higher clay content (above 5%) the whole soil mass behaves as fine grained soil and the critical shear stress increases (van Ledden et al. 2004; Winterwerp and van Kesteren 2004). Beside these laboratory studies, many field studies have shown the increase in erosion threshold with increasing clay content. Houwing (1999) confirmed that, erosion rate decreases by two orders due to increased clay content (4-35%) for intertidal sediment. Despite these results, Aberle et al. (2004) found an inverse correlation between erosion thresholds and mud content. Debnath et al. (2007) explained this discrepancy by attributing the unexpected result to differences in particle size distribution. In order to avoid this difference in particle size distribution, several studies have suggested using volumetric clay content (Dickhudt et al. 2011).

2.1.4.2 Bulk Density and Water Content

Bulk density and water content mainly express the ratio of solid and liquid portion of the sediment (Rowell, 1994; Avnimelech et al., 2001) that gives an idea of the degree of consolidation in fine grained soils. When considered alone, critical shear stress increases with increasing bulk density. Dense sediment has up to 100 times lower erosion (Jepsen et al. 1997; Lick and McNeil 2001) and up to 5-8 times higher erosion threshold than less dense sediment (Bale et al. 2007). Amos et al. (2004) provided an empirical equation showing the relationship between wet bulk density and critical shear stress for natural lacustrine, estuarine, and marine muds as follows:

$$\tau_c = 5.44 \times 10^{-4}(\rho_b) - 0.28 \quad (2.10)$$

where, τ_c is the critical shear stress (measured in N/m^2) and ρ_b is the wet bulk density (measured in kg/m^3). The equation is valid for wet bulk densities from 800 to 2000 kg/m^3.

Water content also plays an important role for the erosive behavior in fine grained soils as the mechanical properties of clays are defined by the water content (Gillot 1987; van Ledden et al. 2004). When shear stress is applied on fine grained soils, two things can happen depending upon the degree of consolidation and liquidity index (I_L) . Unconsolidated clays such as fresh mud deposits having $I_L > 1$ are more prone to erosion than consolidated estuarine sediments that have $I_L < 1$ (Amarayan 1993; Bale et at. 2007). It is to be noted that liquidity index (I_L) is a measure of actual water content in relation to atterberg limits as in:

$$I_L = \frac{w - w_p}{w_l - w_p}; \quad (2.11)$$

where, w, w_l, w_p represent water content, liquid limit and plastic limit of soil respectively. In general, consolidated clays exhibit plastic deformation. When the threshold frequency is crossed, it will deform continuously and erode less. On the other hand, unconsolidated clays act like viscous fluid, where rate of erosion is directly proportional to shear stress (Grabowski et al. 2011).

2.1.4.3 Plasticity Index of Soil

Plasticity Index is defined as the measure of the ability of soil to be deformed while maintaining its shape. Plasticity index has a direct relationship to the cohesive strength and therefore, researchers have shown that the critical shear stress increases with increasing plastic index in the soil. Smerdon and Beasley (1961) developed an empirical relationship between critical shear stress and plasticity index based on flume studies and critical shear stress, τ_c was formulated as,

$$\tau_c = 0.16\ (PI)^{0.84} \quad (2.12)$$

where, PI is the plasticity index of soil. According to Dunn (1959) Plasticity index and sediment shear strength have a combined effect on critical shear stress and proposed an empirical equation

$$\tau_c = 0.01(\tau_s + 180)\tan(30 + 1.73\ PI) \quad (2.13)$$

where, τ_s is the sediment shear strength, and PI is the plasticity index of soil. Among the few recent studies, Shan et al. (2015) tested 17 laboratory prepared fine grained soil samples in ESTD and found that critical shear stress increases with increasing plasticity index. The empirical equation is combined of several other soil parameters and is formulated as

$$\tau_c = 0.1 \left(\frac{w}{F}\right)^{-2.0} PI^{1.3} q_u^{0.4} \tag{2.14}$$

where, w is the water content, F is the percent of particles finer than 0.075 mm, PI is the plasticity index, and q_u is the unconfined compressive strength of soil.

2.1.4.4 Water Temperature

There are at least two hypotheses exist that explain the proportional relationship between erodibility and water temperature. First, according to Mehta and Prachure (2000), the inter-particular bond between soil particles gets weak due to temperature increase in flowing water that directly results in an increase in the erodibility. This hypothesis is also reinforced by a previous research by cf. Zreik et al. (1998) that demonstrate a decrease in bulk strength of the sediment with an increase in water temperature. According to the second hypothesis, the viscosity of pore water is decreased with an increase in water temperature that contributes to higher permeability and increased velocity in the bed surface (Winterwerp and van Kesteren 2004).

Flume tests using homogenous clay bed were performed to demonstrate the effect of temperature on erodibility. Kelly and Gularte (1981) performed a flume test using homogenous illite beds that showed three times increase in erodibility when temperature of water was increased from 10 to 30 °C. Again, Zreik et al. (1998) found the sediment bed to erode more deeply when water temperature was increased from 20 to 29 °C.

There are other factors affecting soil erosion such as Sodium absorption ratio (SAR), total salinity, presence of dissolved ions, organic content. Although the contributions of these factors are important, were out of the scope of this research.

2.1.5 History: Erosion Rate Measurement

Over the years, researchers have concentrated to develop the relationship between erosion rate and shear stress for different soil types. Among the few laboratory apparatuses, the rotating cylinder

apparatus (Moore and Masch 1962) is one of the earliest. In this apparatus, there are two cylinders. The outer one rotates around the inner stationary cylinder, while the gap between them is filled up with eroding fluid. Motion is generated on the fluid by the rotating outer cylinder, which, in the process, applies shear on the soil sample. Center rod measures the applied torque. When erosion initiates, the critical shear stress can be obtained from this torque and erosion rate is measured by weighing the sample regularly. The rotating cylinder is advantageous in directly measuring the shear stress; however, its use is limited by sufficient cohesive strength of the soil (Crowley et al. 2012a). A schematic of the rotating cylinder apparatus is given in Fig. 2.3.

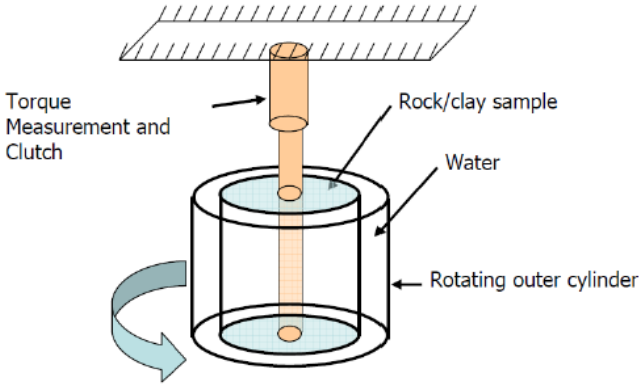

Fig. 2.3. Schematic of rotating cylinder apparatus (Sheppard and Bloomquist 2005)

Later, in 1986, Rohan et al. proposed the drill-hole apparatus. In this apparatus, a 6.35 mm diameter hole is made through the soil sample and water flow is passed along the hole. The shear stress is obtained by observing the head loss of water in the hole, while erosion rate is obtained by weighing the eroded soil. This test method very closely resembles the pinhole test (ASTM 2013b).

Other preliminary apparatuses include the vertical grid oscillator, the EROMES system, the rotating disk device (Salim et al. 2011). Again, several attempts have been made to measure erodibility using specially designed flumes.

The Erosion Function Apparatus (EFA) and the Sediment Erosion Rate Flume (SERF) are the relatively recent devices throughout the United States for measuring soil erosion rate and shear stress. Similar to other flume-style devices, SERF (Fig. 2.4) is also characterized by a rectangular flume design, for rectangular shape allows the flow to be fully developed over a very short length (Trammel 2004). Since a partitioned flume permits testing of different sections varying in length and design, the device was built in sections. In addition to that, these test sections can be used for

different sizes of sample diameter. An 1100-gallons reservoir is used in SERF that has a series of baffles to facilitate turbulence reduction and settling of the suspended sediments. There are two motor pumps and water discharged through the pump is carried through a 100 mm pipe past the paddlewheel flowmeter and enters the flume through a 0.3 m circular to rectangular transition section. A flow straightener is also used in the flume to achieve a fully turbulent flow. The flow then passes through another 0.3 m long rectangular section followed by 0.6 m rectangular section. A shear stress sensor and an access hatch are located at 0.5 m from the upstream of the 0.6 m rectangular section. There are two pressure taps on both sides of shear stress sensor. These taps are also connected to pressure transducers. As such, a comparison between computed shear stress from the pressure drop and actual shear stress from the sensor is afforded. A viewing window is located parallel to the shear sensor that facilitates not only real time viewing but also recording through closed-circuit television (CCTV). The test cylinder, which carries the sample, may consists of either an acrylic cylinder, a PVC cylinder or a Shelby tube. The lead screw stepper motor is positioned under the test cylinder. As erosion takes place, a piston attached to the lead screw lifts the sample within the sample cylinder. A detailed description of the functions of SERF can be found in Crowley et al. (2012b). The SERF is advantageous for its ability to measure instantaneous erosion rate and suitability to test both fine and coarse grained soils. However, a major drawback of the device is its inability to maintain constant shear stress.

Fig. 2.4. Photograph of Sediment Erosion Rate Flume (SERF) (Crowley et al. 2012)

2.1.6 Erosion Function Apparatus (EFA)

2.1.6.1 EFA: Description

Originally developed for fine grained soils, Erosion Function Apparatus (EFA) can be used for any type of soil that can be sampled in a Shelby tube to quantify the rate of erosion. The soil sample is collected by pushing an ASTM standard Shelby tube of 88.9 mm outside diameter. In EFA, water is flowed at different velocities within a 1.33 m long rectangular flume that has a cross-sectional dimension of 101.6 mm x 50.8 mm. A flow straightener is used at one end of the rectangular flume. The rectangular flume has a circular opening in its bottom to insert top end of the Shelby tube containing the soil sample. This top of Shelby tube (or the sample) is kept flush with the bottom of the rectangular flume. As erosion takes place, the sample is pushed from the other end of the sample with the aid of a piston. A leak-proof connection is established by a snug fit and an O-ring. The velocity of water flow in the rectangular pipe can be maintained using an interactive LCD screen. The average flow velocity range is 0.1 to 6 m/s. A diagram explaining the concept is shown in Fig. 2.5.

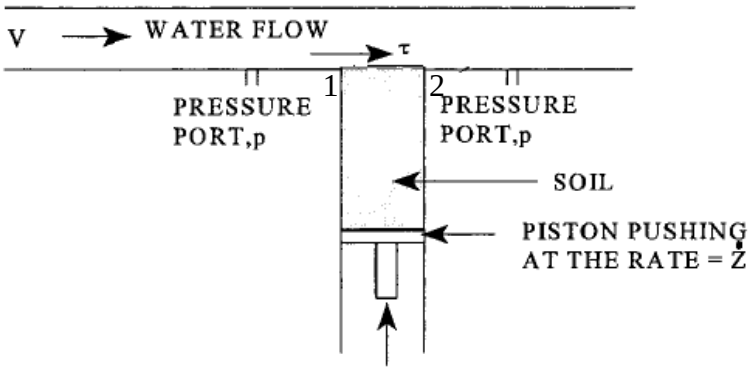

Fig. 2.5. Concept of EFA (Briaud et al., 1999)

2.1.6.2 A Typical Test in EFA

Erosion tests are conducted on soils at their in situ water content. For this reason, if the test is not performed on the day of sampling, then the sample should be kept at a humidity controlled room. During the test, the bottom of the sample is to be placed over the piston and the top is kept flush with the base of the rectangular flume. At first, the sample is eroded under the minimum velocity (typically 0.5 m/s) for one hour. When the sample erodes, the piston is pushed upward to keep the

soil flush with the bottom of the flume. The amount of sample eroded is equal to the length of sample lifted by the piston. This amount can be directly obtained from EFA screen. The same procedure is repeated for velocities 1, 2, 3, 4, 5, and 6 m/s so that, erosion rate (mm/h) can be obtained for each velocity. The objective of erosion tests in EFA is to obtain the plot of rate of erosion, $\dot{z}$ (mm/hr) versus shear stress, τ (N/m^2). A photograph of KSU-EFA is given in Fig. 2.6.

Fig. 2.6. Photograph of KSU-EFA

2.1.6.3 Obtaining Test Results in EFA

Erosion rate, $\dot{z}$ for different velocities can be found using the following formula,

$$\dot{z} = \frac{h}{t} \tag{2.15}$$

where, h = length of sample eroded, and t = duration of the test. One of most challenging tasks is to determine an appropriate shear stress. In early days of erosion testing, the shear stress was measured using the pressure difference between the upstream and downstream of the eroding surface. However, this method was erroneous, as the shear stress due to the roughness of the eroding surface was not considered. According to Briaud et al. (1999), Moody chart (Moody 1944) provides more accurate shear stress estimate for EFA and was used in this project. In this method the shear stress, τ is calculated using the following formula:

$$\tau = \frac{1}{8} f \rho v^2 \tag{2.16}$$

where, f = friction factor obtained from Moody chart, ρ = density of water and v = mean velocity of flow in the pipe. Determination of f is a complex process that depends on specific test and discussed elaborately in chapter 3.

2.2 Electrical Resistivity

2.2.1 Electrical Resistivity Survey

Electrical resistivity (ER) survey, one of the most widely used near surface geophysical methods, has gained more popularity since mid-1900s due to advancements in data acquisition system (Loke 1999; Dahlin 2001; Zonge et al. 2005). An electric current I (measured in amperes) is injected into the ground through a current electrode and resulting voltage potential V (measured in volts) is measured across another pair of electrodes. The impedance of earth, $Z = \frac{V}{I}$ (measured in volts/ampere) is calculated, which is used to calculate resistivity, ρ (measured in Ω-m).

2.2.2 Electrical Resistivity Derivation

Resistivity, ρ (measured in Ω-m) is a material property and is determined using the equation

$$\rho = \frac{RA}{L} \tag{2.17}$$

where, R is the resistance (measured in Ω), A is the corss-sectional area (measured in m^2) and L is the length (measured in m) of any cylindrical sample of that particular material (Fig. 2.7).

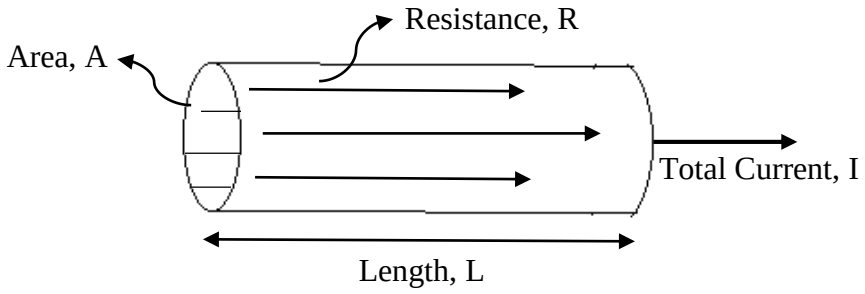

Fig. 2.7. Definition of resistivity

Now, for deriving the subsurface resistivity equation, a hypothetical soil medium having uniform resistivity ρ is considered (Fig. 2.8). Current I is injected at the center of the spherical coordinate of the soil medium and the return electrode is placed at the infinity.

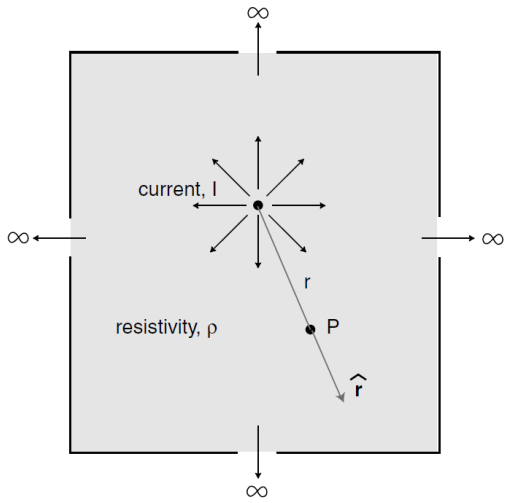

Fig. 2.8. Current injection at a homogenous soil medium (Everett 2013)

Voltage of any point P (Fig. 2.8) within the electrical field is the work done by electric field to move a test charge from infinity to that point. Hence, the voltage, V at point P (Fig. 2.8) will be the product of electric field and the distance moved by the charge so that,

$$V = \int_{\infty}^{r} E.dr \tag{2.18}$$

where, E is the magnitude of the electric field and dr is the infinitesimal distance. Again from Ohm's law, electric field magnitude, E can be expressed as in the following mannar,

$$E = \frac{I\rho \mathbf{r}}{4\pi r^2} \tag{2.19}$$

where, I is the current, ρ is the resistivity and r is the distance of point P from origin. Substituting the value of E from eq. 2.19 to eq. 2.18,

$$V = \int_{\infty}^{r} E.dr = \int_{\infty}^{r} \frac{I\rho r}{4\pi r^2}.dr = \frac{I\rho}{4\pi r} \tag{2.20}$$

where, all the variables are already defined. Eq. 2.20 is the equation for resistivity in the subsurface, where electric source is assumed to be within the subsurface and the electric field is

spherical (Fig. 2.8). In case of ER survey, the electric current is injected from a source electrode, and injection point should be on the surface (Fig. 2.9). The current cannot flow through the non-conducting air; as such, it flows radially outward creating a hemispherical electric field. The area term $4\pi r^2$ in eq. 2.20 (derived for spherical electric field) can be modified by $2\pi r^2$ for hemispherical (Fig. 2.9) electric field and the voltage, V for ER survey can be measured as:

$$V = \frac{I\rho}{2\pi r} \tag{2.21}$$

where, the variables are defined before. Now, the voltage difference between two points P and Q in the ground (corresponding to the pair of voltage electrodes) can be measured using the following equation:

$$V_{PQ} = V_P - V_Q = \left(\frac{I\rho}{2\pi}\right)\left[\frac{1}{r_P} - \frac{1}{r_Q}\right] \tag{2.22}$$

where, V_P, V_Q are the voltages and r_P, r_Q are the distances from source to electrode for P and Q electrodes respectively.

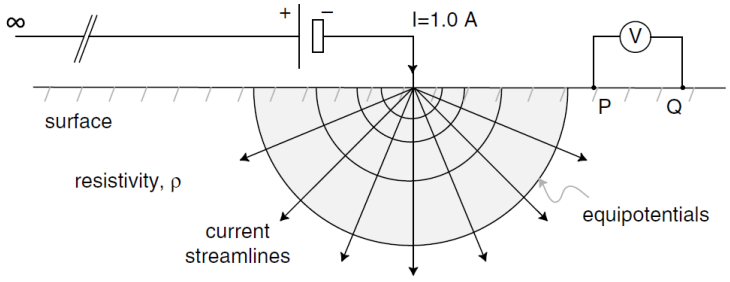

Fig. 2.9. Voltage measurement between P and Q due to injected current from a source (Everett 2013)

Note that, eq. 2.22 is derived for only one current electrode (source). During ER survey, two pairs of electrodes are used, namely, current pair (A, B) and voltage pair (P,Q). Electrode A (source) sends the current into the ground and electrode B (sink) receives it and voltage difference is measured between electrodes P and Q (Fig. 2.10). Therefore, for two current electrodes A and B, the combined equation for voltage difference between P and Q will be,

$$V_{PQ} = V_P - V_Q = \left(\frac{I\rho}{2\pi}\right)\left[\frac{1}{r_{AP}} - \frac{1}{r_{AQ}} - \frac{1}{r_{BP}} + \frac{1}{r_{BQ}}\right] \tag{2.23}$$

where, the variables are self-explanatory, for example, r_{AP} is the distance between current electrode A to voltage electrode P. This is the equation for voltage difference measurement between P, Q voltage electrodes by the ER survey using a total of 4 electrodes. In the field, V_{PQ} and I is measured. Therefore, rearranging the eq. 2.23 to solve for the unknown ρ, it is obtained,

$$\rho = \left(\frac{2\pi V_{PQ}}{I}\right)\left[\frac{1}{r_{AP}} - \frac{1}{r_{AQ}} - \frac{1}{r_{BP}} + \frac{1}{r_{BQ}}\right]^{-1} \tag{2.24}$$

where, all the variables are defined and eq. 2.24 is the final equation for calculating resistivity in the subsurface. Note that, during this derivation it is assumed that the whole subsurface is homogenous with uniform resistivity, ρ. Therefore, the resistivity, ρ obtained in this way is termed as apperant resistivity, ρ_a. Eq. 2.24 can be also written in the following way,

$$\rho_a = \frac{V_{PQ}}{I} * k \tag{2.25}$$

where, $k = 2\pi\left[\frac{1}{r_{AP}} - \frac{1}{r_{AQ}} - \frac{1}{r_{BP}} + \frac{1}{r_{BQ}}\right]^{-1}$ is called the geometric factor for the 4-electrodes system.

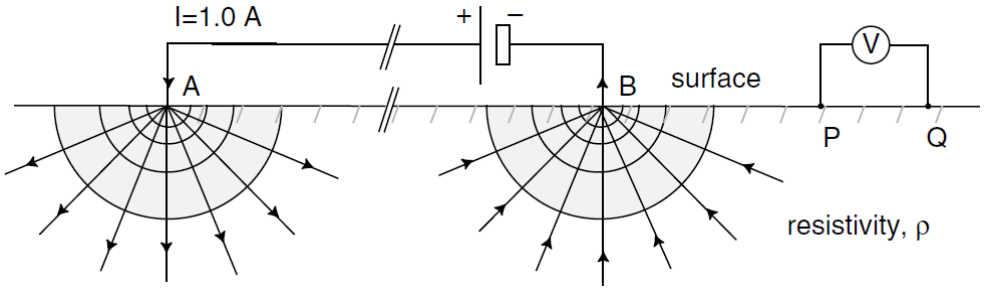

Fig. 2.10. Voltage measurement between P and Q with source A and sink B (adapted from Everett 2013)

2.2.3 Different Electrode Arrays

The derivation for apparent resistivity shown in Section 2.2.2 used 4-electrodes system. Now, with the advancement of data acquisition system, multiple 4-electrodes can be combined or modified to form different arrays to gather the needed data. Depth of penetration, signal to noise ratio, lateral resolution, and ease of deployment are some of the prime criteria upon which the choice of an electrode configuration depends (Everett 2013). However, it is to be mentioned that, irrespective

of the array type, depth of penetration will increase as the spacing between the electrode increases. Described below are some of the most widely used 4-electrode configurations.

2.2.3.1 Schlumberger Array

Schlumberger array is especially designed for determining resistivity profile along the depth beneath a single point; which is also called sounding (Everett 2013). The voltage electrodes PQ are centered at the same position with constant distance *2a* (Fig. 2.11). The current electrodes AB are also centered at the same position but their separation increases during voltage measurements. It is a common practice to express apparent resistivity ρ_a as a function of half of spacing between current electrodes AB. An apparent resistivity profile using Schlumberger array can achieve comparatively large depth of penetration when the spacing between current electrodes are large. However, the lateral resolution using this particular array is poor. The signal to noise ratio is moderate to good, because all the voltage readings are taken at the center of the array which confirms better signal (Everett 2013). The geometric factor *k* for Schlumberger array is:

$$k = \frac{1}{2}(n-1)(n+1)\pi a \tag{2.26}$$

where, n is the ratio of distances of the current electrode B and the voltage electrode Q from the center of the array and a is the half of the voltage electrode separation as shown in Fig. 2.11.

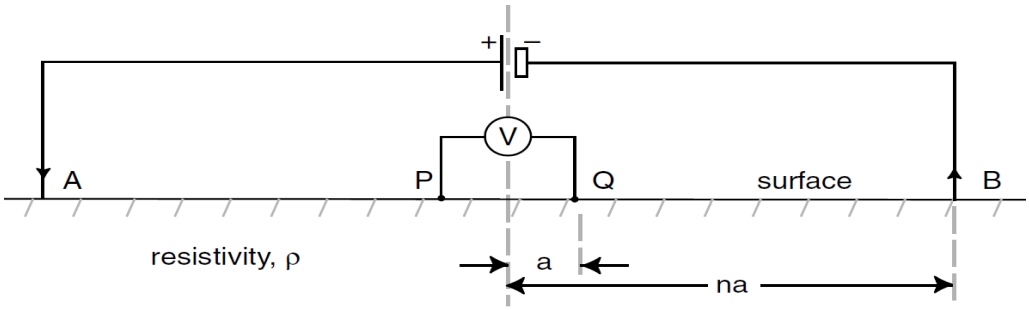

Fig. 2.11. Schlumberger array circuit diagram (Everett 2013)

2.2.3.2 Wenner Array

Wenner array became popular after the pioneering work carried out by the University of Birmingham (Loke 1999). Opposite to Schlumberger, Wenner array is more suitable for lateral distribution of apparent resistivity. The voltage electrodes PQ remains in the middle of the two

current electrodes AB. There is a constant distance a between the electrodes (Fig. 2.12). During the voltage measurement, the whole configuration moves laterally; as such, the separation between the electrodes does not change (Fig. 2.12). Wenner array is particularly used when lateral profiling of resistivity is expected at a constant depth (Everett 2013). The depth of lateral distribution of subsurface resistivity increases with increasing a. Unlike Schlumberger, where the current electrodes keeps going further apart, in Wenner array signal to noise ratio is better because current electrodes are always at the same distance keeping the voltage electrode at the center (Everett 2013). The geometric factor k for Wenner array is:

$$k = 2\pi a. \tag{2.27}$$

where, a separation between electrodes.

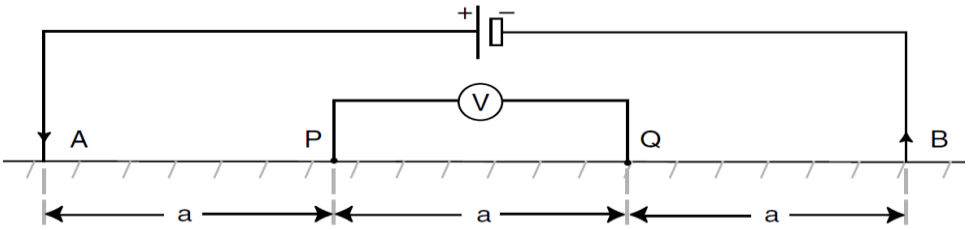

Fig. 2.12. Wenner array circuit diagram (Everett 2013)

2.2.3.3 Dipole-dipole Array

Dipole-dipole is one of the most popular arrays in resistivity applications (Loke 1999). The spacing between current electrodes AB is a, as same as the spacing between the voltage electrodes PQ (Fig. 2.13). The depth of penetration increases as n or a increases. The geometric factor k for dipole-diploe array is:

$$k = \pi n(n+1)(n+2)a. \tag{2.28}$$

where, a is the separation between electrodes and n is the ratio of separation between two electrode pairs and a. The dipole-dipole provides good resolution with depth; thus has the advantage of both Schlumberger and Wenner array. One of the drawbacks of the dipole-dipole array is the poor signal to noise ratio and it gets worse with increasing value of n. For this reason, value of n is limited to

eight. Also, the voltage measurement near to the voltage electrodes are prone to near surface homogeneities.

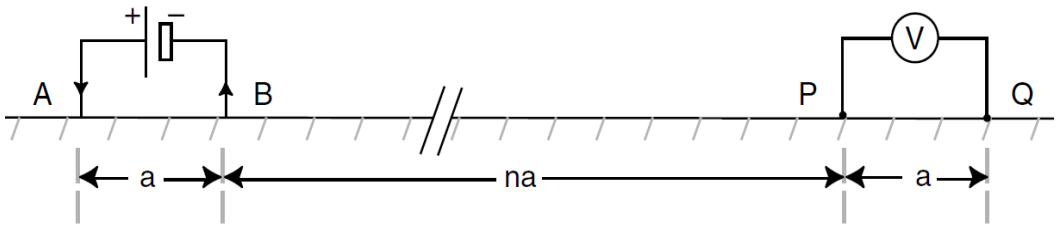

Fig. 2.13. Dipole-dipole array circuit diagram (Everett 2013)

2.2.4 Sensitivity Functions

Due to any change in the magnitude of subsurface resistivity, a corresponding change in measured voltage is occurred. A sensitivity function, S, is defined as the degree to which a change in the resistivity of a section of the subsurface will influence the voltage potential measured by the array. Higher sensitivity yields greater influence of measured voltage for subsurface resistivity (Everett 2013). In order to determine the sensitivity function, S, for several four-electrode configurations, Furman et al. (2003) used a 2-D analytic solution for small change in the resistivity of a buried cylindrical homogeneity of radius L. This process was repeated for various positions of the cylindrical heterogeneity to obtain cumulative sensitivity function, $CS(x, y)$. Cumulative sensitivity function, $CS(x, y)$, is the summation of the sensitivities due to the changes in voltage measurements caused as the cylindrical heterogeneity is placed at various subsurface locations. The results of the analysis of Furman et al. (2003) for four different arrays are shown in Fig. 2.14. The contours of $CS(x, y)$ at 25, 50, 75, and 90% level are shown. For example, a $CS(x, y)$ of 90% shows that, 10% of the measurement sensitivity of the array lies outside the 90% contour. These plots indicate the region of subsurface to which a given measurement array is sensitive. For example, Wenner array (Fig. 2.14 (a)) is particularly more sensitive to the ground beneath the midpoint of the array with a moderate sensitivity across the length of the array. For this reason, Wenner array is suitable for lateral resistivity profiling. On the contrary, Schlumberger array (Fig. 2.14 (b)) is mainly sensitive around the near surface, just below the potential electrodes than elsewhere, justifying their suitability in vertical sounding purpose. Dipole-dipole array (Fig. 2.14 (c)) is sensitive under the current and potential electrodes and less sensitive between the electrodes. In comparison to the other arrays, for dipole-dipole array, the area enclosed by cumulative

sensitivity at 90% is the least. This verifies the fact that, dipole-dipole array has poor signal to noise ratio and high sensitivity to near surface homogeneity. Lastly, Fig. 2.14 (d) shows a non-uniform partially overlapping array possessing a high sensitivity along both vertical and horizontal direction.

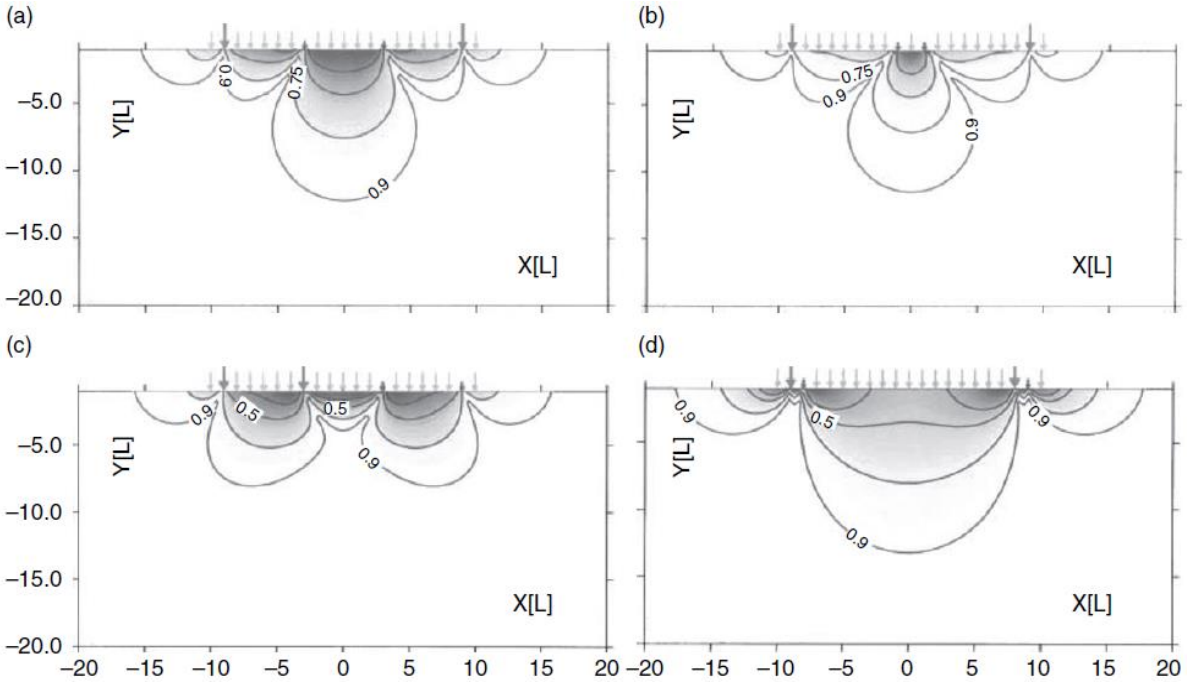

Fig. 2.14. Cumulative sensitivity functions for different array: (a) Wenner; (b) Schlumberger; (c) Dipole-dipole; (d) partially overlapping (larger, bold arrows show current electrodes and smaller, bold arrows show potential electrodes) (Furman et al., 2003)

2.2.5 Resistivity Pseudosections

The subsurface apparent resistivity data from multi-electrode survey are expressed using the pseudosections. To plot the data from a 2-D imaging survey, the pseudosection contouring method is normally used (Loke 1999). As shown in Fig. 2.15, for a dipole-dipole array, the apparent resistivity ρ_a corresponding to the current electrodes AB and voltage electrodes PQ is plotted at the intersection of the 45° lines (with horizon) drawn from the centers of the electrodes. The same procedure is repeated until all the current and potential electrode pairs are covered. In this way, a rough estimation of true subsurface resistivity is obtained because maximum sensitivity of the ground surface for a particular voltage measurement is found near the midpoint of the four-electrode configuration at a depth of one-half of the separation of the current-potential electrode

pairs (Everett 2013). However, the pseudosection gives a distorted picture of the subsurface because the shape of the contours depends on the type of array used as well as the true subsurface resistivity.

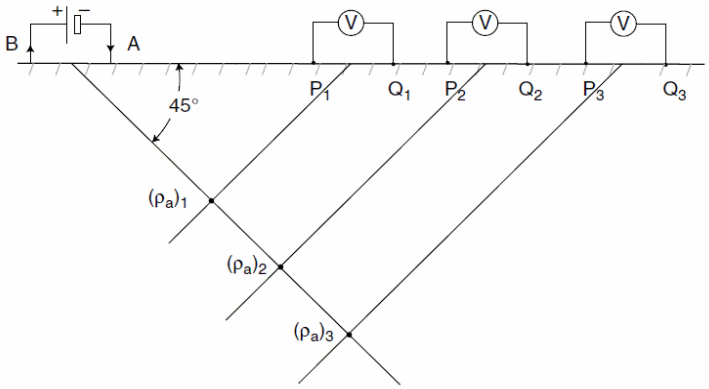

Fig. 2.15. Resistivity pseudosection for a dipole-dipole array (Everett 2013)

2.2.6 Data Processing: Forward Modeling and Data Inversion

The objective of conducting an ER survey is to estimate the subsurface electrical properties (resistivity or conductivity). The apparent resistivity (ρ_a) measured in the field can be converted to inverted resistivity though an iterative process that includes forward modeling and data inversion. Forward modeling mathematically models the apparent resistivity for given electrical properties and boundary condition using partial differential equations such as Poisson's equation (Binley et al. 2005). Inversion, on the other hand, produces the subsurface distribution of electrical properties (model parameter) from a set of given measurements (data); this relation is expressed in Fig. 2.16.

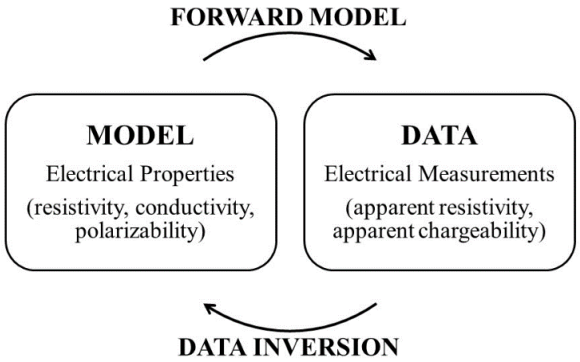

Fig. 2.16. Forward modeling and data inversion processes (adapted from Binley et al. 2005)

In a two-dimensional (2D) ER survey, the earth model is 2D but the electrical field due to a point source is 3D; hence, the problem is considered 2.5D and the domain of investigation is discretized for solving the 2.5D forward modeling problem (AGI 2007). In order to find the forward solution, the 3D partial differential equation is Fourier transformed into a 2D partial differential equation

$$\frac{\partial}{\partial x}\left(\frac{\partial V}{\partial x}\right) + \frac{\partial}{\partial z}\left(\frac{\partial V}{\partial z}\right) - k^2 \sigma V = -I.\delta(x).\delta(z) \tag{2.29}$$

where, V and k are the scaler electrical potential and wavenumber in the Fourier transfer domain, I is the injected electric current and σ is the electrical conductivity as function of (x, z).

For a horizontally layered earth where σ varies only with z, solution of the Poisson's equation can also be obtained. For instance, in case of Schlumberger electrode configuration, the apparent resistivity can be given by the Stefanescu integral (Koefoed 1979):

$$\rho_a(r) = r^2 \int_0^\infty T(\lambda)\, J_1(\lambda r)\, \lambda\, d\lambda \tag{2.30}$$

where, r is the half of the distance between two electrodes, J_1 is the Bassel's first order function and Kernel $T(\lambda)$ is a function of the given layer thickness and resistivities and λ is an integration variable (Binley et al. 2005). In all of these cases, the distribution of conductivity (inverse of resistivity) is approximated by a mesh of individual cells having constant conductivity. The potential is then calculated after solving linear system of equations deriving from the discretized differential equation (such as eq. 2.29) and boundary condition (Binley et al. 2005). Both finite element (FE) and finite difference (FD) method can be used in EarthImager. Although FD is fast, FE method provides more accurate solution to forward modeling problem and was used in this research. Again, EarthImager also offers both Cholesky decomposition (CD) and conjugate gradient (CG) methods as forward equation solver. For this research, CD was applied as this method is more accurate when more than 20 electrodes are used (AGI 2007). Dirichlet boundary condition is used for this research.

To formulate the inverse problem, a model vector **m** is constructed which comprises of electrical properties of the subsurface. This model vector contains the conductivities (σ) (inverse of resistivity) of the individual elements or cell in the FE mesh used in the forward modeling. That is:

$$m_j = ln\sigma_j \tag{2.31}$$

where, j = 1,2,…,M and the logarithm stands for probable large variation of earth conductivities. Similarly, the measured apparent resistivities (ρ_a) can be stored in another vector **d** as follows:

$$d_i = -ln\rho_{a_i} \tag{2.32}$$

where, i = 1,2,…,N and logarithm stands for the same reason as in the previous vector. The negative sign is used to convert measured apparent resistivity into conductivity and make the dimension constant with eq. 2.31. The inverse problem now is to determine a model **m** so that it reproduces (using the forward modeling) the data **d** with a certain level of uncertainty. To account for the non-uniqueness of inversion and the presence of error prone data, additional constraints should be imposed in the inversion (Binley et al. 2005). For this reason, inverse problem is solved as a regularized optimization problem (Tikhonov and Arsenin 1977), in which the following objective function is minimized:

$$\psi(\mathbf{m}) = \psi_d(\mathbf{m}) + \alpha\psi_m(\mathbf{m}) \tag{2.33}$$

where, $\psi_d(\mathbf{m}) = \|\mathbf{W}_\mathrm{d}[\mathbf{d} - \mathbf{f}(\mathbf{m})]\|^2$ is a measure of data misfit between measured and calculated (using forward modeling) resistivities and $\mathbf{W}_\mathrm{d} = \mathrm{diag}(\frac{1}{\varepsilon_1}, \frac{1}{\varepsilon_2}, \ldots, \frac{1}{\varepsilon_N})$ is a data weighting matrix associated with the uncorrelated data errors ε_i (Binley et al. 2005). Again, $\psi_m(\mathbf{m})$ is a stabilizing model objective expressed as $\psi_m(\mathbf{m}) = \|\mathbf{W}_\mathrm{m}[\mathbf{m} - \mathbf{m}_\mathrm{ref}]\|^2$ that includes certain model constraints with respect to the reference model $\mathbf{m}_\mathrm{ref}$, and $\mathbf{W}_\mathrm{m}$ is the model weighting matrix similar to $\mathbf{W}_\mathrm{d}$. The regularization parameter, α controls the tradeoff between influence of data misfit and model objective function (Binley et al. 2005). The reference model, $\mathbf{m}_\mathrm{ref}$ can have the value of expected model parameter and/or the result of previous inversion. It can also be assigned to a homogenous half space or the null vector if sufficient information is not available.

Eq. 2.33 can be simplified by applying gradient search method. Choosing Gauss-Newton approach iterations are continued, where at each step, k, the linear system of equation:

$$\left(\mathbf{J}_k^\mathrm{T}\mathbf{W}_\mathrm{d}^\mathrm{T}\mathbf{W}_\mathrm{d}\mathbf{J}_k + \alpha\mathbf{W}_\mathrm{m}^\mathrm{T}\mathbf{W}_\mathrm{m}\right)\Delta\mathbf{m}_k = \mathbf{J}_k^\mathrm{T}\mathbf{W}_\mathrm{d}^\mathrm{T}\mathbf{W}_\mathrm{d}[\mathbf{d} - \mathbf{f}(\mathbf{m}_k)] - \alpha\mathbf{W}_\mathrm{m}^\mathrm{T}\mathbf{W}_\mathrm{m}(\mathbf{m}_k - \mathbf{m}_\mathrm{ref}) \tag{2.34}$$

is solved for a model update $\Delta\mathbf{m}_k$. Here, $\mathbf{J}_k$ is the Jacobian sensitivity matrix, and $J_{ij} = \frac{\partial d_i}{\partial m_j}$ is evaluated for the current model $\mathbf{m}_k$. The iteration process $\mathbf{m}_{k+1} = \mathbf{m}_k + \Delta\mathbf{m}_k$ continues until $\psi_d\ (m_k)$ matches the desired data misfit target value. For starting the iteration, initial model $\mathbf{m}_0$ is taken equal to $\mathbf{m}_{\text{ref}}$, if available (Binley et al. 2005).

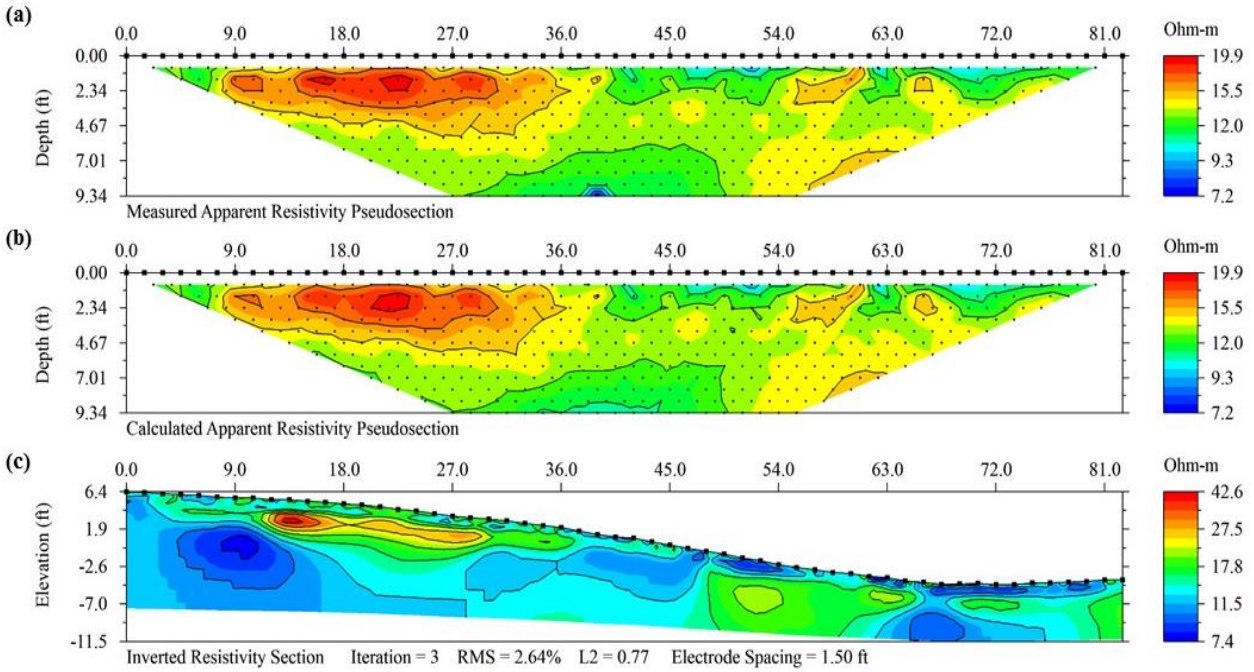

Fig. 2.17. Results of an electrical resistivity survey conducted near a bridge abutment of Kansas-4 highway: (a) measured apparent resistivity pseudosection; (b) calculated apparent resistivity pseudosection; (c) inverted resistivity section

There are four methods of inversion available in EarthImager; namely, forward modeling only, damped least squares inversion, smooth model inversion, and robust inversion. For this research, smooth model inversion or Occam's inversion was chosen. The smooth model inversion, which is based on Gaussian distribution of data errors, searches for the smoothest possible model that fits the data to an *a-priori* Chi-squared statistic. The whole inversion process can be summarized in the following few steps.

After the ER survey and before starting the inversion process in EarthImager, only distribution of measured apparent resistivity (ρ_a) is known (Fig. 2.17 (a)) based on the measured current(I), voltage difference (V), and electrode geometry (k). In the first iteration, the starting model is constructed based on the average resistivity or a prior knowledge of subsurface resistivity

distribution. Then, using the starting model, forward modeling is performed to predict the apparent resistivity distribution. At this stage, the root mean square (RMS) error between predicted (or, calculated) and measured resistivity is determined using

$$RMS = \sqrt{\frac{\sum_{i=1}^{N}\left(\frac{d_i^{Pred} - d_i^{Meas}}{d_i^{Meas}}\right)^2}{N}} * 100\% \qquad (2.35)$$

where, N = total number of measurements, d_i^{Pred} = predicted data at ith iteration, and d_i^{Meas} = measured data at ith iteration. Based on the data misfit, a linearized inversion is performed for a model update ($\Delta \mathbf{m}_k$). The resistivity model is updated and the new inverted resistivity distribution (Fig. 2.17 (c)) is obtained. Forward modeling, using the updated model is performed in the next iteration to obtain calculated resistivity (Fig. 2.17 (b)). If the new RMS error (between measured and calculated resistivity) at this stage meets the desired criteria, then inversion stops; otherwise few more iterations may be performed. The algorithm of forward modeling and inversion based on the measured apparent resistivity and initial resistivity model is given in Fig. 2.18.

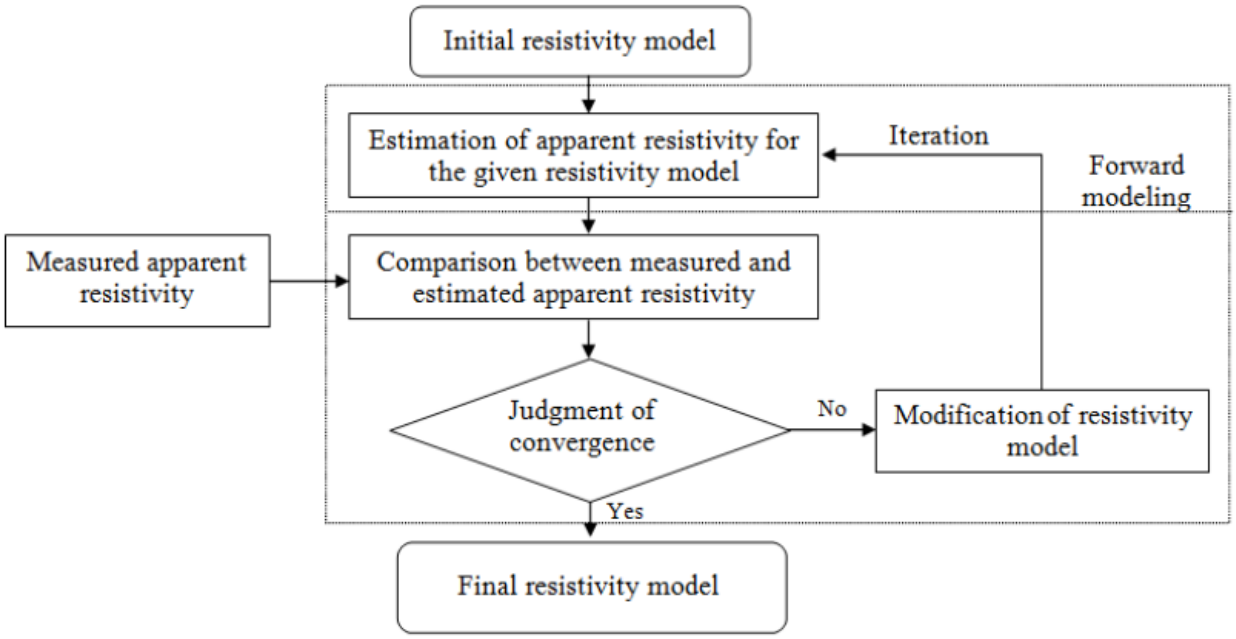

Fig. 2.18. Algorithm of forward modeling and data inversion (Arjwech 2011)

2.2.7 Factors Affecting Subsurface Electrical Resistivity

2.2.7.1 Soil Type (Median Grain Size, Index Properties, Relative Particles)

The Electrical conductivity (opposite of resistivity) is dependent on the electrical charge density at the surface of the solid constituents. The higher electrical charges associated with clay particles lead to higher conductivity than the coarse grained soil (Fukue et al. 1999). Moreover, due to the presence of larger voids, coarse grained soils show very low conductivity (or, high resistivity). Giao et al. (2003) collected 25 clay samples around different places of the world and found that the ER value of them ranges from 1 to 12 Ω m. On the contrary the ER value of sand has a very wide range (20-200 Ω m) (Everett 2013).

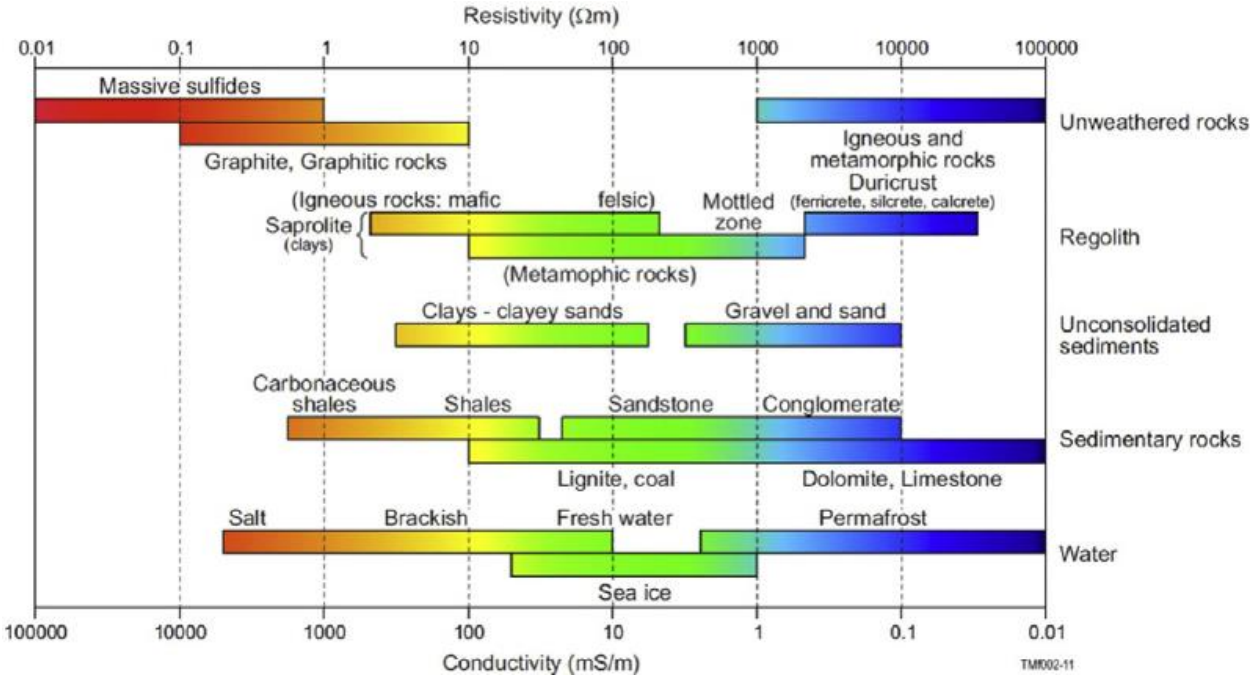

Fig. 2.19. Typical ranges of electrical resistivities of earth materials (Palacky 1987)

Inzaki et al. (2008) conducted an integrated geophysical investigation on an earthen levee in central Japan that was affected by a severe flooding in 2006. As a course of this geophysical investigation, ER survey was conducted along a 3 km stretch of the earthen levee which consisted of both fine and coarse grained soils (median grain size varying roughly from 0.01 to 1.5 mm). When median

grain size was plotted against apparent ER in log scales (Fig. 2.20) a direct relationship was clearly observed between the two parameters.

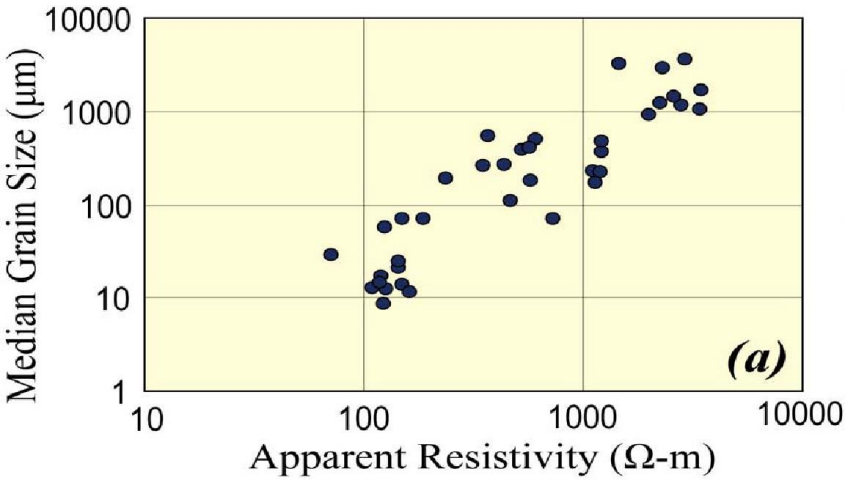

Fig. 2.20. Median grain size against apparent resistivity (Injaki et al. 2008)

Relationship between ER and soil index properties can also be found in the literature. For instance, Abu-Hassnaein et al. (1996) conducted the ER tests on several compacted clay samples in lab. Fig. 2.21 shows the relationships between ER and liquid limit (LL) and plasticity index (PI) for four samples (A, B, C, D). A trend of decreasing ER with increasing LL and PI is evident. However, a discrepancy is seen in these relationships as one of the data points (for sample C) largely deviates from the trend. When ER of sample C was measured using the particles passing No. 200 sieve, the ER value was more consistent with the trend (shown with the hollow circle in Fig. 2.21).

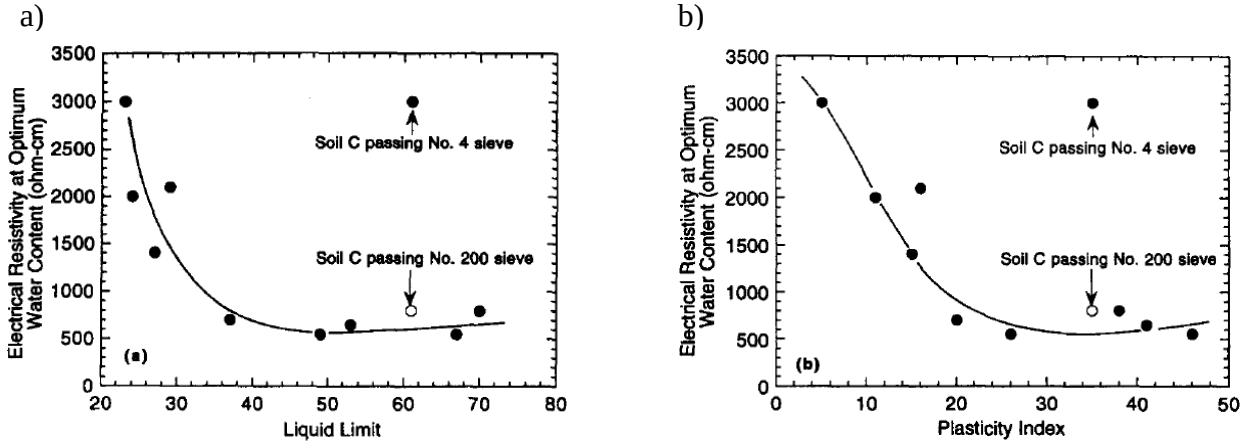

Fig. 2.21. Relationships between ER and, a) liquid limit and, b) plasticity index (Abu-Hassanein et al. 1996)

Electrical resistivity can also be related to percentage of fines and percent of coarse fraction. Abu-Hassanein et al. (1996) used the same clay samples to correlate ER with percent fines and coarse fraction and the correlation is shown in Fig. 2.22. It is evident from Fig. 2.22 (a) that the ER values decrease with increasing percent fines. This is due to the reason that soils with more fines contain more conductive clay particles and have higher specific surface that improves surface conductance (Kwader 1985). Fig. 2.22 (b) shows that ER values increase with increasing percent coarse fraction. The coarse fraction is primarily made of quartz and feldspar that have high electrical resistivity (Keller and Frischknecht 1966). As a consequence, the higher the coarse fraction, the higher will be the electrical resistivity.

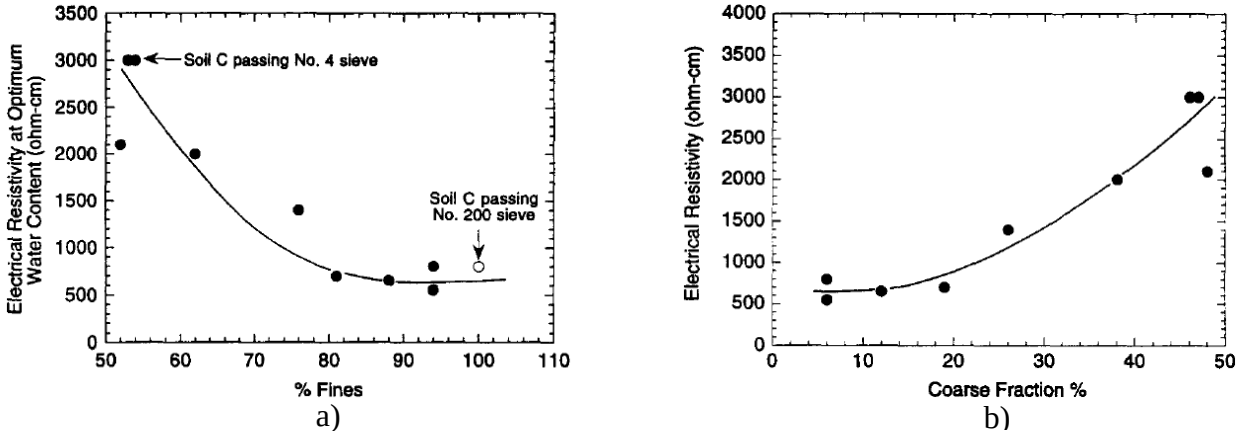

Fig. 2.22. Relationship between ER and: a) percent fines; b) percent coarse fraction (Abu-Hassanein et al. 1996)

2.2.7.2 Water Content and Unit Weight

Electrical current in soil is dependent on the displacement of ions in pore-water; therefore, water content is identified as one of major factors that affects ER of soils (McCarter 1984). Kibria et al. (2012) performed laboratory ER tests for four samples at varying water content, while keeping the dry unit weight constant. The results are shown in Fig. 2.23 that indicates that as water content increases, the ER value decreases. It is also evident that the water content has more significant effect on ER in the region of lower water content values as the curve becomes flatter after 40% water content.

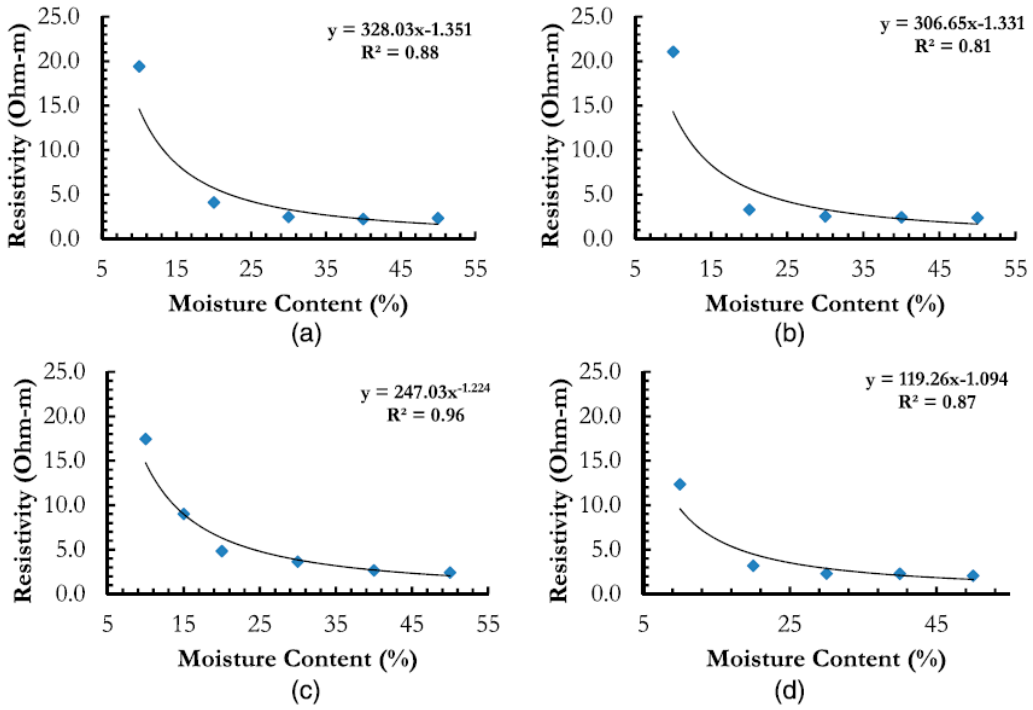

Fig. 2.23. Relationship between ER and water content of four samples (Kibria et al. 2012)

Kibria et al. (2012) also developed a relationship between ER and moist unit weight of soil using the same four samples (Fig. 2.24). The water content was constant at 18% for all the samples. It is evident from Fig. 2.24 that ER values decrease with increasing moist unit weight. It is also notable that, variation of ER with moist unit weight is more prominent in the lower moist unit weight region for all the four samples. This inverse relationship between ER and moist unit weight can also be understood by the study of Abu-Hassanein et al. (1996). When moist unit weight is increased (keeping water content constant), the degree of saturation increases. Therefore, more bridging occurs between soil particles. In addition, an increased moist unit weight is associated with remolding of clay clods, elimination of interclod voids, and reorientation of particles- all these factors decrease the ER values (Abu-Hassanein et al. 1996).

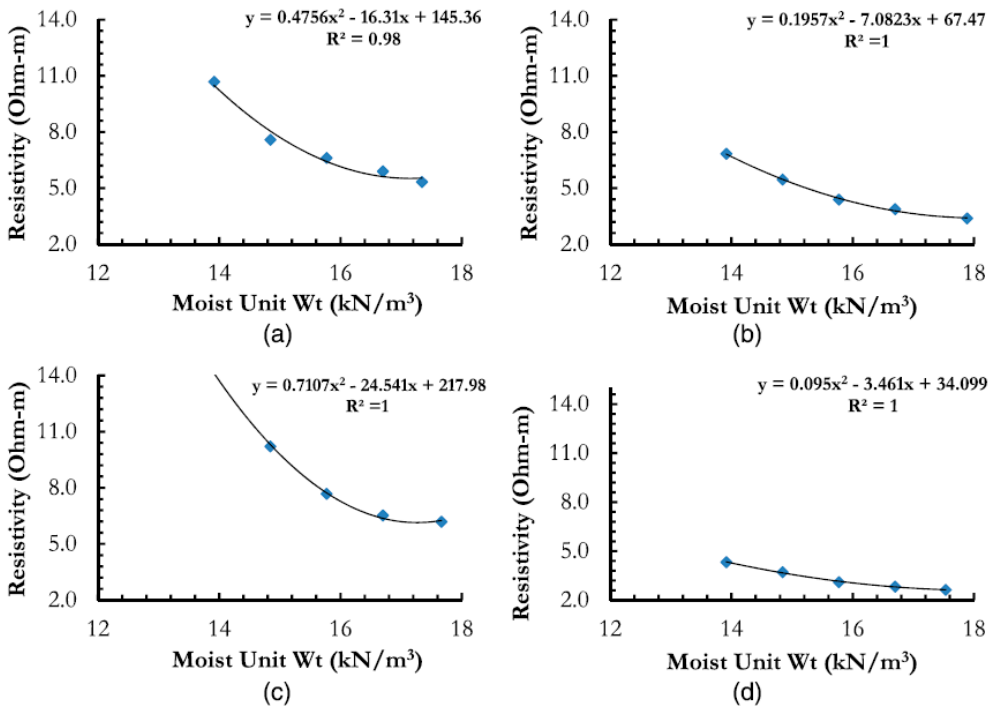

Fig. 2.24. Relationship between ER and moist unit weight of four samples (Kibria et al. 2012)

The water content discussed so far, was gravimetric water content. Kibria et al. (2012) also correlated electrical resistivity with volumetric water content, which is shown in Fig. 2.25. It shows that, ER decreases with increasing volumetric water content, as was the case for gravimetric water content and regression coefficient of this correlation was 0.64.

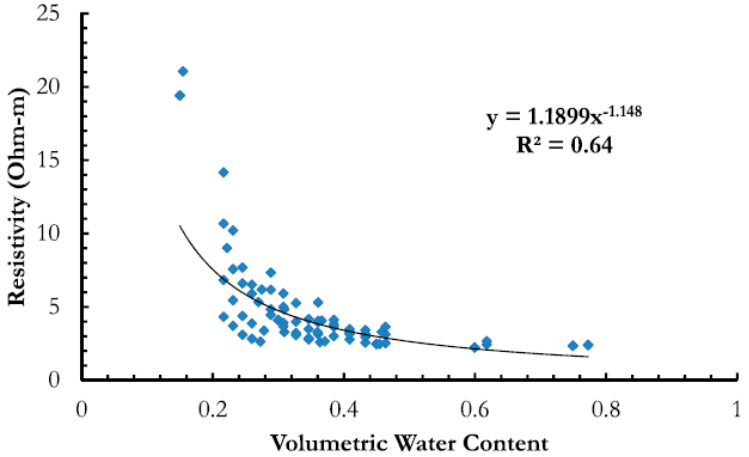

Fig. 2.25. Relationship between ER and volumetric water content (Kibria et al. 2012)

From the results of these laboratory tests, Kibria et al. (2012) proposed an empirical formula to correlate ER with several soil parameters as

$$\rho = 16.366 \left[\gamma_m * \frac{w}{1+w}\right]^{-1.148} \tag{2.36}$$

where, ρ is the ER, γ_m is the moist unit weight of soil and w is the gravimetric moisture content of soil.

2.2.7.3 Temperature

Ion ignition increases with increasing temperature when viscosity of fluid decreases. Therefore, electrical resistivity of soil decreases with increasing temperature (Samouelian 2005). Abu-Hassanein et al. (1996) correlated the ER with temperature using soil samples A, B, D (described in section 2.2.7.1). These samples were compacted with optimum water content before measuring ER at different temperatures. The semi-logarithmic graph at Fig. 2.26 shows the relationship between ER and temperature of these three samples and it is seen that ER decreases with increasing temperature. An abrupt change in the ER occurs at the freezing temperature (0℃) due to the change in di-electric constant (Keller and Frischknecht 1966). The slope of the graph (after 0℃) is known as thermometric coefficient (C_{TE}). The average value of C_{TE} for the three samples was 0.0078 $℃^{-1}$, which is very close to the C_{TE} of tap water (0.0080 $℃^{-1}$) (Abu-Hassanein et al. 1996). The linear relationship after freezing point (above 0℃) in Fig. 2.26 can be used to normalize the ER measured at any temperature above 0℃ to the ER measured at 25℃ (Abu-Hassanein et al. 1996) using

$$\rho_T = \rho_{25} 10^{-(C_{TE})(T-25)} \tag{2.37}$$

where, T is the soil temperature in ℃, ρ_T is the ER at temperature T℃ in Ω-m, and ρ_{25} is the ER at 25℃ in Ω-m.

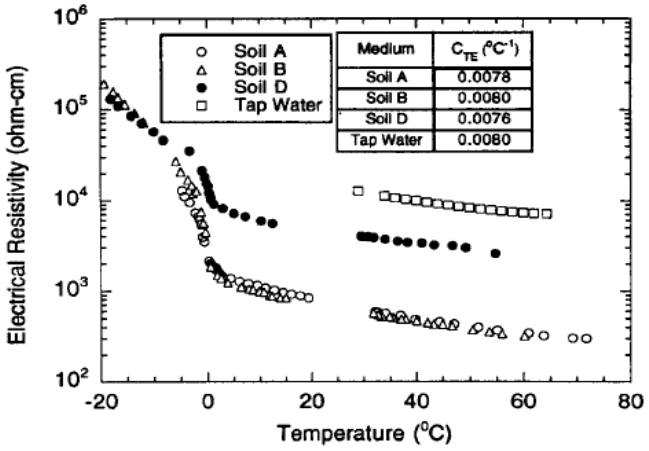

Fig. 2.26. Relationship between ER and temperature (Abu-Hassanein et al. 1996)

2.3 Summary

This chapter presented a review on erosion and electrical resistivity of soils from engineering, geological and geophysical point of view. In the first part of this chapter, necessary definitions and equations regarding erosion were provided so that erodibility, critical shear stress for erosion can be understood. A detailed discussion of the factors affecting erosion in soils was given with references. A brief history of the previous apparatuses that were used for measuring erosion rate was given. The equations and assumptions associated with erosion rate measurement in EFA was presented that will be used in this research.

In the second part, fundamentals on electrical resistivity were discussed with necessary theory and derivations. The data processing comprises of two mutually related complex process: forward modeling and inversion. Necessary theory and assumptions related to forward modeling and data inversion were discussed in a brief so that the algorithm of the data processing software: EarthImager can be understood. Finally a brief discussion on the factors affecting electrical resistivity of soils was provided.

It is observed that there are some mutual factors such as: soil type, water content, plasticity index, unit weight of soil, temperature that affect both erosion and electrical resistivity of soils. It is very inspiring that, despite these mutual factors, no direct attempts were found in the literature to correlate erosion rate with the electrical resistivity of soil: which is the main driving force for this research.

Chapter 3 - Methodology

3.1 Overview

This chapter includes the research methodology for this project including field and laboratory work. In order to correlate the erosion potential of soil with electrical resistivity, samples were collected from bridge sites that were selected by Kansas Department of Transportation (KDOT). Electrical resistivity (ER) surveys were also conducted at the bridge sites. Erosion tests, soil classification, and analysis of the ER survey were done in the KSU geotechnical laboratory. The overall methodology is shown in the following diagram (Fig. 3.1).

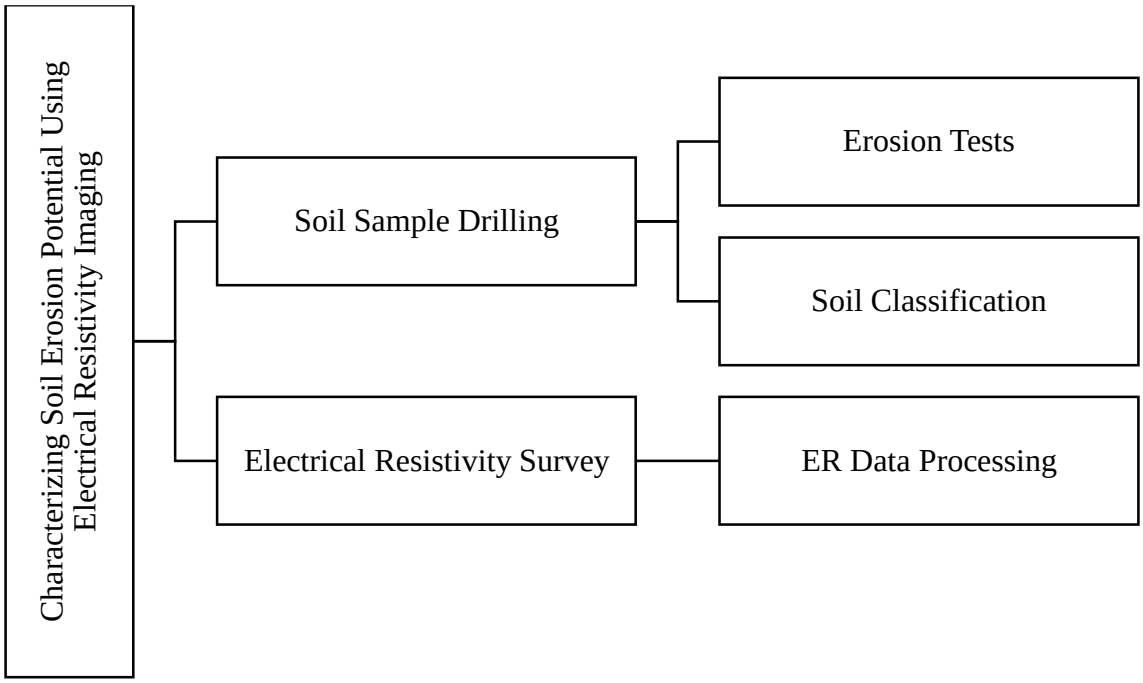

Fig. 3.1. Flow diagram of the research methodology

3.2 Listing of Sites

KDOT selected eleven sites around Kansas for this study. Depending on the accessibility, soil samples were collected as close to the stream as possible. ER surveys were conducted so that the borehole was in the center of the array- this also affected the sample drilling position. A short description of these sites is given in Table 3.1 (KDOT 2015) and a map containing all the sites is presented in Fig. 3.2 (Google Maps 2016).

Table 3.1. Selected sites for the research (KDOT 2015)

No.	Bridge ID**	County	KDOT District	KDOT Area Office	Highway	Scour Critical*	Perennial Stream	Crossing
1	043-0030	43-Jackson	1	4-Topeka	US-75	8	Unk	Straight Creek
2	058-0008	58-Marshall	1	1-Horton	US-36	3	Yes	Black Vermillion River Drg.
3	058-0025	58-Marshall	1	5-Wamego	K-9	3	Unk	Robidoux Creek
4	007-0013	7-Brown	1	1-Horton	US-73	3	Yes	Walnut Creek
5	015-0005	15-Cloud	2	2-Mankato	US-24	3	Unk	Cris Creek
6	085-0108	85-Saline	2	4-Ellsworth	K-4	3	No	Dry Creek
7	085-0146	85-Saline	2	4-Ellsworth	K-4	3	Unk	East Dry Creek
8	016-0041	16-Coffey	4	1-Iola	K-58	3	Unk	Neosho River Drainage
9	019-0056	19-Crawford	4	4-Pittsburg	K-126	3	Unk	East Cow Creek
10	050-0067	50-Labette	4	4-Pittsburg	US-400	3	No	Hickory creek
11	054-0030	54-Linn	4	2-Garnett	US-69	3	Yes	Big Sugar Creek

Notes:
*A value of 4 or less
indicates a scour critical bridge
**Bridge ID = County Number-Bridge Serial Number

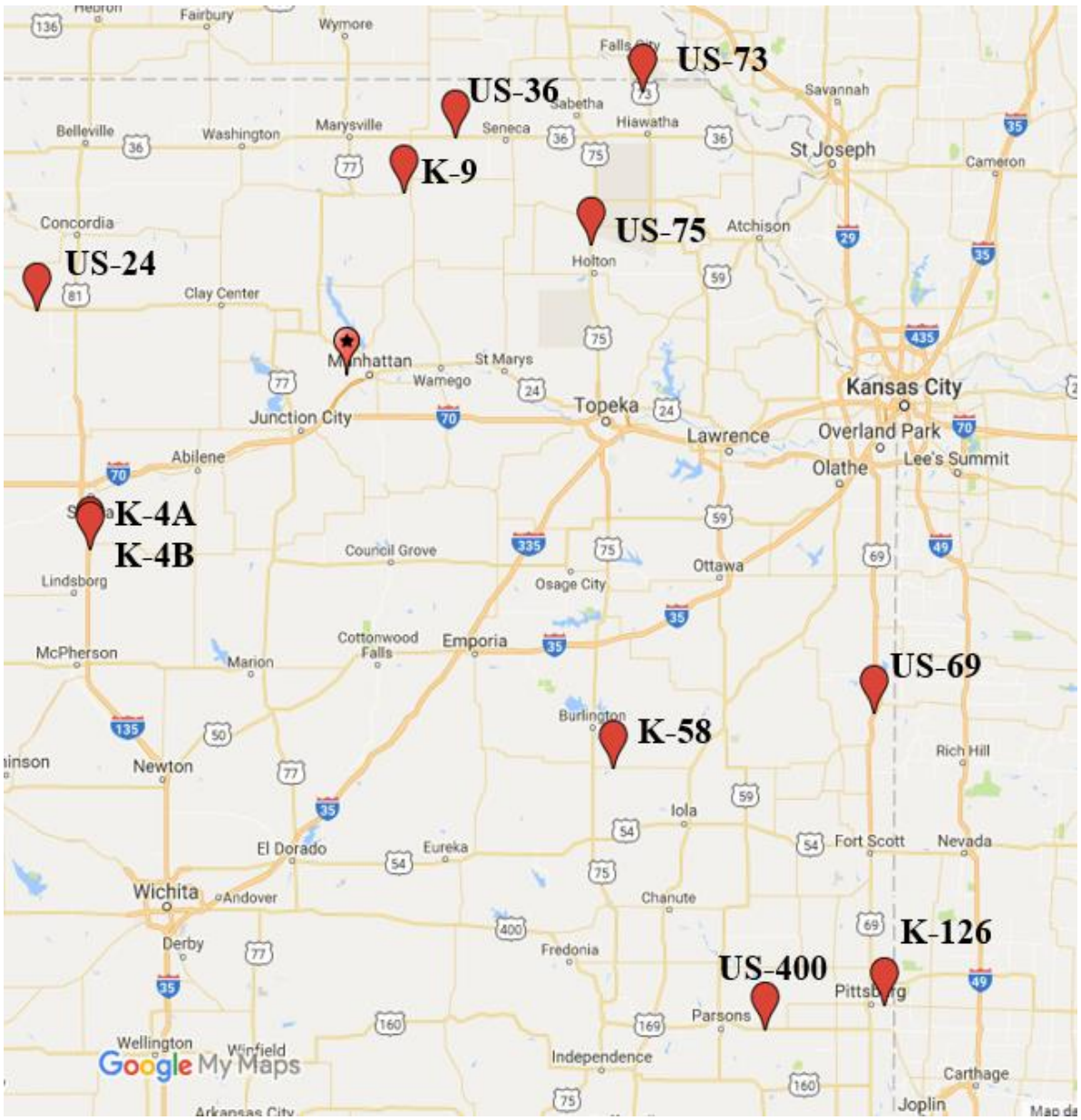

Fig. 3.2. Map containing research sites (Google Maps 2016)

3.3 Soil Sample Drilling

Thin-walled Shelby tubes were used following ASTM standard D1587 (ASTM 2015) to collect undisturbed soil samples at each bridge site. A schematic of the tube is given in Fig. 3.3. The tubes were 88.9 mm (3.5 in) in diameter and 914.4 mm (36 in) long. Five 609.6 mm (2 ft) long samples were collected at each of the eleven sites at a fixed drilling position. As a result, the total drilling depth was approximately 3.1 m (10 ft) at every site.

The drilling operations were conducted by KDOT. Prior to drilling, one of the constraints was to find the optimal location for the borehole using the following criteria:

- Foreign soil materials are often used to construct embankment near bridge abutment and pavement. Therefore, drilling position should not be very close to the pavement or bridge abutment so that the collected samples represent the native geology of the site.
- There should be approximately 12.5 m (41 ft) of accessible land on either side of the potential borehole. This length was required for the ER survey line (discussed later in this chapter).
- There should not be any utility line or fiber optic cable underneath the soil.

Once these criteria were met, the drill rig was moved to the selected drilling position. Loose material and vegetative cover were removed from the center of the casing to avoid sample disturbance. Expected sample recovery (609.6 mm) was marked on the Shelby tube and the sampler was advanced without rotation by pushing the tube to the marked point. To increase the sample recovery, minimum 10 minutes delay was applied before withdrawing the tube. This delay ensures to build up enough skin friction between the soil and tube. Special care was taken to minimize sample disturbance. For example, especially for highly plastic soils, the Shelby tube was slowly rotated to shear the sample at the bottom and maximize recovery.

Sample recovery and unconfined shear strength of the sample were measured using a measuring tape and pocket penetrometer respectively. A field log was also recorded at the time of subsurface exploration which included the name of the project, location, sampling equipment, KDOT drillers and engineers name, sample number; depth of retained sample; length of push and recover.

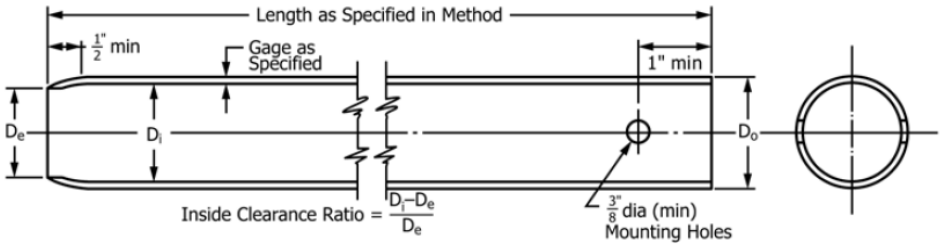

Fig. 3.3. Typical longitudinal and cross section of an ASTM standard Shelby tube; where D_e, D_i, D_o are end, inner and outer diameters respectively (ASTM 2015)

ASTM standard D4220 (ASTM 2014b) was followed for preserving and transporting soil samples to maintain the in situ conditions for erosion testing. After sampling and measuring the sample recovery, both ends of the Shelby tube were sealed using plastic end-caps. To provide for more protection to preserve the in-situ moisture content, duct tape was used at both ends and the whole tube was wrapped using plastic sheet. Samples were labeled with the bridge number and sampling depth. If the ER survey was not conducted on the same day due to the limitations of the drilling schedule, the borehole location was marked with respect to at least two permanent objects. Once back at the university the samples were stored in the 100% humidity controlled room until taken to the lab for erosion tests. The samples were designated according to their highway name and the order of sampling. For example, the top sample from US-400 site was designated as US-400 #1.

Fig. 3.4. a) Sample drilling with the drill rig; b) close view of drilling

3.4 Erosion Test

Erosion test refers to the measurement of the erodibility or erosion rate of soils (mm/hr) at different velocities in an Erosion Function Apparatus (EFA). The length of the piston rod in the EFA is such that it allows a maximum length of 406.4 mm (16 in) of sample to be tested. For this reason, Shelby tubes containing the sample were cut and 381 mm (15 in) was used for the erosion test. The rest of the sample was used for classification according to the USCS (Coduto 1999). The erosion test was run using cold tap water. As mentioned earlier, water temperature and soil temperature affect erosion. Therefore, water temperature was maintained between 15 ± 2 ℃ for all tests by continuous

filling and swamping of the water reservoir with cold tap water and soil sample was at room temperature (20℃).

3.4.1 Test Description

The goal was to test each sample under six different velocities in the EFA. The range of velocities chosen for each sample varied depending on the sample type. The range of velocities for samples that had large amount of fines and high plasticity was typically 0.50 to 6.00 m/s (i.e. 0.50, 1.00, 2.00, 3.00, 4.00, 5.00, and 6.00 m/s); whereas, samples with large amount of coarse particles were tested from 0.30 to 1.30 m/s (i.e. 0.30, 0.50, 0.75, 0.90, 1.10, 1.30 m/s) velocity range. If a sample erodes very fast at a certain velocity, the next velocity should be chosen smaller than the previous velocity. It will ensure enough data points under different velocities before running out of sample.

Each sample was brought from the humidity controlled room right before the test to ensure that the test was run at the in-situ moisture content. The moisture content was measured before the test according to ASTM standard D2216 (ASTM 2010a). Initially the sample was placed on the platform over the piston head and the outside of the tube was tightened with a bracket attached to the platform. This ensured that only the soil moved when the piston was pushed to extrude the sample (Fig. 3.5 (a)). With the help of a crank wheel the platform was lifted so that the top of the tube (and sample) were flush with the bottom of the flume (Fig. 3.5 (b)). A flow button on the interactive LCD screen should be pressed for initiating water flow and input of the preferred water velocity is given. Temperature and velocity of water were measured by a temperature sensor and a flowmeter respectively, and displayed continuously on the LCD screen and recorded with time. Erosion occurred if the resistive forces of the soil sample were less than the force due to applied shear stress by water flow. When erosion occurred, sample was extruded using the motor controlled piston so that the soil sample is flush with the bottom of the flume again. The piston can be moved any amount from 0.1 to 100 mm and movement rate can be regulated (0.2 to 0.5 mm/s). Ideally, the test was conducted for 60 mins (1 hr) under each velocity. However, for highly erodible soil, the duration of test under each velocity was reduced to 30 mins or less to ensure enough sample remained for testing under other velocities. The rate of erosion (mm/hr) was obtained by dividing the total amount of erosion (mm) by the duration of the test (hr).

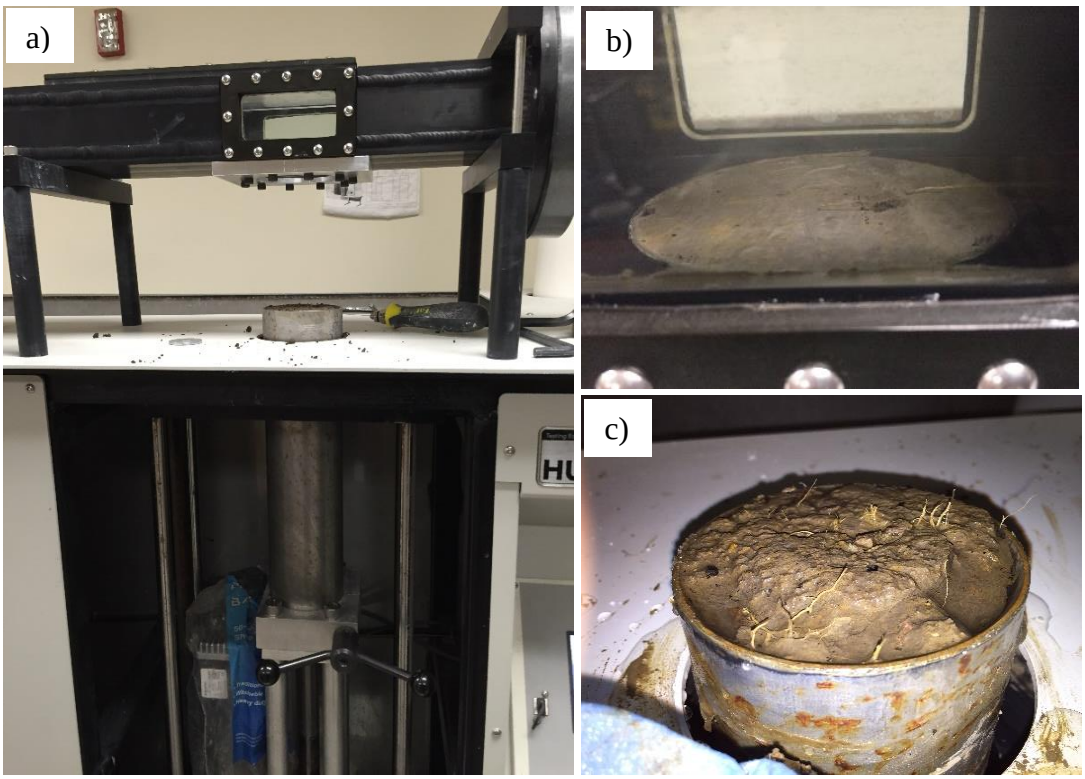

Fig. 3.5. a) Placement of the sample on piston head; b) trimmed sample in flush with flume bottom (before the test); c) sample with rough surface (after the test)

The above process was repeated for other velocities. Before starting the test under each velocities, the top of the sample was trimmed so that the soil sample was flush with the bottom of the flume. This allowed the flowing water to exert shear force on the soil surface tangentially.

3.4.2 Calculating Shear Stress

As mentioned in Chapter 2, in the equation for calculating shear stress τ (N/m^2) (Eq. 2.16), there is a term called friction factor f which is obtained from the Moody chart (Munson et al. 1990), shown in Fig. 3.6. The friction factor f is a function of pipe Reynolds number, and relative roughness. Reynold's number, R is calculated using

$$R = \frac{VD}{\upsilon} \tag{3.1}$$

where, V is the water velocity, D is the pipe diameter, υ is the kinematic viscosity of water (10^{-6} m^2/s at 20℃). Again, relative roughness is calculated from the ratio, ε/d; where, ε is the average height of roughness elements of the eroding surface of the sample, and d is diameter of the sample.

For the rectangular cross section of the flume, D is taken as the hydraulic diameter $D = 4A/P$; where, A is the cross-sectional area; P is the wetted perimeter; and 4 is a factor to convert the hydraulic diameter of the flume to the diameter of a circular pipe. Hence, for the rectangular cross section of the pipe (flume), D is calculated using the following equation:

$$D = \frac{2ab}{a+b} \tag{3.2}$$

where, a and b are side dimensions of the flume. The accuracy of the shear stress calculation depends on the accurate measurement of the relative roughness of the eroding surface. After testing under each velocities the plain eroding surface becomes irregular and rough (Fig. 3.5 (c)) because erosion does not occur homogeneously along the surface. For calculating the average height of the roughness elements ε, several measurements of the height of the individual roughness elements and their corresponding areas were taken so that:

$$\varepsilon = \sum_{i=1}^{n} \frac{h_i A_i}{A} \tag{3.3}$$

where, h_i, A_i are the height and corresponding area of i-th roughness element measured by calipers; n is the number of roughness elements; and A is the cross-sectional area of the sample.

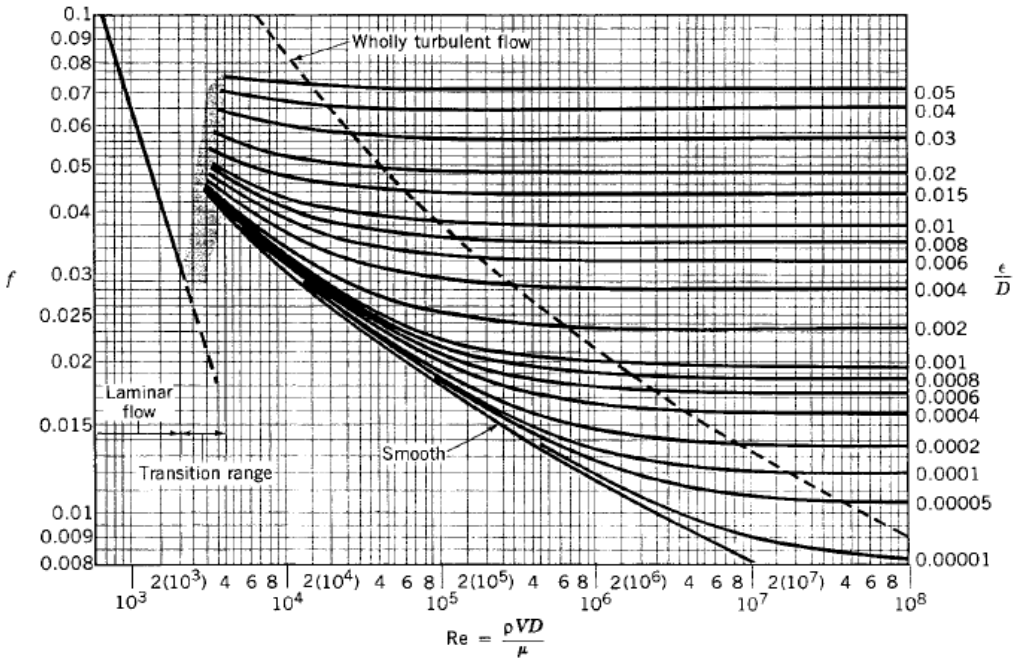

Fig. 3.6. Moody chart (Munson et al. 1990)

3.5 Soil Classification

The EFA test samples were classified using Unified Soil Classification System (USCS) (Coduto 1999). Almost all of our sites (10 out of 11 sites) having fine grained soils, Atterberg limit tests were required in addition to grain size distribution for classification.

ASTM standards C117 (ASTM 2013a) and C136 (ASTM 2014a) were followed for wet and dry sieving respectively; while ASTM D422 (ASTM 2007) was followed for the hydrometer analysis. The soil samples were dried in the oven at approximately 105-110℃ for 24 hours. The aggregation of the dried sample was broken by grinding it with a rubber covered pestle in a mortar. Approximately 500 g of each sample was used for sieve analysis. At first, the sample was washed through a #200 sieve. Then, the portion retained on #200 were left for drying in the oven at 105-110℃ for 24 hours; after drying this, they were dry sieved using the sieves recommended by ASTM standard C136. The hydrometer analysis was conducted using the sample passed through #200 sieve. The mass retained on each sieve and hydrometer data were used to prepare grain size distribution curve. Although not needed for classification according to the USCS, the hydrometer analysis was conducted to obtain median grain size, d_{50} that was used in the analysis. Atterberg limits tests were conducted according to ASTM standard D4318 (ASTM 2010b).

3.6 Electrical Resistivity Survey

Ideally, the goal was to conduct the ER survey on the same day as sample drilling to ensure the in situ water content would be the same as measured in the laboratory. As mentioned in Chapter 2, the ER of soil is primarily controlled by the water content. However, due to time constraints, three of the sites (US36, K-9, and K-126) were surveyed on a different date than the drilling date. But, using repeated measurements at US-36 the change in electrical resistivity over time was found negligible if drilling or ER surveys were not conducted immediately following a rain event (Valenzuela 2015).

ER data were collected using the 'SuperSting with Wi-Fi Eight-Channel Earth Resistivity, Induced Polarization and Self Potential Instrument for Geo-Electrical Tomography' (SuperSting) meter, manufactured by Advance Geosciences Inc. (AGI). Powered by two 12V deep-cycle marine batteries, the SuperSting can take up to eight simultaneous voltage readings per single current

injection, speeding up data acquisition. Each connecting cable has four electrodes on it and K-State has 14 cables allowing for 56 electrodes per survey. The electrodes were connected to metal stakes that were hammered into the ground to couple the electrodes to the subsurface. Metal stakes were 46 cm in length and 2.2 cm in diameter. The stakes were hammered as deep as possible into the ground to ensure contact for the injected current and measured voltage potential.

A command file was created in the computer and uploaded to the SuperSting prior to the ER survey. The command file provided all directions to the SuperSting regarding the sequence in which different electrodes should be used for current injection or measurement of voltage difference. AGI's SuperSting Administrator software was used to create the command file for this research. Information such as, type of array, number of electrodes, sequence and amount of ER data to be collected was given as input during preparing the command file. The anticipated depth of survey, data coverage and time estimation for the survey are estimated by simulating the command file in the same software. After creating the command file it was saved and transferred to the SuperSting.

Three criteria were considered when the array type was selected: vertical and lateral resolution, depth of investigation and test duration. As mentioned previously, that the total drilling length was approximately 3.1 m (10 ft) and the diameter of drilling was 88.9 mm (3.5 in). As such, the primary intention of the ER investigation was to achieve higher vertical resolution than lateral resolution around the borehole. The dipole-dipole array was selected because it provided highest vertical and lateral resolution simultaneously. Use of dipole-dipole array allowed to get the bore-hole ER as well the subsurface image of entire channel section with optimum resolution. The command file was created for the dipole-dipole array and loaded on the SuperSting before going to each site. Simulation of the command file showed that approximate depth of investigation was $10ES$ for the dipole-dipole array, where ES is the electrode spacing. Therefore, 0.46 m (1.5 ft) was chosen as the electrode spacing in the site, so the intended depth of 3.1 m (10 ft) was imaged with optimum resolution.

With 56 electrodes and a spacing of 0.46 m (1.5 ft), the length of survey line was 25.15 m (82.50 ft). The survey line was selected in such a way that the position of the borehole was in the center of the ER survey line (between the 28^{th} and 29^{th} electrode). This was also selected because, in the

ER survey, more data points are in the central region of the survey line and consequently the highest resolution is obtained in that region. A straight survey line was laid with the aid of a tape. Then, the stainless steel stakes were hammered into the ground at 0.46 m spacing. The stakes were driven as deep as possible to ensure adequate contact with the soil. The electrode portion of the cable were attached to the steel stakes and cables were connected to each other (Fig. 3.7 (a)). The cables adjacent to the 28th and 29th electrodes were connected to the SuperSting for data acquisition (Fig. 3.7 (b)). Finally the SuperSting was connected to the DC power supply. Two 12V DC batteries were used as power supply in this research.

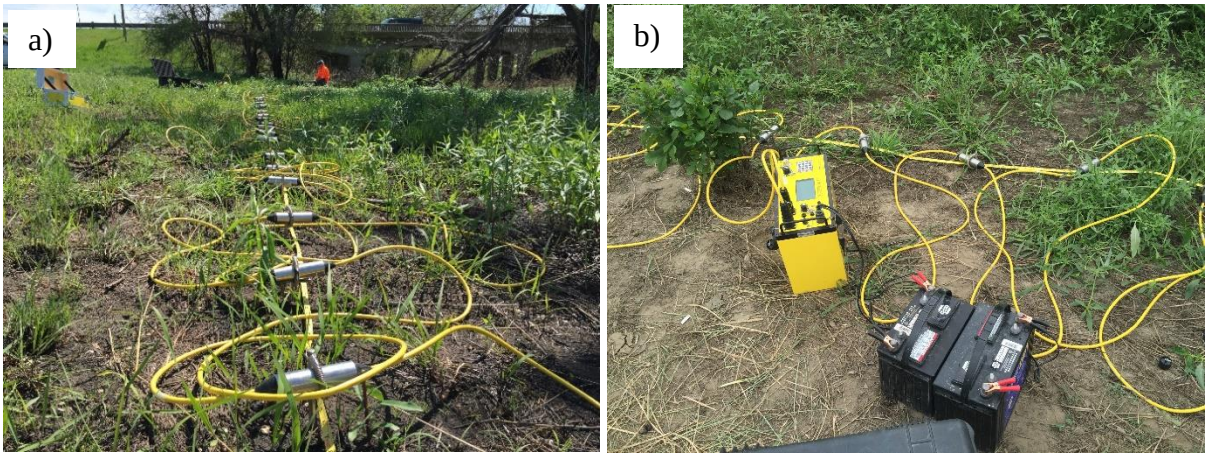

Fig. 3.7. a) ER survey line; b) 28th and 29th electrodes connected to the SuperSting

Once the setup was complete, the contact resistance test was performed before actual ER survey. A contact resistance test indicates if the surface area of the stakes is getting enough contact into the ground. Bad contact will increase the contact resistance. A higher value indicates that current is not flowing into the ground with ease, and this may produce noisy data. The contact resistance test also verifies that all cables are connected to each other and that the electrodes are attached to the steel stakes. If the LCD screen of the SuperSting shows an error "HVOVL", that indicates poor contact between the stake and the ground. Since most of the sites were of fine grained soils, contact with the ground was not an issue. The second error, "INOV" indicated that there was improper connection of the electrode cables. The values of contact resistances found in all sites were in the range of 0 to 500 Ω. Contact resistance values less than 40,000 Ω ensures good contact between electrode and ground, meaning the maximum electric current could be injected into the ground,

reducing noise in the survey. For coarse grained particles, however, contact resistance test can be significant where the values are in the range of tens of thousands.

The actual ER survey followed the contact resistance test. At the beginning of the actual ER survey, a file name was selected so that it could be recognized after the survey for analysis. Then, the command file was chosen that had been uploaded in the SuperSting. The ER survey was started after fixing the array type and spacing. In this research, the runtime of each ER survey using dipole-dipole array was around 32 minutes. This time was utilized for measuring the relative elevations of each electrodes using a total station and a survey rod. This information was required to produce the terrain file. The terrain file contains the relative horizontal and vertical coordinates of each electrode that are utilized for post processing of the ER survey data. For post processing, the file containing all the data of ER survey was downloaded using the SuperSting Administrator software. After downloading, two types of file were created: .crs file had the contact resistance data and .stg file had the measured resistivity data. These were saved for post processing.

3.6.1 Data Processing

AGI's EarthImager 2D was used for processing of measured ER data. Data processing, consisting of data inversion and forward modeling, is an iterative process to get inverted resistivity from the apparent resistivity measured in the field. The basics of these two process were discussed in section 2.2.6. After reading the field data, the first step was to check for noisy data and remove them (if required) before inversion process. Additionally, data removal criteria can be set to remove negative resistivity, set minimum voltage, or remove spikes so that noisy data has less impact in inversion process. The finite element method was chosen for forward modeling using Cholesky decomposing as the equation solver. In the boundaries of finite element mesh (surface, bottom and sides), Dirichlet boundary condition was applied to solve the unknowns of the associated equations. Once all the settings are set, the terrain files was read. Then the inversion and forward modeling processes are started that continues until the desired criteria are fulfilled and finally inverted resistivity section is obtained. However, if the RMS error is not satisfactory, poorly fit data can be removed from the data misfit scatter plot and a modified inverted resistivity section can be obtained.

3.7 Summary

This research include both field and laboratory procedures. Fieldwork included sample drilling and ER survey. Laboratory work included erosion testing in EFA, soil classification and analysis of the ER data. The major difficulties experienced to carry out the research project are described below.

One of the constraints in the fieldwork was to find adequate ground stretch of native soils for drilling and ER survey. Because, near bridge abutment and pavement the embankment soil may not represent the actual geology of the site. Again, due to the proximity to the stream and adjacent farmlands, it was difficult to obtain enough length for setting ER survey line. During drilling, sometimes, due to the lack of skin friction, the sample fell from the tube (K-9, K-126, US-400). In those cases, resampling was done and the corresponding depths were noted.

Chapter 4 - Results and Analysis

This chapter includes the results of the ER survey and erosion tests performed in the EFA. Erosion test results are presented as erosion rate with respect to shear stress applied by the flowing water. In the analysis section, soil erodibility levels are classified using several parameters including ER. Additionally, analytical development such as regression equations to predict critical shear stress are provided as functions of ER and other soil parameters.

4.1 Typical Results from a Single Site

ER surveys were conducted as close to the stream as possible depending on the site conditions for all 11 sites. Five 0.6 m long soil samples were collected at each site with a drill rig continuously pushing from the surface to 3.1 m using 88.9 mm diameter thin-walled Shelby tubes. In the laboratory, erosion tests were performed using each of these samples. Since five samples were collected from each site, a total of 55 samples were available for running erosion tests in the EFA. However, six of the Shelby tubes from different sites were bent during sampling and could not be used for erosion tests. And, one of the samples from K-9 site had 0.8 m recovery, which allowed for two erosion tests from a single sample. Ultimately, 50 samples were used for the erosion tests. After conducting erosion tests, the remaining soil of each sample was classified. Although all test results from 11 sites are used for analysis, only test results of K-58 site are shown below as a typical site.

4.1.1 Subsurface ER Distribution of K-58

K-58 site is located in Coffee County of eastern Kansas. The K-58 bridge crosses one of the Neosho river drainages; no water-flow was observed during the ER survey on October 22, 2015. The dipole-dipole array with 56 electrodes and 0.46 m center to center spacing was used, shown in Fig. 4.1. The inverted resistivity sections of the other sites are provided in appendix A.

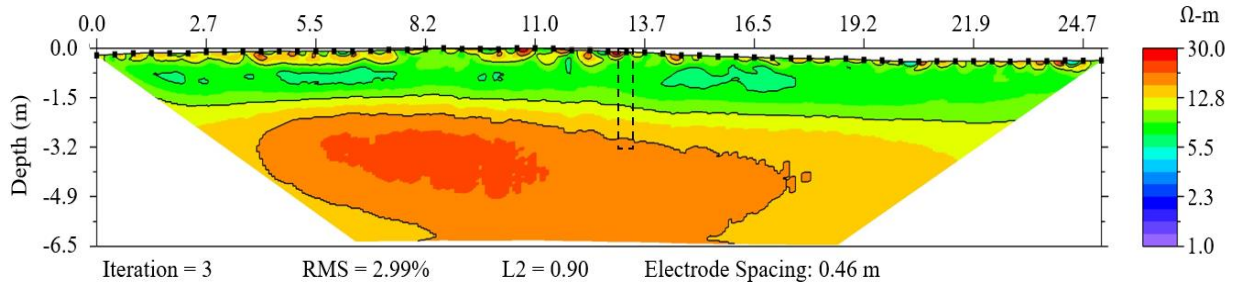

Fig. 4.1. Subsurface inverted ER distribution of K-58 site

The RMS error for the inversion was 2.99% and L2 norm was 0.90, which indicate good agreement of the measured and calculated resistivity. All inversion statistics had below 3.0 of RMS error and below 1.0 of L2 norm. These boundaries were set to for data quality specifications to ensure minimum error in the inversion process. The rectangle drawn with the dashed lines in Fig. 4.1 shows the location of borehole corresponding to the five samples from K-58. This two-dimensional distribution of ER is a contour diagram of ER constructed of thousands of elements in the subsurface. Each sample was 0.6 m long and 88.9 mm (0.1 m) in diameter. In the ER profile this 0.6 m x 0.1 m area corresponded to 16 elements of resistivity. The average ER from these 16 elements was used to calculate the ER of the sample. The ER's of the five samples from K-58 were between 8.7 to 18.5 Ω-m and are shown versus the mid-depth of the samples in Fig. 4.2.

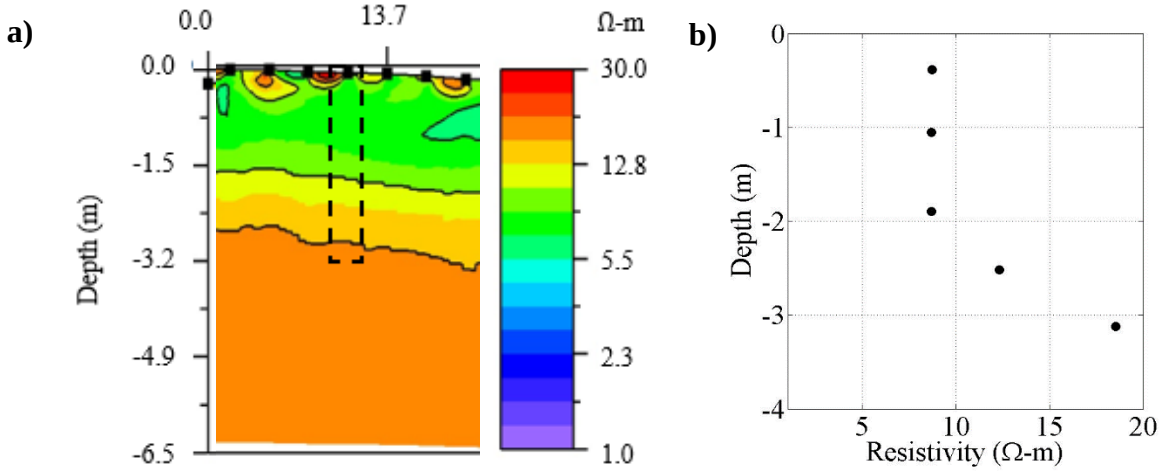

Fig. 4.2. a) Cropped ER distribution near sampling location of K-58 site, b) Plot of ER against the mid-depth for five samples

4.1.2 Erosion Test Results from K-58 Samples

Each erosion test was performed under six different water velocities and samples were allowed to erode for one hour under each velocity. Eq. 2.16 was used to convert the velocities to shear stresses responsible for erosion. Table 4.1 presents the results of erosion tests from K-58 samples.

Table 4.1. Erosion test results of K-58 samples

Sample	Erosion Test Results							Critical Shear Stress (N/m^2)
US-58 #1	Water Velocity (m/s)	1.0	2.0	3.0	3.5	4.0	-	16.3
	Shear Stress (N/m^2)	2.9	20.0	40.5	50.5	65.0	-	
	Erosion Rate (mm/hr)	0.0	1.8	9.3	10.8	12.9	-	
US-58 #2	Water Velocity (m/s)	1.0	2.0	3.0	4.0	5.0	6.0	46.3
	Shear Stress (N/m^2)	3.0	11.3	26.4	47.6	96.9	193.5	
	Erosion Rate (mm/hr)	0.0	0.0	0.0	0.5	16.0	135.0	
US-58 #3	Water Velocity (m/s)	1.0	2.0	3.0	4.0	5.0	6.0	21.2
	Shear Stress (N/m^2)	3.7	13.3	23.1	51.0	119.7	139.5	
	Erosion Rate (mm/hr)	0.0	0.0	0.5	7.5	19.0	29.0	
US-58 #4	Water Velocity (m/s)	1.0	2.0	3.0	4.0	5.0	6.0	40.8
	Shear Stress (N/m^2)	3.3	12.2	23.6	46.0	98.1	124.7	
	Erosion Rate (mm/hr)	0.0	0.0	0.0	0.5	1.0	3.0	
US-58 #5	Water Velocity (m/s)	1.0	2.0	3.0	4.0	5.0	6.0	30.6
	Shear Stress (N/m^2)	3.3	11.9	25.3	40.0	109.4	144.0	
	Erosion Rate (mm/hr)	0.0	0.0	0.0	0.5	2.0	5.5	

Table 4.1 shows that, sample #2 through #5 were tested under a maximum velocity of 6 m/s. However, sample #1 was comparatively more erodible, hence it was tested up to 4 m/s. The high erodibility of sample #4 is also evident by its lower critical shear stress (16.3 N/m^2). These results were compiled using HEC-18 (Arneson et al. 2012) erodibility categorizing plot in Fig. 4.3. Note that this a logarithmic plot. Points below critical shear stress have zero erosion rate and therefore are not visible in this plot.

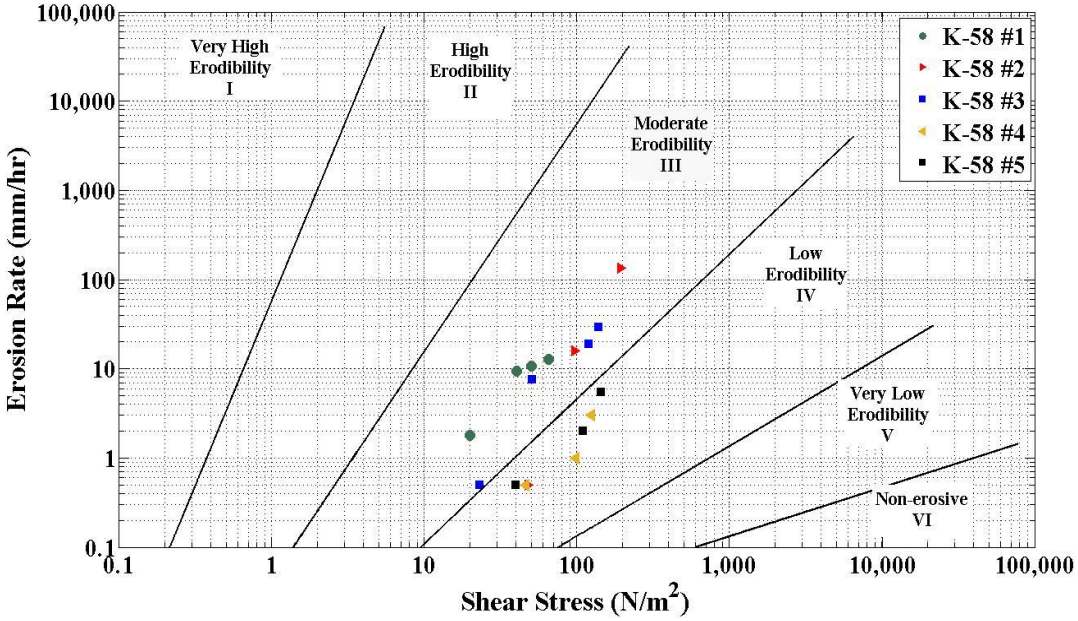

Fig. 4.3. Erosion rate versus shear stress for five samples of K-58

Fig. 4.3 shows that sample #1 was comparatively more erodible than the rest of the samples at the site. Note that all points from these samples were in the low to moderate erodibility zones according to HEC-18 erodibility categorization. Previously, Fig. 4.2 showed that corresponding ER values of these samples lie in the range of 8.7 to 18.5 Ω-m.

4.1.3. Soil Parameters and Classification of K-58 Samples

The remaining soils after erosion tests of each sample were used for soil classification and determining soil parameters. These parameters were used for predicting erosion characteristics discussed in sections 4.2 and 4.3. Table 4.2 shows the soil parameters and the USCS classification of the five samples from K-58.

Table 4.2. Soil parameters and classification of K-58 samples

Sample Designation	Water Content (%)	Percent Finer than 0.075 mm (%)	Median Grain Size (mm)	LL	PL	PI	USCS Classification
K-58 #1	33	99	0.0012	80	28	52	CH
K-58 #2	32	99	0.0014	72	22	50	CH
K-58 #3	26	99	0.0102	43	16	27	CL
K-58 #4	28	99	0.0070	44	14	30	CL
K-58 #5	30	98	0.0145	41	15	26	CL

Table 4.2 shows the water content (prior to erosion tests), w; percent finer than 0.075 mm, F; median grain size, d_{50}; liquid limit (LL); plastic limit (PL); plasticity index (PI) and USCS classifications of the five samples of K-58. The samples classified as low and high plasticity clays. The median grain size ranged between 0.0012 to 0.0145 mm and the plasticity indexes ranged between 26 to 52. These results were in agreement with their low ER values (8.7 to 18.5 Ω-m).

4.2 Analysis of the Erosion Characteristics Integrating All Sites

4.2.1 Erosion Performance for Various Sites

All of the sites in this study were distributed throughout eastern Kansas. As mentioned earlier, although 55 samples were collected from eleven sites (five from each), six of them were damaged and one extra sample was collected at a site. Results of erosion tests of 50 samples from the eleven sites are shown in Fig. 4.4.

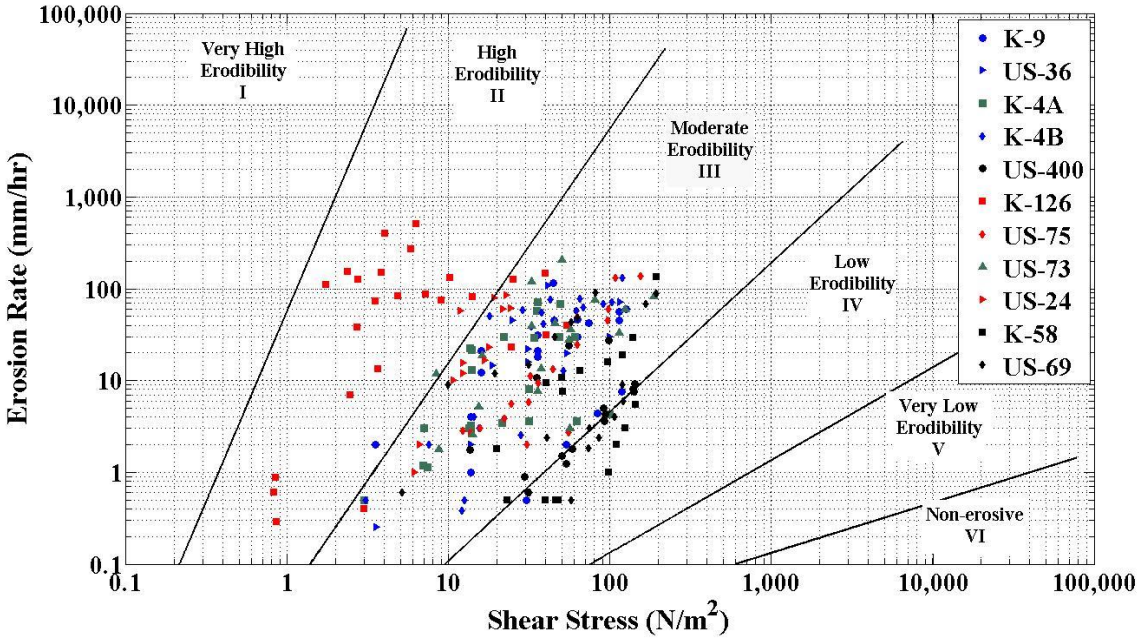

Fig. 4.4. Erosion rate versus shear stress for eleven sites

78.7% of soil samples used in this study were classified as moderate erodibility. Points falling in the low erodibility zones are mostly from US-58, US-69, and US-400. K-126 samples alone contributed to the most of the points falling in the high erodibility zone. The lowest erodibility sites (US-58, US-69, and US-400) and the highest erodibility site (K-126) were all in southeast

Kansas. K-126 site may be given priority in any further bridge-scour monitoring by KDOT because it was highly erodible compared to the other sites.

4.2.2 Effects of Index Properties on Erosion Performance

The plasticity indexes of all the samples were divided into five categories and plotted on the erodibility graph as shown in Fig. 4.5. A total of 22 points fell in the high erodibility zone; of them, 19 points had plasticity indexes below 10. Again, among the points falling in the moderate erodibility zone, those having PI of 10 to 19 (shown with green dots) were more erosive (since, closer to moderate-high erodibility boundary) than the other points corresponding to comparatively higher plasticity indexes. Bernhardt et al. (2011) also performed a similar analysis using plasticity indexes of the Mississippi river levee soils.

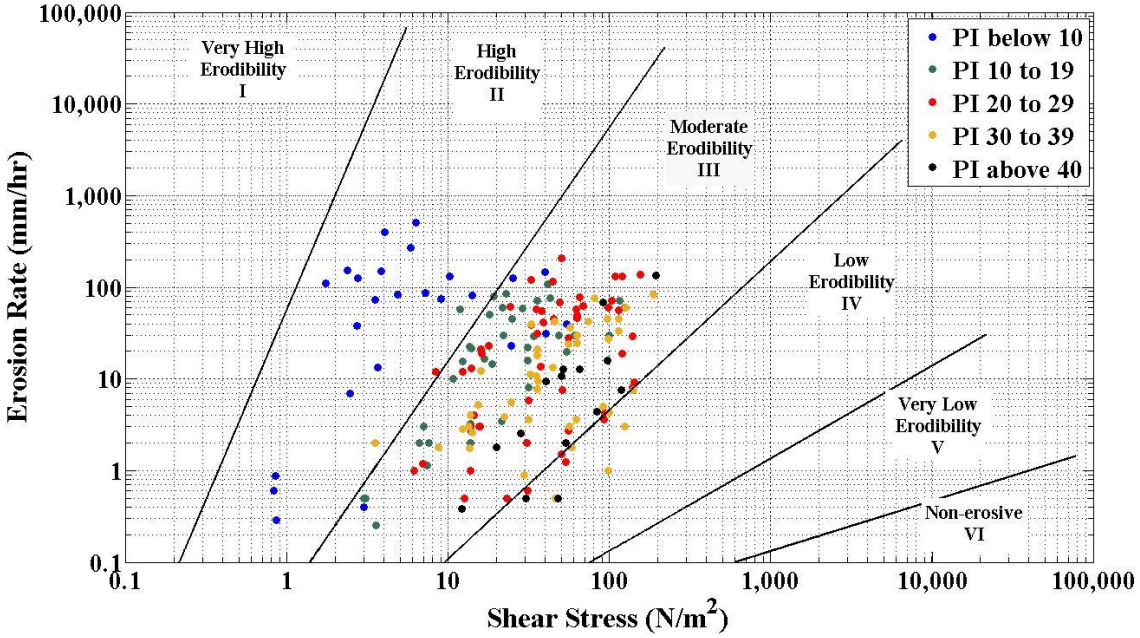

Fig. 4.5. Erosion rate versus shear stress for varying plasticity index

4.2.3 Effects of Particle Sizes on Erosion Performance

Median grain size was calculated from each sample using the grain size distribution curve. Note that the samples from the first three sites of this project (K-9, US-36, and K-4B) were not sieved using the wet sieve method. The values of percent finer than #200 sieve were in the range of 50 to 60 % for the samples from these three sites (using dry sieving only). Index properties of these

samples, determined later, were not in agreement with the previously obtained median grain sizes. As the samples were discarded after sieving, corrections could not be made to the median grain sizes of the samples from these three sites and will not be used in analysis. Samples from rest eight sites were sieved using both dry and wet sieving method and accurate median grain sizes were obtained. Among the rest eight sites used in the analysis, only K-126 had coarse gained samples, with particles up to 1.9200 mm. The median grain sizes of the remaining sites' samples were between 0.0012 mm (K-58 #1) and 0.0310 mm (US-69 #1). The median grain sizes of the eight sites were divided into four categories to analyze the effect of grain size on erosion performance shown in Fig. 4.6.

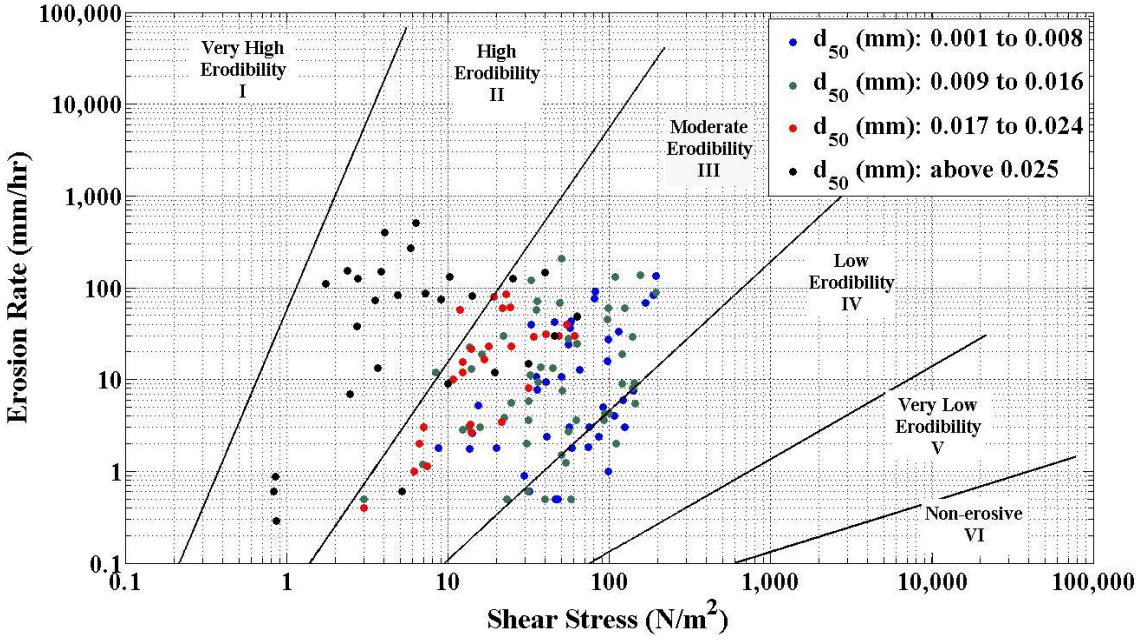

Fig. 4.6. Erosion rate versus shear stress for varying median grain size

As evident from Fig. 4.6, particles with larger median grain size were more erodible. Most of the points (19 out of 21) that showed high erodibility, had median grain size above 0.025 mm. Moreover, the higher density of red dots near the moderate-high erodibility boundary indicates that the samples corresponding to median grain size of 0.017 to 0.024 mm were more erodible than the smaller particles.

4.2.4 Erosion Performance for Varying Soil Types

Erodibility categorizing graph was also utilized in terms of the USCS soil types of the samples. Soil classification gave six different types of soils for the samples collected from eleven sites. The results of the erosion tests with varying soil type is presented in Fig. 4.7.

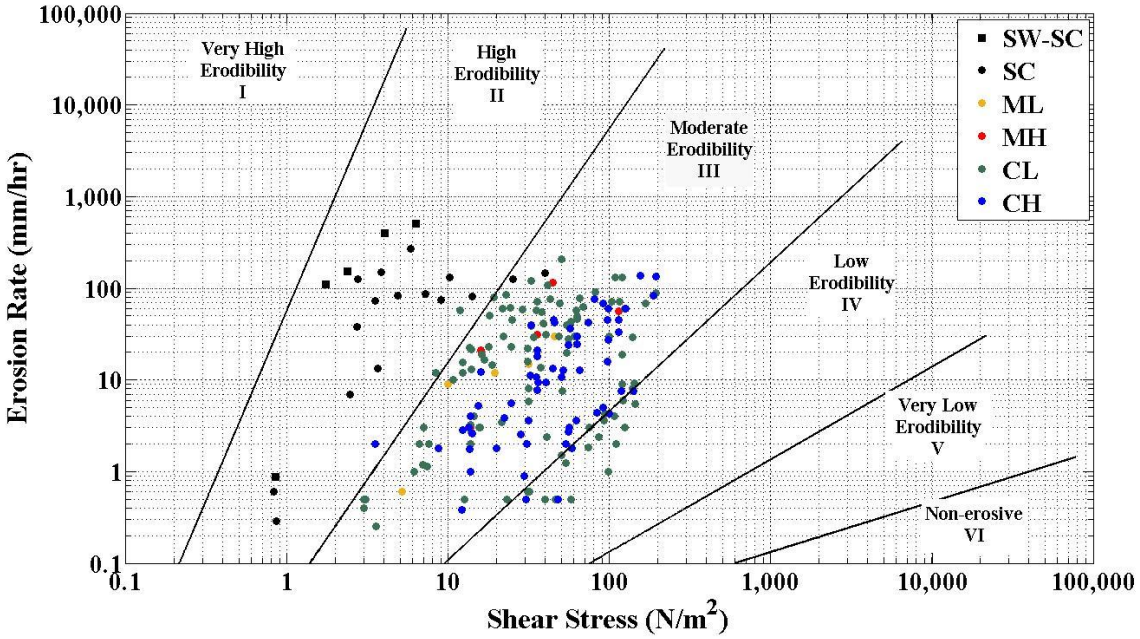

Fig. 4.7. Erosion rate versus shear stress for varying soil type

It is evident from Fig. 4.7 that soils classified as sand (SW-SC and SC) have mainly contributed to the points showing high erodibility. Two samples of K-9 were classified as highly plastic silts (MH) and one sample from US-69 was classified as low plastic silts (ML); all of these showed moderate erodibility (represented by the red and yellow dots). The remaining samples were classified either as low or high plastic clays (CL or CH respectively) and were moderate and low erodibility. It can be seen that the density of the green dots (representing the CL) is more in the moderate-high erodibility boundary. This may indicate that CL samples were more erodible than CH samples (blue dots). Briaud et al. (2011) included the corresponding soil types into the erodibility categorizing graph based on their previous erosion test results in EFA as shown in Fig. 4.8. If results of this project are compared with this figure, it shows very good agreement.

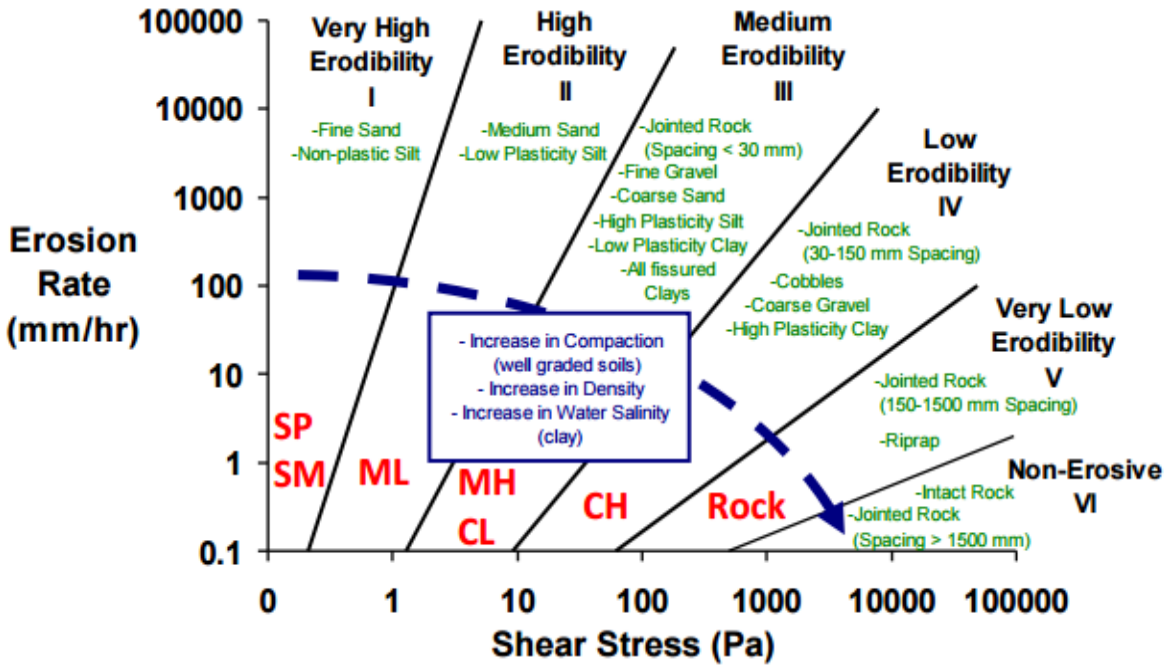

Fig. 4.8. Erodibility categories of different soil types based on shear stress (Briaud et al. 2011)

4.2.5 Erosion Performance for Varying ER

Soil parameters such as median grain size, plasticity index, percent of fines, water content have been used to trace the erosion before by many researchers such as Hanson and Tremble (2002), Clark and Wynn (2007). However, no evidence of using geo-physical methods such as ER to describe soil erosion is found in literature. In this project, ER values of different samples varied from 6 Ω-m (K-9 #4, US-73 #1) to 328 Ω-m (K-126 #2). Erosion rate versus shear stress for varying ER is shown in Fig. 4.9.

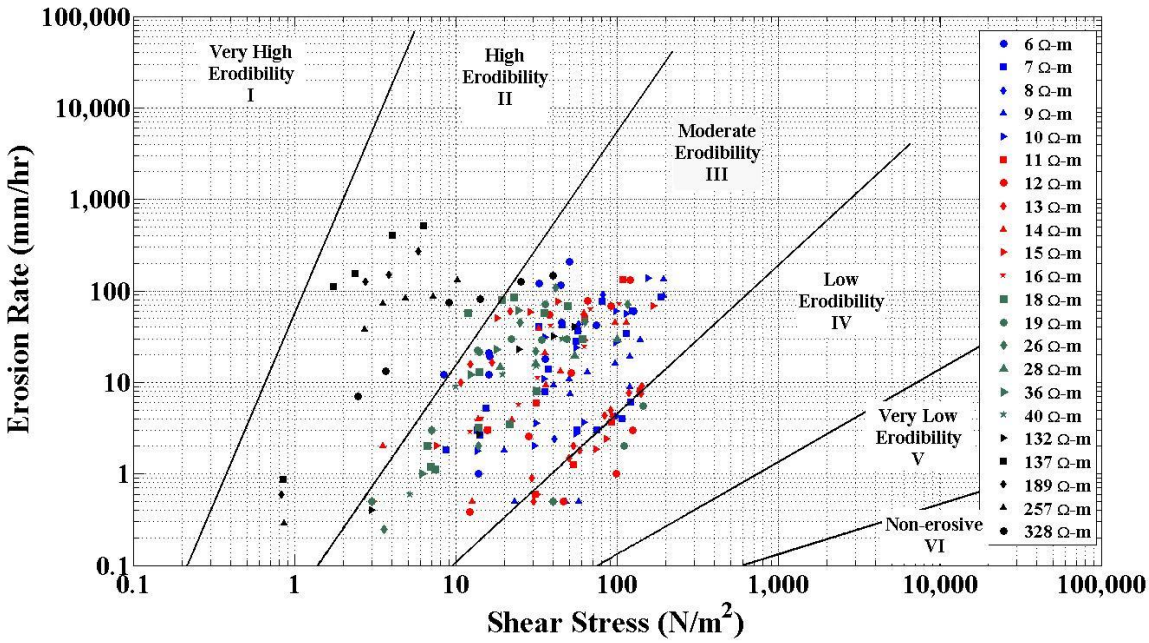

Fig. 4.9. Erosion rate versus shear stress for varying ER

Fig. 4.9 was constructed for the ER of each sample. There were 22 different measured ER's (after rounded to nearest full number) from the 50 samples. Note that 13, out the 22 ER values corresponded to more than one sample. A trend showing samples with higher ER values tended to be in the high erodibility category as shown in Fig. 4.9. As such, ER values were divided in two ranges; below and above 100 Ω-m as shown in Fig. 4.10 to improve the visualization of the effect of ER on erosion.

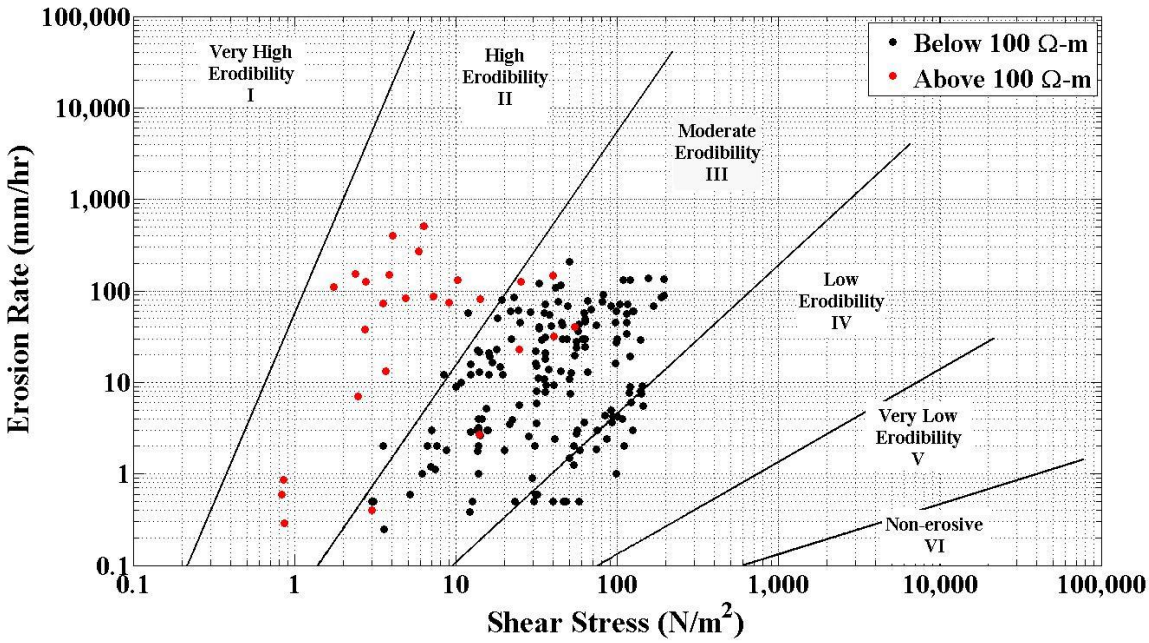

Fig. 4.10. Erosion rate versus shear stress for two ranges of ER

In this study, 171 out of 197 of the points in the erodibility graph corresponded to ER of less than 100 Ω-m. When ER values were below 100 Ω-m, 98.3% (168 out of 171) points showed low to moderate erodibility. Again, when ER values were above 100 Ω-m, 73.1% (19 out of 23) points showed high erodibility. Fig. 4.10 shows that ER survey can be used as a preliminary tool to prioritize scour critical bridges and eliminate time consuming erosion tests. In fact, only one site from this study, K-126, provided samples that had ER values over 100 Ω-m. Most of the samples from this site, although classified as sands, contained both fines and gravel. Visually it looked like a fine-grained soil but the ER survey identified the presence of gravel (as ER was more than 100 Ω-m) entrapped within the fines in the subsurface and later it showed high erodibility when tested. This highlights how ER can be used to predict the erodibility.

4.3 Predicting Critical Erosion

All 50 samples from 11 sites showed various erosion patterns. The majority of the samples started eroding in small particles at lower velocity (and corresponding shear stress) and as velocity was increased they eroded in soil blocks. When big blocks of soils erode, holes are created on the eroding surface and water entrapped in these holes provides turbulent forces on the samples. These turbulent forces are a higher magnitude than the eroding forces. Although, block by block erosion

cannot be totally ignored, tests were restarted after trimming the samples when turbulence was observed on the eroding surface. For this reason, testing at very high velocity (above 4 m/s) was not possible for these kind of soils. Again, Samples #2 through #5 from K-126 and #1 from US-69 had considerable amount of gravels and very low plasticity indexes, thereby did erode in blocks, but were very erodible. These samples started to erode at very low velocities (such as 0.3 m/s) and all soils finished eroding at very low maximum velocity (below 3 m/s). Furthermore, some samples (such as from K-58) with very high plasticity indices did not show any erosion by blocks and the erosion rate was very low (less than 10 mm/hr) at water velocity as high as 6 m/s. Although all the tests were velocity controlled, corresponding shear stress will be used for any analytical development. It is the shear stress exerted by the water on soil surface that actually causes the erosion. Different samples tested under the same velocity have different shear stress depending on the roughness of the erosion surface. For these reasons, shear stress is used in the analysis. The relation between erosion rate and shear stress as shown in Fig. 4.3 through Fig. 4.10 can take various shapes when plotted. For describing this relation, critical shear stress is an important curve fitting parameter. As such, a model that can predict the critical shear stress is needed for future applications of this methodology.

4.3.1 Predicting Critical Shear Stress Using ER

It was shown that ER may be used as a rapid tool for determining whether a bridge-site is vulnerable by using the HEC-18 erodibility categorizing graph to evaluate erosion potential. For analytical development, critical shear stresses, of the 50 samples were plotted against the corresponding in-situ ER. When data were plotted, critical shear stress did not appear to vary linearly with ER and linear relationship provided $R^2 = 0.13$ only. Various mathematical functions such as exponential, logarithmic, power, and polynomial relationship between the independent and dependent variables were iterated. Ultimately a power relationship provided the best fit to the data with $R^2 = 0.59$, and therefore, was selected. The relationship is presented in logarithmic scale in Fig. 4.11.

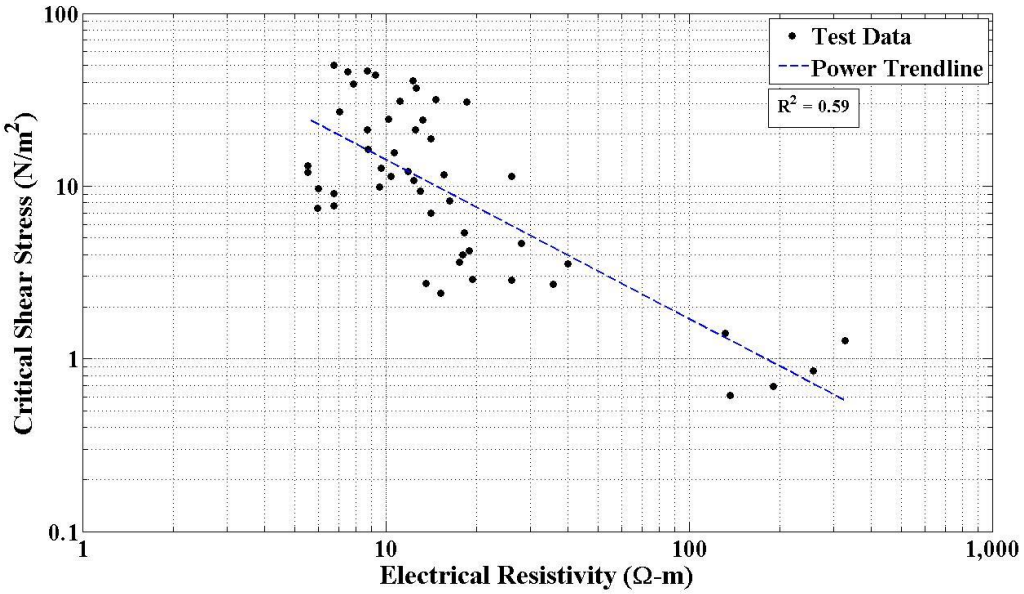

Fig. 4.11. Critical shear stress versus electrical resistivity (ER)

As seen from Fig. 4.11, critical shear stress decreases with increasing ER. The regression was performed in SAS^{TM} software (SAS Institute Inc. 2014) and the equation to predict critical shear stress, τ_c using ER is given as:

$$\tau_c = 118.62\ \rho^{-0.92} \tag{4.1}$$

where, ρ is the ER of soil. Note that, the residual (difference between actual and predicted shear stress) output showed that the values of 27 observations (out of 50 observations) of τ_c are over predicted. As such, the slope coefficient (118.62) of eq. 4.1 needs to be modified using an appropriate factor of safety if used in design. Prior to this study, no evidence of predicting critical shear stress using ER was found in the literature. Although examples of predicting critical shear stress using other soil parameters can be found in the literature, the R^2 were very low and the datasets were small for these experiments. An R^2 of 0.59 for 50 data sets shows that ER alone may be used to predict the critical shear stress.

4.3.2 Predicting Critical Shear Stress Using Median Grain Size

One advantage of this project was, although soil samples were predominantly fine grained, a wide range of grain sizes were observed. This helped to obtain a relationship between critical shear

stress and median grain size. Similar studies to correlate critical shear stress with median grain size were done previously by researchers. These attempts did not find any good correlation among these two parameters; for example, Kimiaghalam et al. (2016) obtained R^2 = 0.11 when critical shear stresses were plotted against median grain sizes of 17 fine grained samples in a linear scale. In this project, a linear relationship provided R^2 = 0.12. Several other models were investigated (such as exponential, logarithmic, and polynomial); but power model provided the best fit among the data and R^2 was found 0.60. The relationship is shown in Fig. 4.12.

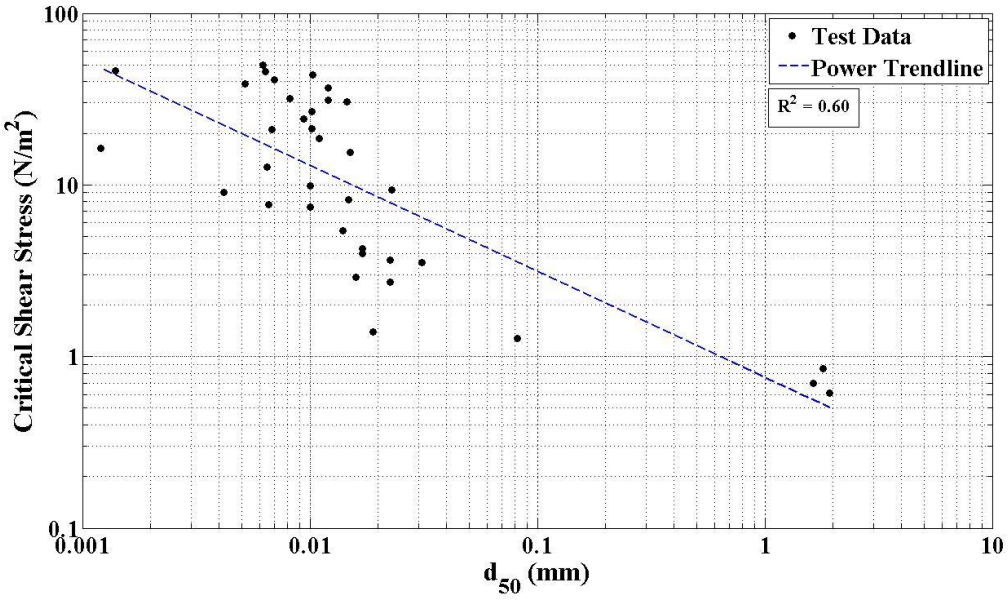

Fig. 4.12. Critical shear stress versus median grain size

Fig. 4.12 shows that critical shear stress for erosion decreases with increasing median grain size. The predictive equation from this power model is expressed as follows.

$$\tau_c = 0.76\, d_{50}^{-0.62} \tag{4.2}$$

where, d_{50} is median grain size. Note that this correlation does not include the median grain sizes of the samples from first three sites (K-9, US-36, and K-4B); so there were total 36 observations from remaining eight sites used in the regression.

4.3.3 Predicting Critical Shear Stress Using Plasticity Index

Previously researchers have tried to correlate critical shear stress using plasticity index. Moreover, Fig. 4.5 showed that plasticity index can categorize the erodibility. For this reason, critical shear stress was correlated with plasticity index. Kimiaghalam et al. (2016) used 17 fine grained soil samples for predicting critical shear stress using plasticity index and obtained linear upward (critical shear stress increases with increasing plasticity index) trend with $R^2 = 0.20$. Interestingly, on the contrary, Briaud et al. (2001) obtained a linear downward trend with a R^2 as low as 0.01 for 11 fine grained soil samples.

In this project, when critical shear stresses were plotted against the corresponding plasticity indexes from 50 samples in a linear scale, a R^2 of 0.20 was obtained. Like previous equations, several other models were investigated (such as exponential, logarithmic, polynomial, and power). The power model gave the best fit to the dataset and R^2 increased to 0.47. The relationship is shown in Fig. 4.13.

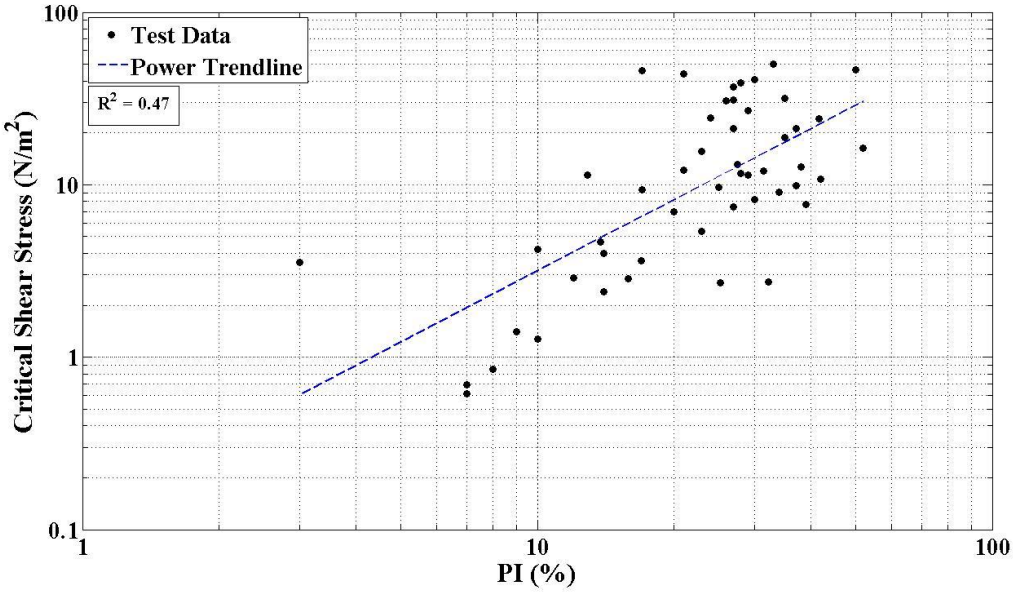

Fig. 4.13. Critical shear stress versus plasticity index (PI)

Fig. 4.13 shows that critical shear stress increases with increasing plasticity index. The equation to predict critical shear stress, τ_c using plasticity index is as follows:

$$\tau_c = 0.13\ PI^{1.37} \quad (4.3)$$

where, PI is the plasticity index. Total 50 observations were used in the regression. There are a few outliers in this correlation; for example, one of the US-69 sample (#1) (classified as ML) provided a plasticity index of three.

4.3.4 Predicting Critical Shear Stress Using Percent Finer and Water Content

Among the other soil parameters percent finer than 0.075 mm and water content were obtained and may influence critical shear stress as discussed in the literature review. In case of water content, no viable relationship was obtained with critical shear stress as the standard deviation in water content among the 50 samples was only 4%. Various models such as exponential, logarithmic, power, and polynomials were iterated, but no models gave a R^2 value above 0.2. This was also investigated by previous researchers who measured the effect of water content on the initiation of erosion (or critical shear stress); however, no good correlation has been found to date. For example, Kimiaghalam et al. (2016) obtained a R^2 = 0.05 when critical shear stresses were plotted against water content linearly.

Similarly, the effect of the percent of soil particles finer than 0.075 mm (passing ASTM standard #200 sieve) on critical shear stress was investigated. Although, a power model of critical shear stress versus percent finer had an R^2 of 0.49, the presence of non-constant variance was identified. The residuals (difference between actual and predicted value of critical shear stress) were very high when percent finer was above 95% compared to the coarser particles. As such, this parameter was not used in the analysis for predicting critical shear stress.

4.4 Variable Screening and Model Building

The previous sections showed the influence of ER, median grain size, and plasticity index on critical shear stress. Previous researchers have not correlated ER with critical shear stress. Several researchers have established that median grain size (Briaud et al. 2011, Smerdon et al. 1961) and plasticity index (Shan et al. 2015, Smerdon et al. 1961) are correlated with critical shear stress. As such, the objective was to combine ER with median grain size and plasticity index to determine if the resulting model predicting critical shear stress would be more accurate. This was done through a robust statistical analysis of the data. There are several model selection criteria in statistics; such

as coefficient of determination (R^2), adjusted coefficient of determination (R^2_{adj}), Mallow's C_p, and Akaike's Information Criteria (AIC). One of the important conditions to use these analyses is to have at least ten observations for each independent variable. As mentioned before, among the 50 samples of known ER and PI, there were 36 known data points for median grain size. The results of these analyses as obtained from SAS software are presented in Table 4.3.

Table 4.3. Variable screening results output from SAS software

Model #	No. of Variables	R^2_{adj}	R^2	C_p	AIC	Model Variables
Model #1	3	0.6916	0.7180	4.0000	-79.7143	log (ρ), log (d_{50}), log (PI)
Model #2	2	0.6089	0.6229	3.0000	-112.3879	log (ρ), log (PI)
Model #3	2	0.6858	0.7038	3.6138	-79.9431	log (ρ), log (d_{50})
Model #4	2	0.6272	0.6485	9.8902	-73.7800	log (d_{50}), log (PI)
Model #5	1	0.5786	0.5872	5.4471	-109.8676	log (ρ)
Model #6	1	0.5858	0.5977	13.6580	-70.9183	log (d_{50})
Model #7	1	0.4605	0.4715	19.8725	-97.5093	log (PI)

Table 4.3 shows the values of coefficients for four different model selection criteria: R^2_{adj}, R^2, C_p, and AIC. Mendenhall et al. (2012) provides a detailed derivation of these coefficients. There were seven models possible with various combinations of the independent variables. Note that variables were in logarithmic scales as all the models were power models. The criterion for the coefficients R^2_{adj}, and R^2 was, among the competing models, whichever had the highest value. Therefore, Model #1 was selected using criteria for R^2_{adj}, and R^2. The criterion for C_p and AIC was the model corresponding to the lowest value therefore Model #2 was selected for these two methods. The governing coefficient value among the seven different models for each model selection criteria are highlighted green in Table 4.3.

No criteria were satisfied for Model #3 through Model #7; hence these were discarded from further consideration. To select the best model for predicting critical shear stress Model #1 was compared to Model #2. The variables for Model#1 were log(ρ), log(d_{50}), log(PI); and the variables for Model #2 were log(ρ), log(PI). Comparing the two models, Model #1 had median grain size in addition to Model #2's variables. The calculation of plasticity index is dependent on determining the Liquid

Limit (LL) and Plastic Limit (PL) of the respective soil sample. Determination of LL and PL are user dependent, which may result in error. The median grain size is a unique soil property that does not require any visual judgement and is less operator dependent. Both models had plasticity index as a variable, but the contribution of plasticity index was less in Model #1. For this reason, with the presence of median grain size, Model #1 ($R^2 = 0.72$) was more robust and selected as the final model. The model parameters were obtained after regression analysis and the model equation was

$$\log \tau_c = 0.9356 - 0.6102 \log \rho - 0.1709 \log d_{50} + 0.3812 \log PI \tag{4.4}$$

where, ρ is the ER, d_{50} is the median grain size, and PI is the plasticity index. When eq. 4.4 was solved for critical shear stress, τ_c, the final model equation was

$$\tau_c = 8.62\, \rho^{-0.61}\, d_{50}^{-0.17} PI^{0.38} \tag{4.5}$$

where, all variables have been defined. The developed model for predicting critical shear stress in eq. 4.5, must be validated using additional data. Ultimately the factor 8.62 in eq. 4.5 may require modification using a factor of safety so it may be used as a design model that is safe as well as economically feasible.

4.5 Model Evaluation

As shown in Table 4.3 seven different models were possible with combination of the three variables namely, ER, d_{50}, and PI. On the basis of four variable screening criteria, Model #1 was chosen as the best model. Predicted values of critical shear stress using Model #1 were evaluated with respect to the measured values in the following section. Similar evaluations were also done for other models of the study. In addition to these models, two other models from literature, one from Briaud et al. (2011), and another model from Shan et al. (2015) will also be used to compare with the models developed in this research.

4.5.1 Evaluating Model #1 through Model #7

First, model #1 was used to calculate the predicted critical shear stress and compared with the measured (actual) critical shear stress, shown in Fig. 4.14. The governing equation for Model #1 was given in eq. 4.5. As mentioned before, 36 observations were used for the regression and R^2

was 0.72. Fig. 4.14 shows the model equation over-predicted 17 of the total 36 observations of critical shear stresses. It is also evident that the under-prediction is commonly done when the actual critical shear stress is above 16 N/m^2.

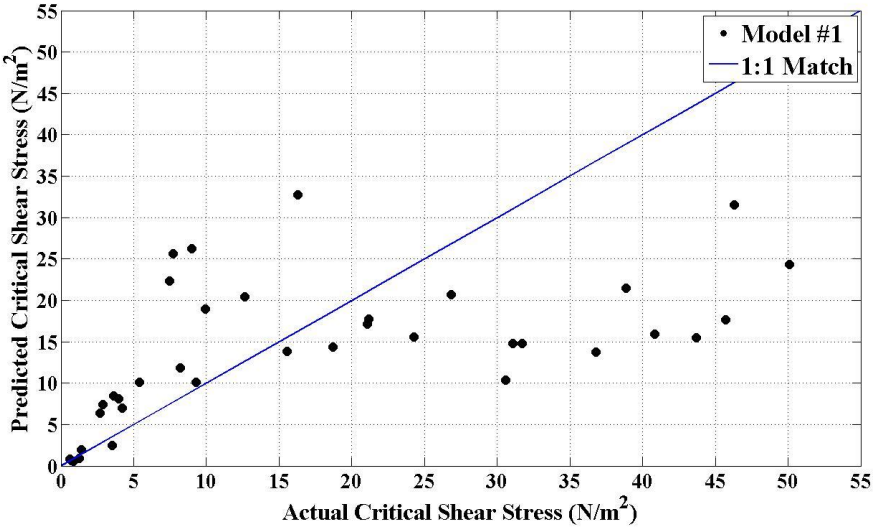

Fig. 4.14. Critical shear stress comparison (predicted vs. actual) for Model #1

For model #2, critical shear stresses, τ_c were predicted with the following equation

$$\tau_c = 11.20\ \rho^{-0.68}\ PI^{0.55} \tag{4.6}$$

where, ρ is the ER and PI is the plasticity index of the soil. A total of 50 observations were used in the regression and R^2 was 0.62. The model equation over predicted 25 out of the 50 observations and the predicted versus actual critical shear stress comparison is presented in Fig. 4.15 for Model #2.

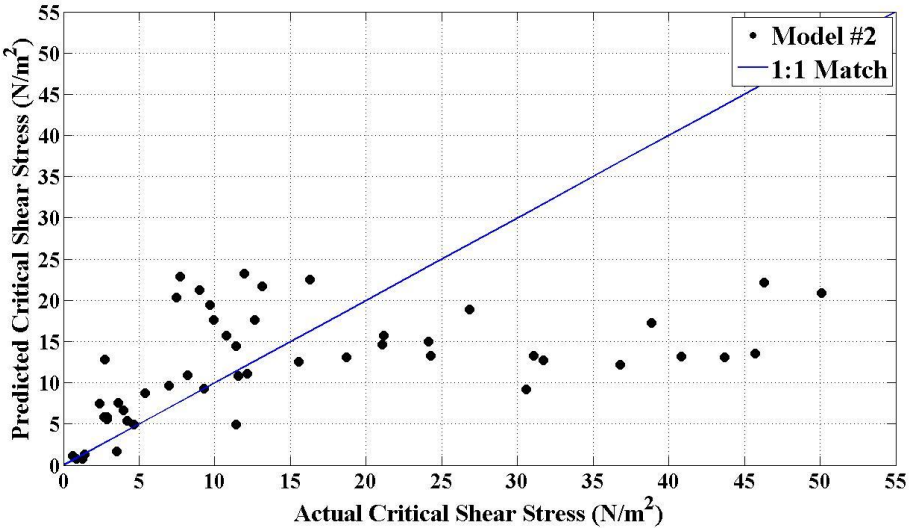

Fig. 4.15. Critical shear stress comparison (predicted vs. actual) for Model #2

Model #3 uses the following equation to predict critical shear stress, τ_c

$$\tau_c = 28.74\,\rho^{-0.71}\,d_{50}^{-0.23} \tag{4.7}$$

where, ρ is the ER and d_{50} is the median grain size of the soil. A total of 36 observations were used in the regression and R^2 was 0.70. Model #3 over predicted 17 out of 36 observations and the predicted versus actual critical shear stress comparison is presented in Fig. 4.16 for Model #3.

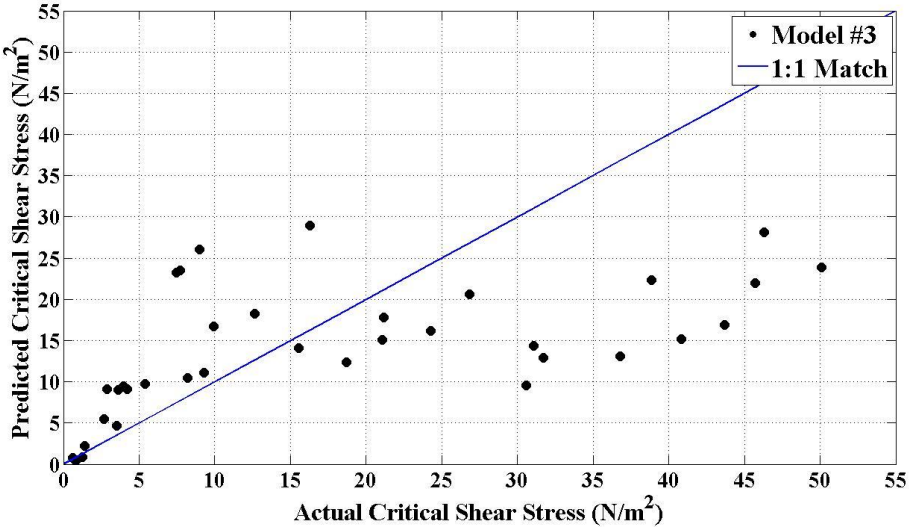

Fig. 4.16. Critical shear stress comparison (predicted vs. actual) for Model #3

For model #4, critical shear stresses, τ_c were predicted with the following equation

$$\tau_c = 0.22\, d_{50}^{-0.42} PI^{0.68} \tag{4.8}$$

where, d_{50} is the median grain size and PI is the plasticity index of the soil. 36 observations were used in the regression and R^2 was 0.65. The model equation over predicted 17, out of the 36 observations and the predicted versus actual critical shear stress comparison is presented in Fig. 4.17 for Model #4.

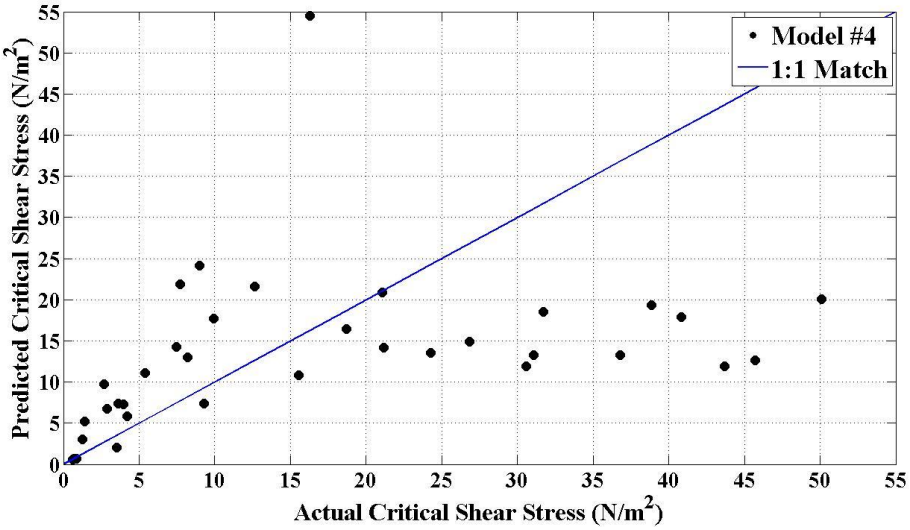

Fig. 4.17. Critical shear stress comparison (predicted vs. actual) for Model #4

Model #5 through Model #7 used only one independent variable each. Predicting critical shear stress using these models were previously discussed when single variable effects were considered in sections 4.3.1 through 4.3.3 of this chapter. In this section these models will be used for comparing the predicted values with the actual values.

Model #5 used ER (ρ) as independent variable and eq. 4.1 gives the governing equation. The regression used 50 observations and resulting R^2 was 0.59. 27, out of 50 observations were over-predicted as seen from the predicted versus actual critical shear stress diagram in Fig. 4.18.

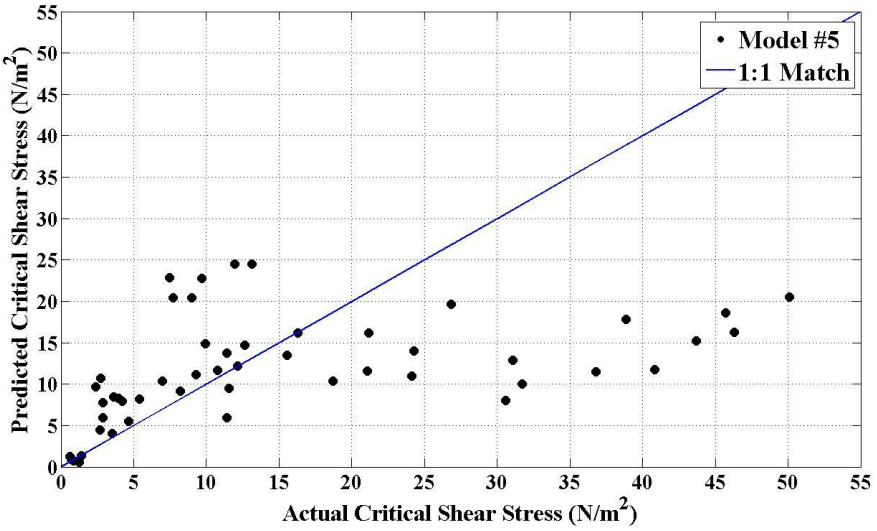

Fig. 4.18. Critical shear stress comparison (predicted vs. actual) for Model #5

Model #6 used median grain size, d_{50} as independent variable and governing equation to predict critical shear stress is given in eq. 4.2. 36 observations were used in the regression and R^2 of the model equation was 0.60. Fig. 4.19 shows the comparison of predicted value of critical shear stress with respect to actual measurement. 16, out of 36 observations shows over prediction. Only one extreme outliers can also be seen from Fig. 4.19 corresponding to 16.5 N/m^2 actual critical shear stress.

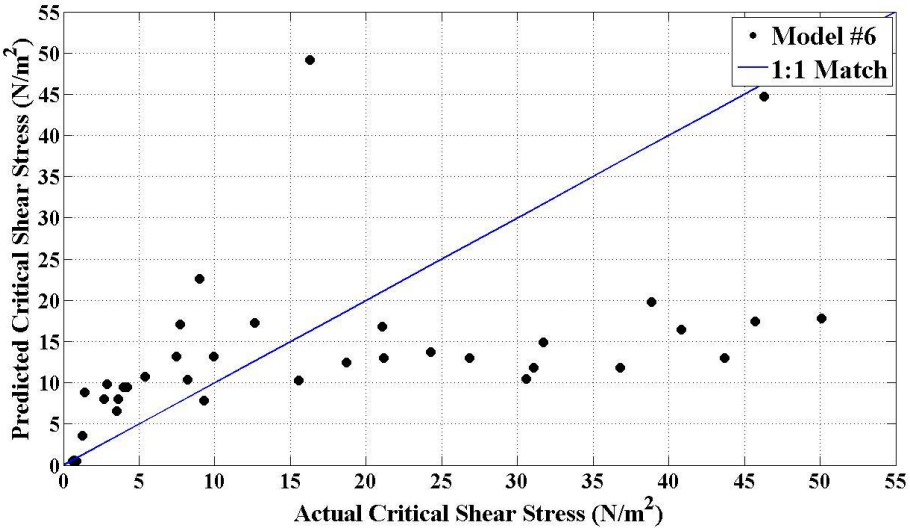

Fig. 4.19. Critical shear stress comparison (predicted vs. actual) for Model #6

Model #7 used only plasticity index of soil, *PI* as independent variable and eq. 4.3 gives the governing equation. The regression used 50 observations and resulting R^2 was 0.47. Out of 50 observations, 26 were over-predicted as seen from the predicted versus actual critical shear stress diagram in Fig. 4.20.

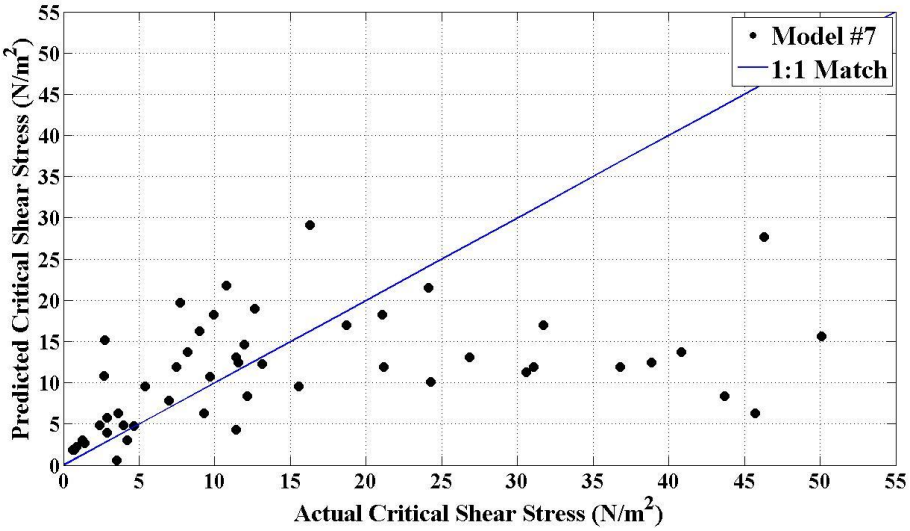

Fig. 4.20. Critical shear stress comparison (predicted vs. actual) for Model #7

4.5.2 Comparing Briaud et al. (2011) Model

HEC-18 provides two models, developed by Briaud et al. (2011) that use median grain size as an input variable to predict lower and upper bounds for critical shear stress. Note that, a similar type of approach to predict critical shear stress using median grain size was made in this project too, as shown in eqn. 4.2. The difference is, direct prediction was made in this research. Briaud et al. (2011) made a zone of predicted shear stresses applying lower and upper boundaries using median grain size. The equations for the boundaries for predicting critical shear stress are:

$$\tau_c = \alpha d_{50}^{-0.4} \quad (4.5)$$

$$\tau_c = \alpha d_{50}^{-2.0} \quad (4.6)$$

where eqn. (4.5) and eqn. (4.6) represent the lower and upper boundaries and the values of α (S.I. units) are 0.05 and 0.006 respectively (Briaud et al. 2011). These equations were utilized to predict critical shear stress boundaries for corresponding median grain size and compared with actual critical shear stresses obtained during tests as shown in Fig. 4.21. Note that these boundary

equations are valid for d_{50} less than 0.2 mm. 3 of the median grain sizes (out of 36 observations) were above this limit, and thereby not used in the comparison.

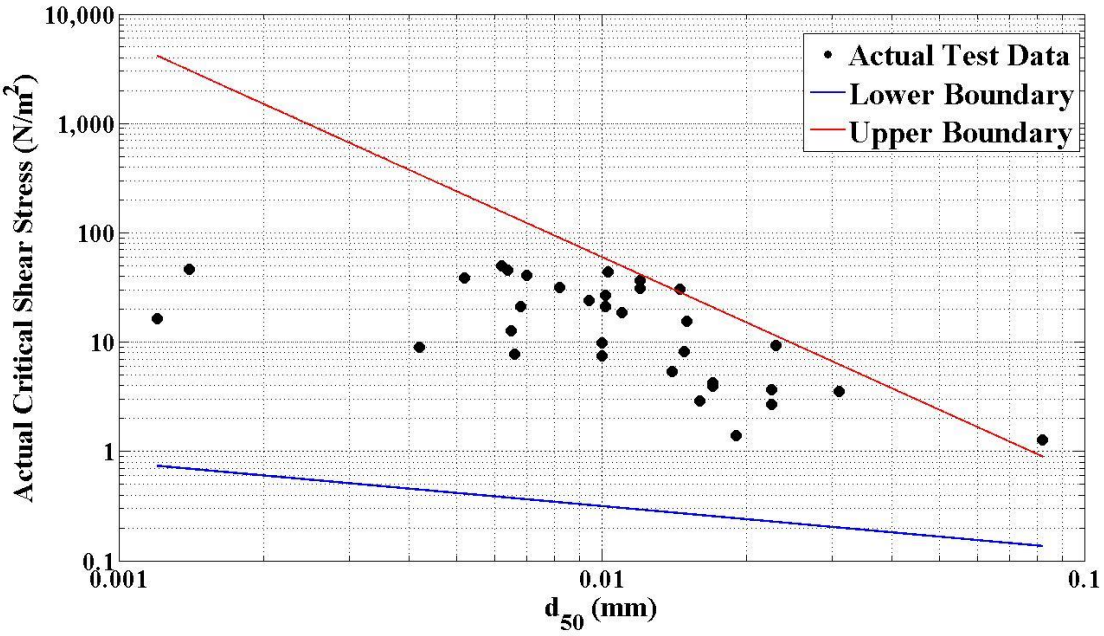

Fig. 4.21. Comparison of actual shear stress with Briaud et al. (2011) boundaries as a function of median grain size

Most of the actual critical shear stress data of this project fit well within the Briaud et al. (2011) boundaries in Fig. 4.21, as only 2 observations (out of 33) were out of the boundary. One of the possible reasons for this good agreement is that this project and Briaud et al. (2011) both used the same apparatus (EFA) for erosion tests. However, it is also visible that 7 observations of the actual critical shear stress (from this project) are crowded near the upper boundary of Briaud et al. (2011). This is likely because of higher values of the roughness coefficient, f used in the shear stress equation (eq. 2.16) in this project. In this project, f was determined by measuring the roughness of the eroding surface of each sample using calipers. However, Briaud et al. (2011) assumed the roughness of the sample was constant and equal to half of the median grain size of the soil. It has been seen in tests that, the actual roughness is far higher when measured with calipers than taking a constant value as half of the median grain size. This possibly resulted the actual values of critical shear stresses in this project to be higher and lie near the upper boundary of Briaud et al. (2011).

4.5.3 Comparing Shan et al. (2015) Model

Shan et al. (2015) developed a model to predict critical shear stresses based on laboratory tests using the Ex Situ Scour Test Device (ESTD). The predictive model is given in the following equation:

$$\tau_c = \alpha \left(\frac{w}{F}\right)^{-2.0} PI^{1.3} q_u^{0.4} \tag{4.7}$$

where, α is 0.1 in S.I. unit, w is the water content, F is the percent finer than 0.075 mm, and PI is plasticity index dimensionless ratio, and q_u is the unconfined compressive strength. Since, all these variables were also measured in this project; the predicted values of critical shear stress using the Shan et al. (2015) model were compared with the actual values of critical shear stress as shown in Fig. 4.22.

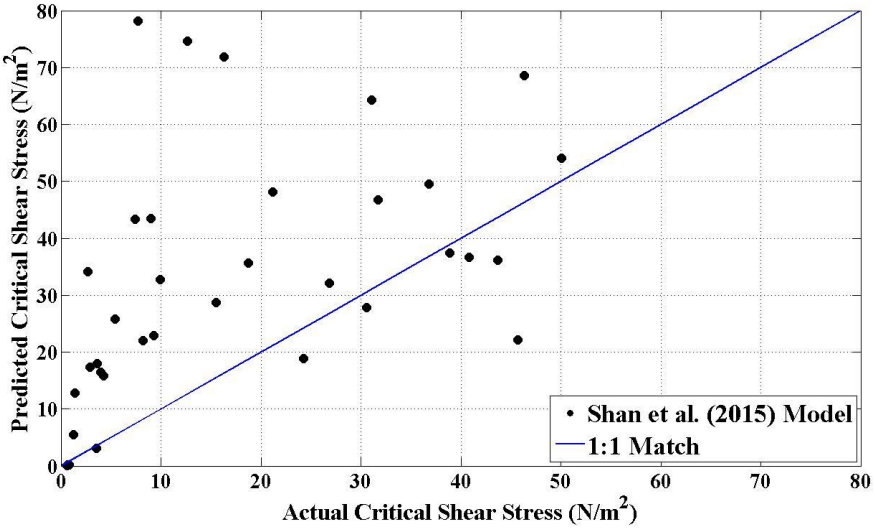

Fig. 4.22. Critical shear stress comparison (predicted vs. actual) using Shan et al. (2015) model

36 data points were used to predict critical shear stress using Shan et al. (2015) model and as seen from Fig. 4.22, 28 of the critical shear stress values were over predicted by the model. This was likely due to the different processes of calculating shear stress in EFA (this project) and ESTD (Shan et al. 2015) apparatuses. Shan et al. (2015) also compared some of the erosion test results from Texas and Illinois. Texas samples were tested using EFA. Instances of over prediction (using

Shan et al. (2015) model) were also visible for the Texas samples in that comparison as shown in Fig. 4.23.

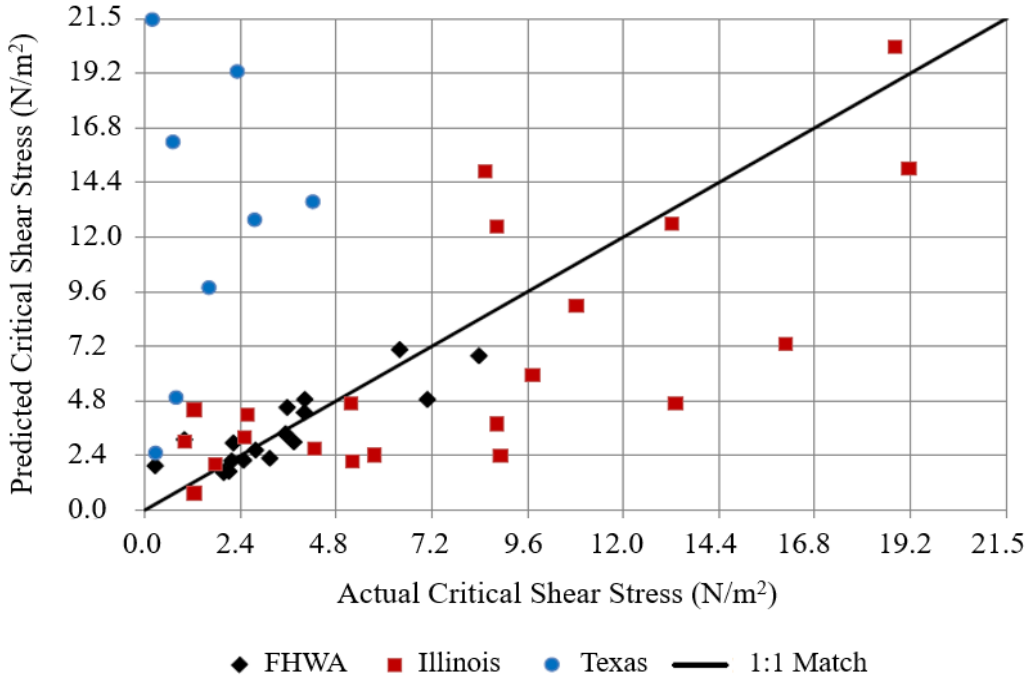

Fig. 4.23. Critical shear stresses predicted by Shan et al. (2015) model versus actual values for FHWA, Illinois and Texas data (adapted from Shan et al. 2015)

All 13 observations of critical shear stress from Texas data were over predicted by the Shan et al. (2015) model, though only eight points are shown due to limited graph scale. This supports the over predictions of critical shear stress when Shan et al. (2015) model was used for this project (Fig. 4.22) as shear stress is estimated differently in EFA and ESTD.

4.5.4 Combining Several Comparisons

To compare predicted versus actual values of critical shear stress for several models discussed above, corresponding graphs were combined in a single graph using the best fit lines of predicted versus actual critical shear stress plot of each model. Eight models were used: Model #1 through Model #7, developed in this study, and Shan et al. (2015) model as shown in Fig. 4.24.

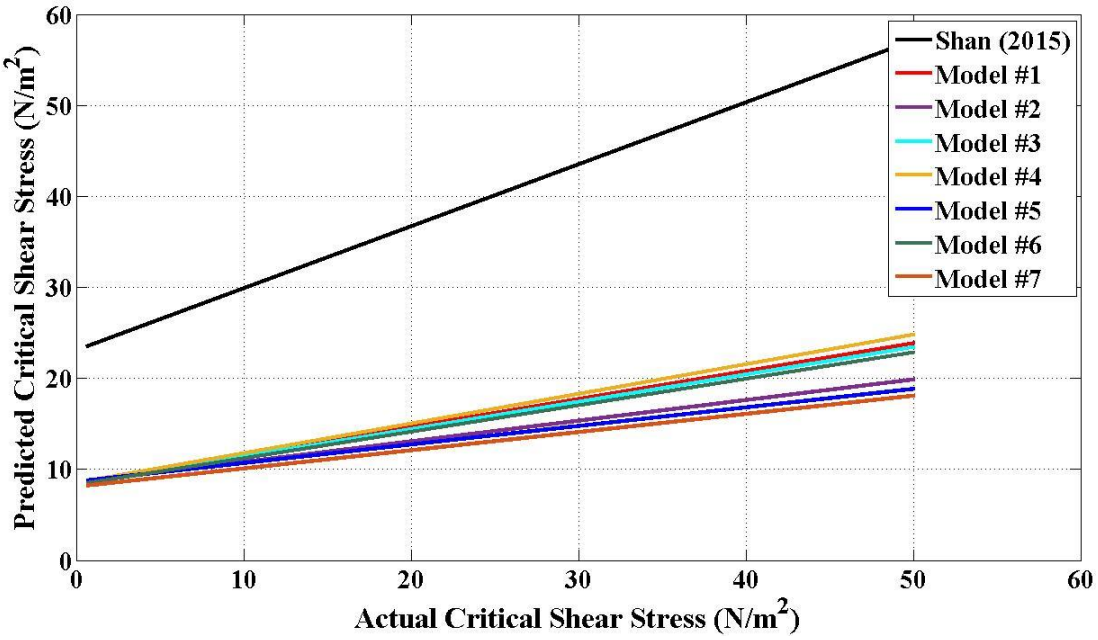

Fig. 4.24. Critical shear stress comparison (predicted vs. actual) for various models using best fit lines

According to Fig. 4.24, all models developed in this study, Model #1 through Model #7 predicted much lower values of critical shear stress compared to Shan et al. (2015) model (represented by the black line). Predicting lower critical shear stress is assuming that erosion will initiate at a lower shear stress during any flood event. As such, from engineering point of view, all the models generated in this study (Model #1 through Model #7) will provide a safer design compared to Shan et al. (2015) model.

4.6 Summary

This chapter indicates how ER can be used a primary tool (with the aid of HEC-18 erodibility categorizing graph) for prioritizing bridge monitoring schedule as well as to construct a robust model to predict critical shear stress that can be used to quantify the amount of scour across a channel section. However, the models proposed, need to be validated using further testing.

Chapter 5 - Conclusions, Recommendations and Future Work

5.1 Conclusions

The current FHWA methodology for predicting the potential of soil erosion is based on the analysis of coarse grained soils. When this methodology is applied to fine grained soils, the scour design is typically over-conservative. Therefore, site-specific testing is recommended as an alternative. Although a recent method (Shan et al. 2015) to predict the erosion potential of fine grained soils has been proposed by FHWA, it includes a limited range of fine grained soils. Therefore, site-specific testing remains as an alternative that is applicable for all soil types. While site-specific testing is a valid method, it is time consuming and costly. In this study, ER surveys were used to determine its applicability in bridge scour monitoring and design. Eleven sites were selected by KDOT around Kansas and used for this study to determine the correlation between ER and soil erodibility as well as for quantifying the soil erodibility near these scour critical bridges.

ER surveys were conducted at each site and soil samples were collected for erosion tests in the laboratory. In addition to the erosion testing in KSU-EFA, various geotechnical parameters such as median grain size, plasticity index, percent finer, water content were obtained. Median grain sizes varied between 0.0012 mm (K-58 #1) to 1.9200 mm (K-126 #5). On the other hand, plasticity indexes varied between 3 (US-69 #1) to 52 (K-58 #1). With the aid of the erodibility categorizing graphs (Arnenson et al. 2012), it was shown that soils were more erosive when median grain size increased and plasticity index decreased.

According to USCS, 43 out of 50 samples from 11 sites were classified as high or low plastic clays (CH or CL). Of the other seven samples, three were clayey sands (SC) from K-126, one was well-graded sand with clay (SW-SC) also from K-126, two were elastic silts (MH) from K-9, and one was silt (ML) from US-69. Using the erodibility categorizing graph, it was shown that SC and SW-SC were highly erodible. The other soil types had low to moderate erodibility.

One unique finding of this research was the ability to categorize erodibility based solely on bulk ER measurements. When the ER values corresponding to all 197 points in the erodibility categorizing graph were divided into two ranges (i.e. above and below 100 Ω-m), 73.1% of the samples that had an ER over 100 Ω-m were classified as high erodibility. When ER values were

below 100 Ω-m, 98.3% of the samples were low to moderate erodibility. Erodibility levels with respect to ER for all the samples are shown in Table 5.1.

Table 5.1. Categorizing erodibility using ER

	ER below 100 Ω-m	ER above 100 Ω-m	Probability (When below 100 Ω-m)	Probability (When above 100 Ω-m)
High Erodibility	3	19	1.75%	73.08%
Low/Moderate Erodibility	168	7	98.25%	26.92%
Total	171	26	100.00%	100.00%

Based on these findings shown in Table 5.1, transportation agencies can utilize ER to prioritize bridge sites for additional sampling and erosion testing as part of scour monitoring procedures. This methodology has the potential to reduce a large number of time consuming erosion tests during the primary stage of the FHWA required scour monitoring procedures.

Seven models were developed for predicting critical shear stress (τ_c). Variable screening criteria were used to select the best model among these and the following model was selected

$$\tau_c = 8.62\,\rho^{-0.61}\,d_{50}^{-0.17}PI^{0.38} \tag{5.1}$$

where, ρ is the measured ER, d_{50} is the median grain size, and PI is the plasticity index. The R^2 of this equation was 0.72. Moreover, in one of the other models, critical shear stress (τ_c) was predicted using only ER as independent variable such that

$$\tau_c = 118.62\,\rho^{-0.92} \tag{5.2}$$

where, all variables have previously been defined. The corresponding R^2 of 0.59 of the model in eq. 5.2 indicates that ER itself can predict the critical erosion with an acceptable accuracy if laboratory tests to determine other soil parameters are not possible. Eq. 5.2 may also be used for preliminary investigation to determine if a soil has a high erodibility and should be prioritized for additional testing.

5.2 Recommendations

Several recommendations were identified for implementation of these findings for KDOT and other transportation agencies. ER surveys should be conducted before sample drilling to ensure the borehole is in the middle of the survey. Survey locations may be moved because a site may have limited access due to person property fences, steep grades, or subsurface materials may not be suitable for ER electrode stake driving. For example, at US-24 an abandoned pavement section was discovered in the subsurface and it was not possible to drive stakes through the asphalt pavement. Therefore, the other side of the highway was used for sampling and the ER survey. Also, the contact resistance between the stakes and soil must be checked before performing an ER survey. A contact resistance test indicates if the surface area of the stakes has sufficient contact with the ground, because poor contact will increase the contact resistance. Contact resistance of above 40,000 Ω-m does not provide enough current to receive reliable data and data becomes too noisy for interpretation (Snapp 2015). A contact resistance test can also identify any poor or wrong connections between cables and between electrodes and stakes in the ER survey. Finally, during drilling, after pushing the Shelby tube to a desired level, at least ten minutes delay is desirable before retrieving the tube with sample. This time delay ensures that enough skin friction develops between the soil and tube, so that maximum amount of soil is retrieved.

In the laboratory, while conducting erosion tests it is recommended to measure the roughness with slide calipers as opposed to assuming a constant roughness for all data points as was indicated in the literature review (Briaud 2001). The roughness greatly affects the shear stress measurement. A current study at K-State is developing a digital methodology for determining the roughness to further reduce operator dependence. One of the other challenges while testing in the EFA, was to avoid turbulence effect of flowing water. Turbulence occurs when holes are created on the eroding surface and it can result in erroneous erosion rates. When turbulence occurs, tests should be restarted after trimming the sample. Again, it is very difficult to predict the range of velocities to be selected for a particular sample. It is always better to follow an iterative process. If a sample erodes very fast at a certain velocity, the next test velocity should be chosen smaller than the previous velocity. This will ensure six data points can be measured without running out of sample. Regarding soil classification, it is recommended to use wet sieve method irrespective of the soil type.

5.3 Future Work

Among the eleven sites used in this study, only K-126 provided coarse grained soils and silts were found at two sites (K-9 and US-69). The remaining soil samples were either high or low plastic clays. Therefore, additional testing is needed to encompass a variety of soil types and corresponding ER and other soil parameters. This will help to build a more robust model applicable to a wide range of soil type and geologic conditions. Also, the predictive model to calculate the critical shear stress developed in this study requires validation using further tests. After validation, an economic factor of safety will be determined before application for quantifying amount of erosion.

In this study, the amount of soil per sample was insufficient to perform any strength tests on the soils such as to determine the cohesion and angle of friction at various load conditions. Because the soil index properties showed correlation with erosion potential, it is very likely that cohesion can be used to predict erosion potential in fine grained soils as well. Therefore, research is needed to incorporate soil strength parameter in the predictive model. Again, some of the available soil parameters such as water content, percent finer, liquid limit were not considered for critical shear stress model development because these parameters did not show good relationship with critical shear stress individually. However, combining these variables (such as taking their ratio) might show a better relationship with critical shear stress. This verification is also needed to possibly improve the critical shear stress model developed.

The results of Table 5.1 can be used to construct a probabilistic function (such as probability of exceedance) that can be used to categorize erodibility using ER with a certain confidence level. Furthermore, a different approach can be followed to quantify amount of erosion across a stream. One of the advantages of subsurface ER survey is that it captures a continuous (as opposed to discrete data points) subsurface ER distribution. In fact, ER data are collected for thousands of points across the subsurface to generate a contour map of the bulk resistivity. For example, in this study, ER values were measured across as many as 46,480 elements for a two-dimensional plane of 25.1 m x 6.6 m. It was shown ER alone can predict critical shear stress with an R^2 of 0.59 (eq. 5.2). Therefore, in future studies all of these subsurface elements can be assigned with corresponding erosion potential using the predictive equation. This would result in a subsurface

ER distribution converted into an erosion potential distribution across the subsurface to characterize the entire site.

References

Abu-Hassanein, Z. S., Benson, C. H., & Blotz, L. R. (1996). Electrical resistivity of compacted clays. *Journal of Geotechnical Engineering*, *122*(5), 397-406.

Aberle, J., Nikora, V., & Walters, R. (2004). Effects of bed material properties on cohesive sediment erosion. *Marine Geology*, *207*(1), 83-93.

Avnimelech, Y., Ritvo, G., Meijer, L.E., Kochba, M., 2001. Water content, organic carbon and dry bulk density in flooded sediments. Aquacultural Engineering 25 (1), 25–33.

AGI (Advanced Geosciences, Inc.). (2008). *Instruction Manual for EarthImager 2D Version 2.4.0 Resistivity and IP Inversion Software,* Advanced Geosciences, Inc., Austin, TX.

Arjwech, R. (2011). *Electrical resistivity imaging for unknown bridge foundation depth determination* (Doctoral dissertation, Texas A&M University).

Arjwech, R., Everett, M. E., Briaud, J. L., Hurlebaus, S., Medina-Cetina, Z., Tucker, S., & Yousefpour, N. (2013). Electrical resistivity imaging of unknown bridge foundations. *Near Surface Geophysics*, *11*(6), 591-598.

Amaryan, L. S. (1993). *Soft soil properties and testing methods*. AA Balkema.

Amos, C.L., Bergamasco, A., Umgiesser, G., Cappucci, S., Cloutier, D., DeNat, L., Flindt, M., Bonardi, M., Cristante, S. (2004). The stability of tidal flats in Venice Lagoon — the results of in-situ measurements using two benthic, annular flumes. *Journal of Marine Systems* 51(1), 211–241.

Arneson, L. A., Zevenbergen, L. W., Lagasse, P. F., & Clopper, P. E. (2012). *Evaluating scour at bridges* (No. FHWA-HIF-12-003).

ASTM D422-63 (2007). *Standard Test Method for Particle-Size Analysis of Soils*, ASTM International, West Conshohocken, PA.

ASTM D2216-10 (2010). *Standard Test Methods for Laboratory Determination of Water (Moisture) Content of Soil and Rock by Mass*, ASTM International, West Conshohocken, PA.

ASTM D4318-10 (2010). *Standard Test Methods for Liquid Limit, Plastic Limit, and Plasticity Index of Soils*, ASTM International, West Conshohocken, PA.

ASTM C117-13 (2013). *Standard Test Method for Materials Finer than 75-μm (No. 200) Sieve in Mineral Aggregates by Washing*, ASTM International, West Conshohocken, PA.

ASTM D4647/D4647M-13 (2013). *Standard Test Methods for Identification and Classification of Dispersive Clay Soils by the Pinhole Test*, ASTM International, West Conshohocken, PA.

ASTM C136/C136M-14 (2014). *Standard Test Method for Sieve Analysis of Fine and Coarse Aggregates*, ASTM International, West Conshohocken, PA.

ASTM D4220/D4220M-14 (2014). *Standard Practices for Preserving and Transporting Soil Samples*, ASTM International, West Conshohocken, PA.

ASTM D1587/D1587M-15 (2015). *Standard Practice for Thin-Walled Tube Sampling of Fine-Grained Soils for Geotechnical Purposes*, ASTM International, West Conshohocken, PA.

Avnimelech, Y., Ritvo, G., Meijer, L. E., & Kochba, M. (2001). Water content, organic carbon and dry bulk density in flooded sediments. *Aquacultural engineering*, *25*(1), 25-33.

Bale, A. J., Stephens, J. A., & Harris, C. B. (2007). Critical erosion profiles in macro-tidal estuary sediments: Implications for the stability of intertidal mud and the slope of mud banks. *Continental shelf research*, *27*(18), 2303-2312.

Bernhardt, M., Briaud, J., Kim, D., Leclair, M., Storesund, R., Lim, S. G., ... & Rogers, J. D. (2011). Mississippi river levee failure: June2008 flood.*International Journal of Geoengineering case history*.

Binley, A., & Kemna, A. (2005). DC resistivity and induced polarization methods. In *Hydrogeophysics* (pp. 129-156). Springer Netherlands.

Briaud, J. L., Ting, F. C., Chen, H. C., Gudavalli, R., Perugu, S., & Wei, G. (1999). SRICOS: Prediction of scour rate in cohesive soils at bridge piers.*Journal of Geotechnical and Geoenvironmental Engineering*, *125*(4), 237-246.

Briaud, J. L., Ting, F. C. K., Chen, H. C., Cao, Y., Han, S. W., & Kwak, K. W. (2001). Erosion function apparatus for scour rate predictions. *Journal of geotechnical and geoenvironmental engineering*, *127*(2), 105-113.

Briaud, J.L., Chen, H.C., Chang, K.A., Oh, S.J., Chen, S., Wang, J., Li, Y., Kwak, K., Nartjaho, P., Gudaralli, R., Wei, W., Pergu, S., Cao, Y.W., and Ting, F. (2011). The Sricos – EFA Method Summary Report, Texas A&M University.

Calappi, T., Miller, C. J., & Carpenter, D. (2010). Revisiting the HEC-18 Scour Equation. In *Scour and Erosion* (pp. 1102-1109). ASCE.

Chambers, J. E., Wilkinson, P. B., Penn, S., Meldrum, P. I., Kuras, O., Loke, M. H., & Gunn, D. A. (2013). River terrace sand and gravel deposit reserve estimation using three-dimensional electrical resistivity tomography for bedrock surface detection. *Journal of Applied Geophysics*, *93*, 25-32.

Clark, L. A., & Wynn, T. M. (2007). Methods for determining streambank critical shear stress and soil erodibility: implications for erosion rate predictions. *Transactions of the ASABE*, *50*(1), 95-106.

Coduto, D. P. D. P. (1999). *Geotechnical engineering: principles and practices* (No. Sirsi) i9780135763803).

Crowley, R. W., Bloomquist, D., Robeck, C. (2012). Description of erosion rate testing devices and correlations between rock erosion and cohesion. *Proc., International Conference on Scour and Erosion,* ICSE6, Paris, 205.

Crowley, R. W., Bloomquist, D. B., Shah, F. D., Holst, C. M. (2012). The Sediment Erosion Rate Flume (SERF): A New Testing Device for Measuring Soil Erosion Rate and Shear Stress. *Geotech Test J,* 35(4).

Dahlin, T. (2001). The development of DC resistivity imaging techniques.*Computers & Geosciences*, *27*(9), 1019-1029.

Debnath, K., Nikora, V., Aberle, J., Westrich, B., & Muste, M. (2007). Erosion of cohesive sediments: resuspension, bed load, and erosion patterns from field experiments. *Journal of hydraulic engineering*, *133*(5), 508-520.

Dickhudt, P. J., Friedrichs, C. T., & Sanford, L. P. (2011). Mud matrix solids fraction and bed erodibility in the York River estuary, USA, and other muddy environments. *Continental Shelf Research*, *31*(10), S3-S13.

Droppo, I. G., Lau, Y. L., & Mitchell, C. (2001). The effect of depositional history on contaminated bed sediment stability. *Science of the Total Environment*, *266*(1), 7-13.

Dunn, I. S. (1959). Tractive Resistance of Cohesive Channels. *Journal of the Soil Mechanics and Foundations Division*, *85*(3), 1-24.

Everett, M. E. (2013). Electrical Resistivity Method. Chapter 4 in *Near-Surface Applied Geophysics*. Cambridge University Press, New York, NY, 70-102

Fukue, M., Minato, T., Horibe, H., & Taya, N. (1999). The micro-structures of clay given by resistivity measurements. *Engineering geology*, *54*(1), 43-53.

Furman, A., Ferré, T., & Warrick, A. W. (2003). A sensitivity analysis of electrical resistivity tomography array types using analytical element modeling. *Vadose Zone Journal*, *2*(3), 416-423.

Giao, P. H., Chung, S. G., Kim, D. Y., & Tanaka, H. (2003). Electric imaging and laboratory resistivity testing for geotechnical investigation of Pusan clay deposits. *Journal of Applied Geophysics*, *52*(4), 157-175.

Gillott, J.E., 1987. *Clay in Engineering Geology. Elsevier*, Amsterdam. 468pp.

Google Maps. (2016). [Kansas] [Street map]. Retrieved from https://www.google.com/maps/@38.8580219,-97.5989946,8.53z/data=!4m2!6m1!1s1TSszfwP27a3s5mQ-oy5yqrME9Z0.

Grabowski, R. C., Droppo, I. G., & Wharton, G. (2011). Erodibility of cohesive sediment: the importance of sediment properties. *Earth-Science Reviews*, *105*(3), 101-120.

Grissinger, E. H. (1982). Bank erosion of cohesive materials. *Gravel-bed rivers*, 273-287.

Hanson, G. J., Cook, K. R., & Simon, A. (1999, August). Determining erosion resistance of cohesive materials. In *Proc. ASCE Intl. Water Resources Eng. Conf*.

Hanson, G. J. and Simon, A. (2001). Erodibility of cohesive streambeds in the loess area of the midwestern USA. *Hydrological Processes* 15(1), 23-38.

Hanson, G. J., & Temple, D. M. (2002). Performance of bare-earth and vegetated steep channels under long–duration flows. *Transactions of the ASAE*, *45*(3), 695.

Heinzen, R. T. (1976). *Erodibility Criteria for Soil.* MS thesis, University of CA, Davis.

Houwing, E. J. (1999). Determination of the critical erosion threshold of cohesive sediments on intertidal mudflats along the Dutch Wadden Sea coast. *Estuarine, Coastal and Shelf Science*, *49*(4), 545-555.

Inazaki, T., Hayashi, K., Watanabe, F., Tokumaru, K. M. T., & Imamura, S. (2008, April). Ground truth verification of an integrated geophysical investigation for the assessment of an earthen levee. In *21st EEGS Symposium on the Application of Geophysics to Engineering and Environmental Problems*.

Jepsen, R., Roberts, J., & Lick, W. (1997). Effects of bulk density on sediment erosion rates. In *The Interactions Between Sediments and Water* (pp. 21-31). Springer Netherlands.

Johnson, B. D., Kranck, K., & Muschenheim, D. K. (1994). Physicochemical factors in particle aggregation. *The biology of particles in aquatic systems. Lewis Publishers, Boca Raton, Florida*, 75-96.

Julian, J. P. and Torres, R. (2006). Hydraulic erosion of cohesive riverbanks. *Geomorphology,* 76(1), 193-206.

KDOT (Kansas Department of Transportation). (2015, January). Personal interview.

Keller, G. V., & Frischknecht, F. C. (1966). Electrical methods in geophysical prospecting.

Kelly, W.E., Gularte, R.C. (1981). Erosion resistance of cohesive soils. *Journal of the Hydraulics Division*-ASCE 107 (10), 1211–1224.

Kimiaghalam, N., Clark, S. P., & Ahmari, H. (2016). An experimental study on the effects of physical, mechanical, and electrochemical properties of natural cohesive soils on critical shear stress and erosion rate. *International Journal of Sediment Research*, *31*(1), 1-15.

Kibria, G., and Hossain, M. S. (2012). Investigation of geotechnical parameters affecting electrical resistivity of compacted clays. *Journal of Geotechnical and Geoenvironmental Engineering*, 138(12), 1520-1529.

Knapen, A., Poesen, J., Govers, G., Gyssels, G., & Nachtergaele, J. (2007). Resistance of soils to concentrated flow erosion: A review. *Earth-Science Reviews*, *80*(1), 75-109.

Knight, R. J., and Endres, A. L. (2005). An Introduction to Rock Physics Principles for Near-Surface Geophysics. *Near Surface Geophysics*, Society of Exploration Geophysics, Tulsa, Ok, 31-70.

Koefoed, O. (1979). Geosounding principles, 1. *Resistivity Sounding Measurements*.

Kwader, T. (1985). Estimating aquifer permeability from formation resistivity factors. *Ground Water*, *23*(6), 762-766.

Lau, Y. L., & Droppo, I. G. (2000). Influence of antecedent conditions on critical shear stress of bed sediments. *Water Research*, *34*(2), 663-667.

Leeder, M.R. (1999). Sedimentology and Sedimentary Basins. From Turbulence to Tectonics. xvi+ 592 pp. Oxford: Blackwell Science.

Lick, W., Jin, L., & Gailani, J. (2004). Initiation of movement of quartz particles. *Journal of Hydraulic Engineering*, *130*(8), 755-761.

Lick, W., & McNeil, J. (2001). Effects of sediment bulk properties on erosion rates. *Science of the Total Environment*, *266*(1), 41-48.

Lin, C., Han, J., Bennett, C., & Parsons, R. L. (2014). Case history analysis of bridge failures due to scour. In *Climatic Effects on Pavement and Geotechnical Infrastructure* (pp. 204-216). ASCE Publications.

Loke, M. H. (1999). *Electrical Imaging Surveys for Environmental and Engineering Studies*.

Lucius, J. E., Langer, W. H., & Ellefsen, K. (2007). *An introduction to using surface geophysics to characterize sand and gravel deposits*. US Geological Survey.

McCarter, W. J. (1984). The electrical resistivity characteristics of compacted clays. *Geotechnique*, *34*(2), 263-267.

Mehta, A.J., Parchure, T.M. (2000). Surface erosion of fine-grained sediment revisited. In: *Flemming, B.W., Delafontaine, M.T., Liebezeit, G. (Eds.), Muddy Coast Dynamics and Resource Management*. Elsevier, London. 55–84pp.

Mendenhall, W., & Sincich, T. (2012). *A second course in statistics: Regression analysis* (7th ed.). Boston, Mass.; London: Prentice Hall.

Moody, L. F. (1944). Friction factors for pipe flow. *Trans. Asme*, *66*(8), 671-684.

Moody, J. A., Smith, J. D., & Ragan, B. W. (2005). Critical shear stress for erosion of cohesive soils subjected to temperatures typical of wildfires. *Journal of Geophysical Research: Earth Surface*, *110*(F1).

Moore, W. L., & Masch, F. D. (1962). Experiments on the scour resistance of cohesive sediments. *Journal of Geophysical Research*, *67*(4), 1437-1446.

Munson, B. R., Young, D. F., & Okiishi, T. H. (1990). *Fundamentals of fluid mechanics*. New York, *3*(4).

Nassif, H., Ertekin, A. O., & Davis, J. (2002). Evaluation of bridge scour monitoring methods. *United States Department of Transportation, Federal Highway Administration, Trenton*.

Palacky, G. (1987). Resistivity characteristics of geological targets, in electromagnetic methods in applied geophysics, edited by Misac Nabighian, Society of Exploration Geophysicists. *Society of Exploration Geophysicists*, *1*, 55.

Panagiotopoulos, I., Voulgaris, G., & Collins, M. B. (1997). The influence of clay on the threshold of movement of fine sandy beds. *Coastal Engineering*, *32*(1), 19-43.

Richardson, E. V., Harrison, L. J., Richardson, J. R., & Davis, S. R. (1993).*Evaluating scour at bridges* (No. HEC 18 (2nd edition)).

Richardson, E. V., & Davis, S. R. (2001). Evaluating Scour at Bridges, Hydraulic Engineering Circular No. 18 (HEC-18). *Rep. No. FHwA NHI*, 01-001.

Richardson, E. V., Pagan-Ortiz, J. E., Schall, J. D., & Price, G. R. (2003).*Monitoring and Plans for Action for Bridge Scour: Instruments and State Departments of Transportation Experiences* (No. E-C049,).

Rowell, D. L. (2014). *Soil science: Methods & applications*. Routledge.

Salim, S., Jayaratne, R., & Wijeyesekera, D. C. (2011). Soil protrusion apparatus for erosion rate prediction with smooth and rough sediment beds.

Samouëlian, A., Cousin, I., Tabbagh, A., Bruand, A., & Richard, G. (2005). Electrical resistivity survey in soil science: a review. *Soil and Tillage research*, *83*(2), 173-193.

Sanford, L. P. (2008). Modeling a dynamically varying mixed sediment bed with erosion, deposition, bioturbation, consolidation, and armoring. *Computers & Geosciences*, *34*(10), 1263-1283.

SAS Institute Inc. (2014). SAS™ [Computer software]. SAS Institute Inc., Cary, NC.

Schuring, J. R., Dresnack, R., Golub, E., Khan, M. A., Young, M. R., Dunne, R., & Aboobaker, N. (2010). Review of bridge scour practice in the US. In *Scour and Erosion* (pp. 1110-1119). ASCE.

Shan, H., & Kerenyi, K. (2014). Scour in Cohesive Soils.

Sheppard, D. M., and Bloomquist, D. (2005). *Design and Construction of Apparatus for Measuring Rate of Water Erosion of Sediments,* Florida Department of Transportation, Tallahassee, FL.

Shields, A. (1936). Anwendung der Aenlichkeitsmechanik und der Turbulenzforschung auf die Geschiebebewegung. *Mittleilungen der Preussischen Versuchsanstalt fur Wasserbau und Schiffbau*, W. P. Ott and J. C. Van Uchelen, translators, California Institute of Technology, Pasadena, Calif.

Smerdon, E. T., & Beasley, R. P. (1961). Critical tractive forces in cohesive soils. *Agricultural Engineering*, *42*(1), 26-29.

Snapp, M. A. (2015). *Electrical resistivity measurements of mechanically stabilized earth retaining wall backfill* (MS Thesis, Kansas State University).

Thomsen, L., & Gust, G. (2000). Sediment erosion thresholds and characteristics of suspended aggregates on the western European continental margin. *Deep Sea Research Part I: Oceanographic Research Papers*, *47*(10), 1881-1897.

Tikhonov, A. N., & Arsenin, V. Y. (1977). Solutions of ill-posed problems.

Trammell, M. A. (2004). *Laboratory apparatus and methodology for determining water erosion rates of erodible rock and cohesive sediments* (Doctoral dissertation, University of Florida).

Valenzuela, S. (2015, December 29). Personal interview.

Van Klaveren, R. W., & McCool, D. K. (1998). Erodibility and critical shear of a previously frozen soil. *Transactions of the ASAE*, *41*(5), 1315.

Van Ledden, M., Van Kesteren, W. G. M., & Winterwerp, J. C. (2004). A conceptual framework for the erosion behaviour of sand–mud mixtures. *Continental Shelf Research*, *24*(1), 1-11.

Vaudelet, P., Schmutz, M., Pessel, M., Franceschi, M., Guerin, R., Atteia, O., ... & Bégassat, P. (2011). Mapping of contaminant plumes with geoelectrical methods. A case study in urban context. *Journal of Applied Geophysics*, *75*(4), 738-751.

Winterwerp, J. C., & Van Kesteren, W. G. (2004). *Introduction to the physics of cohesive sediment dynamics in the marine environment* (Vol. 56). Elsevier.

Zhou, Q. Y., Shimada, J., & Sato, A. (2001). Three-dimensional spatial and temporal monitoring of soil water content using electrical resistivity tomography. *Water Resources Research*, *37*(2), 273-285.

Zonge, K., Wynn, J., Urquhart, S. (2005). Resistivity, Induced Polarization, and Complex Resistivity. *Near Surface Geophysics*, Society of Exploration Geophysics, Tulsa, OK, 265-300.

Zreik, D. A., Krishnappan, B. G., Germaine, J. T., Madsen, O. S., & Ladd, C. C. (1998). Erosional and mechanical strengths of deposited cohesive sediments. *Journal of Hydraulic Engineering*, *124*(11), 1076-1085.

Appendix A - Inverted Resistivity Sections

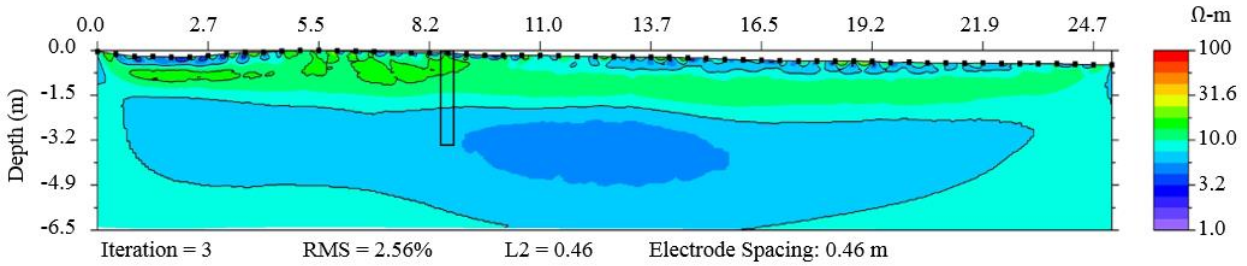

Fig. A.1. Inverted Resistivity of K-9

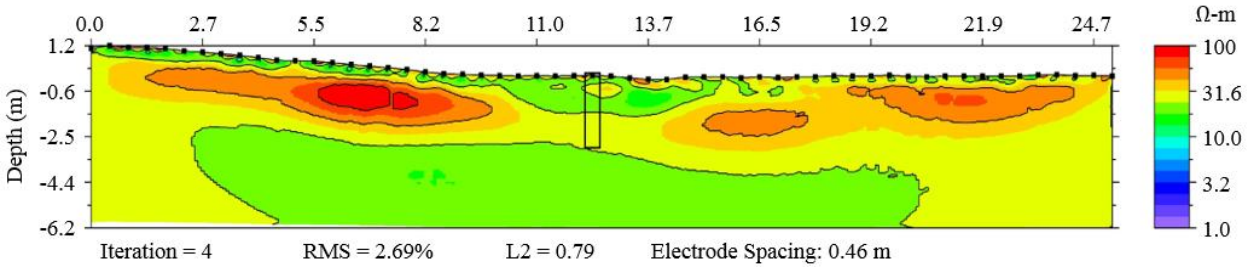

Fig. A.2. Inverted Resistivity of US-36

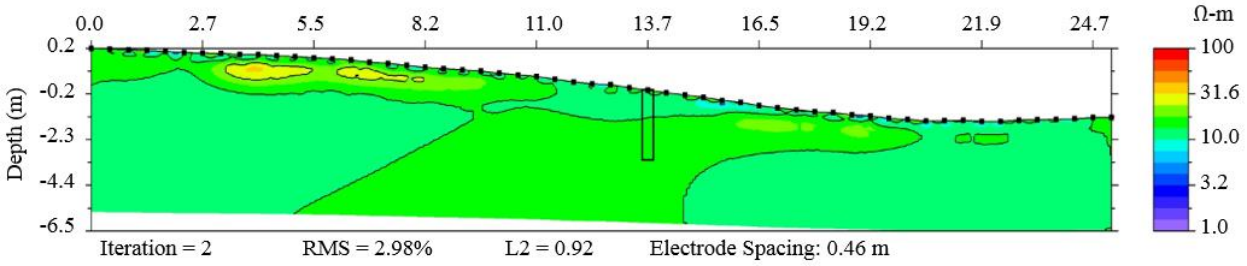

Fig. A.3. Inverted Resistivity of K-4B

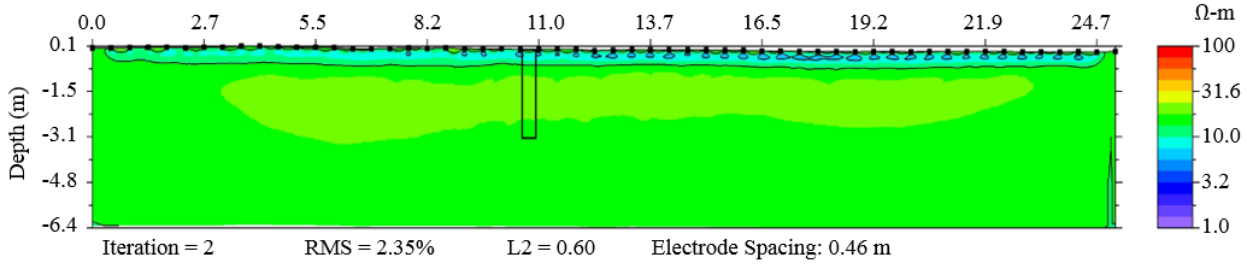

Fig. A.4. Inverted Resistivity of K-4A

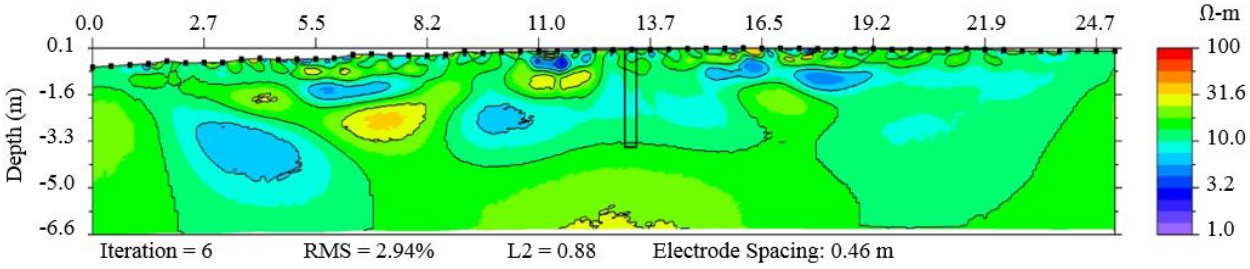

Fig. A.5. Inverted Resistivity of US-400

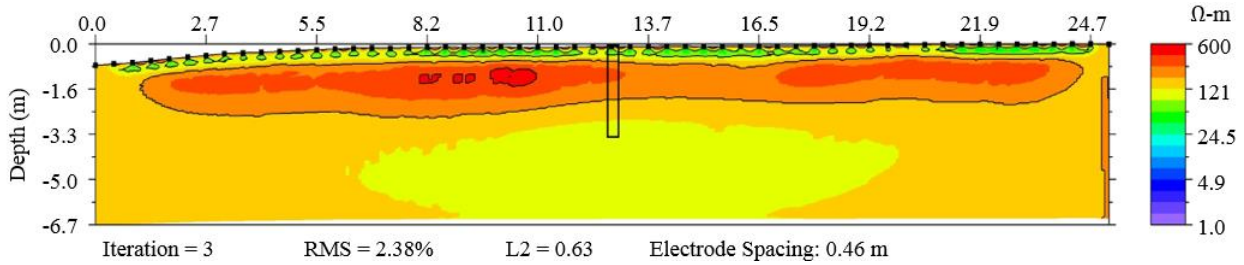

Fig. A.6. Inverted Resistivity of K-126

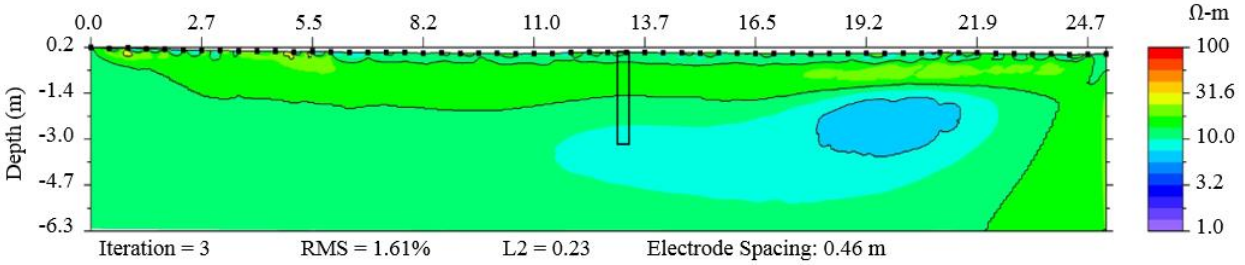

Fig. A.7. Inverted Resistivity of US-75

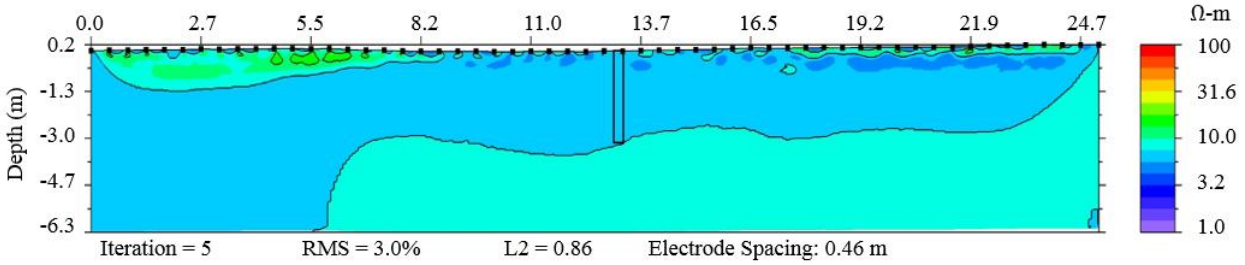

Fig. A.8. Inverted Resistivity of US-73

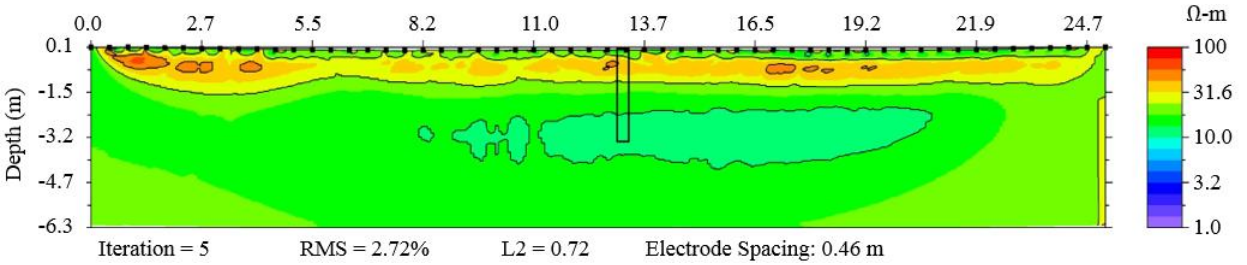

Fig. A.9. Inverted Resistivity of US-24

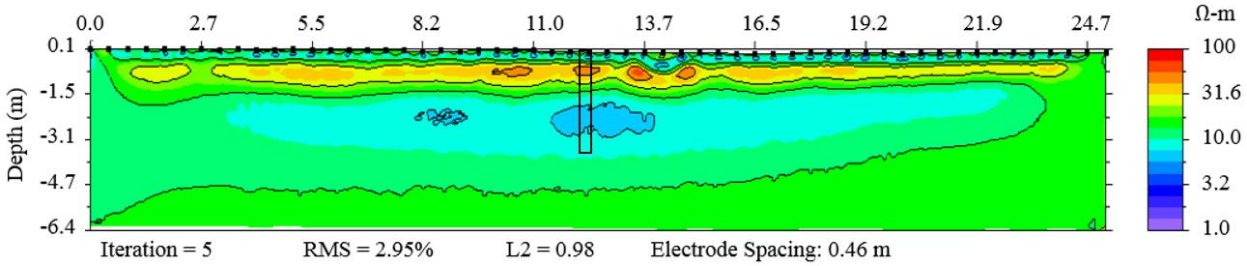

Fig. A.10. Inverted Resistivity of US-69